Investigating human visual processing using MEG and psychophysics

Hellen Jing Yuan

Supervised by Dr Christoph Teufel and Prof. Krish Singh

A thesis submitted to Cardiff University
for the degree of Doctor of Philosophy

November 2022

Summary

Our visual system organises sensory inputs into coherent object percepts. Knowledge and expectations about objects facilitate perceptual organisation via top-down processing. My PhD set out to investigate the neural mechanisms underpinning this process via frequency-tagging. Frequency-tagging studies embed flickers of different frequencies in a stimulus to drive narrow-band neural responses, which provide indices of spatial integration across the stimulus. My pilot experiments failed to robustly evoke this neural signature of perceptual organisation. Consequently, I conducted the following two lines of research.

In a series of MEG studies, I systematically investigated the power of flicker-evoked neural responses as a function of stimulation frequency (Chapter 2). The resulting temporal response tuning profile showed substantial individual variability, which I assessed in relation to two other intrinsic properties of the individual's visual system (Chapter 3). Spectral features of the temporal tuning profile were found to be associated with an individual's perceptual temporal resolution but not with the peak frequency of visually-induced gamma oscillations. Moreover, the temporal resolution was found to be unrelated to visual gamma oscillations and the computationally modelled synaptic properties underlying visual gamma (Chapter 4). These MEG studies provide insights into dynamical properties of the visual system and form the methodological basis for future frequency-tagging studies.

Besides the MEG research, I conducted a psychophysical study to investigate the top-down modulation of the perception of low-level features in an organised percept (Chapter 5). I found that whether the perceptual sensitivity to a low-level feature is enhanced by top-down processing depends on whether this feature contributes to the object percept. Future studies can investigate this effect further via frequency-tagging, by implementing flickers in the stimuli of the psychophysical task and choosing tagging frequencies informed by my MEG studies, to advance our understanding of the neural mechanisms underlying top-down processing in perceptual organisation.

Contents

List of Figures

List of Tables

List of Abbreviations

2IFC 2-interval forced choice. 45, 60, 67

AD Alzheimer's disease. 9, 14, 41, 103

ASSR auditory steady-state responses. 101, 102

BCI brain-computer interface. 9, 20, 44, 101

CFF critical flicker fusion. iii, v, vi, 8, 10, 11, 41, 43–52, 55–61, 63, 66, 67, 70–78, 99, 100, 107–110

CMC canonical microcircuit. vi, 68, 69

dB decibel. 25, 26

DCM Dynamic Causal Modelling. vi, 67, 68, 70–75, 77

DCM-SSR Dynamic Causal Modelling for steady-state responses. vi, 66, 68, 69, 75, 77, 100

ERD event-related desynchronisation. 27

ERPs event-related potentials. 45

FFT Fast Fourier Transform. vi, vii, 24, 54, 57–59, 67, 70, 71, 113, 115

G-C Gestalt-Collinear. 81, 83, 84, 86–93, 98, 103, 104, 117, 120, 121

G-NC Gestalt-NonCollinear. 81, 83, 84, 87–92, 96, 98, 103, 104, 117, 120

HE hepatic encephalopathy. 66, 76, 77

IM intermodulation. 5–8, 101, 103

LCMV linearly constrained minimum variance. 54

LGN lateral geniculate nuclei. 1–3

MEG magneto-encephalography. 4, 24, 47, 52, 53, 66

MRI magnetic resonance imaging. 4, 54

MSR magnetically shielded room. 21, 24, 47, 53

NG-C NoGestalt-Collinear. 83, 84, 88, 89, 91, 93, 117, 121

NG-NC NoGestalt-NonCollinear. 83, 84, 88–93, 117, 120, 121

PF psychometric function. vi, 51, 52, 107, 108

PING Pyramidal INterneuron Gamma. 46, 62, 65

SNR signal-to-noise ratio. 4, 9, 16–18, 25, 27

SSVEP steady-state visually evoked potentials. 4

TFR time-frequency representation. vii, 17, 25, 26, 54, 57–59, 67, 70, 71, 73, 114, 116

VSSR visual steady-state responses. v, vi, viii, 4, 5, 7–10, 13–20, 31, 35–41, 43–48, 56–64, 99–104, 111

Acknowledgements

I would not be able to do this PhD without funding from the Cardiff University School of Psychology Studentship and the generous financial support from my mother. I will always be grateful to you for enabling me to have this life-changing opportunity.

I would like to thank my amazing supervisors, Dr Christoph Teufel and Professor Krish Singh. Thanks for taking me on board as a newbie to the academic world and guiding me through a formative four and half years with more support than I could have asked for. Thank you for training me as a researcher, preparing me for future careers, and supporting me unwaveringly through all the difficult times. I cannot express how lucky I feel to have you as my supervisors. Special thanks to Christoph, for twice recognising that I was heading down the cliff of burnout and depression before I realised it myself. Without your support, I wouldn't have navigated through my personal crises in such a constructive way. Christoph and Krish, thank you so much for everything.

Many academics and fellow PhD students helped me immensely over the past years. Thanks, Dr Gavin Perry, for your technical support on all things MEG-related. Thanks, Dr Aline Bompas, for the helpful discussions and kind words throughout my PhD; I am grateful to have you as my internal assessor. Thanks, Marek Pedziwiatr, for helping me get started with coding experiments at the beginning of my PhD. You will be glad to know that coding remains one of the most enjoyable aspects of work for me. Thanks, Izzy Ward, for always lending a helping hand when I needed anything, from answers about ethics applications to an Overleaf template for this thesis. Thank you, Laura Bloomfield, for involving me in your effort to develop a visual equivalent to your auditory chirp stimuli. This led to the visual chirp project which ended up being an important part of my thesis. To my other amazing colleagues and friends from CUBRIC, thank you for being a part of my journey and making it so much warmer and more colourful – (in alphabetical order) Alisa Priemysheva, Allison Cooper, Aminette D'Souza, Anne Koopman, Caroline Fletcher, Caz Sealey, Deborah Jones, Diana Dima, Dominik Krzeminski, Elisabeth Van der Hulst, Eva Periche Tomas, Ewa Bukowska, Lorena Pach, Lucy Jackson, Megan Godfrey, Marlou Perquin, Simon Leclerc, and Zainab Hassan.

My awesome and loyal friends are a huge part of the reason I made it through this

PhD. Spending time with you has been my great privilege and invaluable fuel. I cannot thank you enough for all your love and care. In alphabetical order, thank you, Abi Finn, Adelina-Mihaela Halchin, Colette Milbourn, Connie Bettison, Holly Kings, Laura Bloomfield and your dog-shaped angels Loki and Luna, Laura Daïeff, Lucie Read, and my sisters from the Xiangdangnvzi comedy group. Completing this thesis also would not have happened without the great help from my counsellor Ceri. I'm lucky to have you by my side. Thanks for guiding me through my most difficult times and helping me recognise what I can do.

Finally, I would like to acknowledge my past self. During my undergraduate degree, I promised myself I would one day add the title 'Doctor' in front of my name. I committed to it and persevered through a year of illness and operations, a global pandemic, multiple rounds of depression, two major personal crises and a complete change of career plan. I kept my promise. This thesis is the result of an incredible four and half years of my life. I'd like to dedicate it to my younger self; I am so proud of you.

Data collection

The data presented in Chapter 5 were collected jointly by myself, Nur Nordin and Aaron Cousins. All other data presented in this thesis were collected by me.

Chapter 1

General introduction

1.1 The human visual system: from the retina to the visual cortex

Our human visual system is incredibly proficient at interpreting sensory inputs to make sense of our complicated visual environment and guide our behaviour. Visual processing starts at the retina in the back of the eyes. When light reaches the retina, photoreceptor cells convert light signals into electrical neural signals. These signals are transmitted across various types of cells in the retina before retinal ganglion cells send the retinal outputs, in the form of action potentials, through optic nerves to sub-cortical brain structures such as the lateral geniculate nuclei (LGN) in the thalamus (Schiller & Tehovnik, 2015b; Wandell, 1995). From the LGN, visual signals are conveyed to the primary visual cortex and further processed by various cortical regions.

Our visual environment and the stimuli in it are vastly varied; for instance, the lighting condition can be extremely bright outdoors during the day but very dim at night, it is sometimes important to perceive fine details of a visual object, and some objects can move at various speeds. To deal with such varied conditions and visual tasks, the visual system consists of two types of photoreceptors and multiple visual pathways with different properties.

The two types of photoreceptors in the retina, rods and cones, are sensitive to different kinds of light signals. Rods can respond to even extremely low illumination, but they have low acuity, cannot distinguish colours, and have a relatively long temporal integration period to accumulate sufficient light energy from the sparse photon flux in dim conditions (Donner, 2021). Whereas cones require high light levels but have high acuity and a shorter temporal integration period, making them more sensitive to motion and changing stimuli. The different wavelength sensitivity of three varieties of cones also enables colour vision. Cones are most concentrated in the centre of the visual field,

i.e., the fovea, and then their density decreases with increased eccentricity from the fovea. Rods are about 20 times more numerous than cones; most are located peripheral to the fovea (Schiller & Tehovnik, 2015b; Wandell, 1995).

Outputs from rods and cones are conveyed within the retina to various types of retinal ganglion cells, forming parallel neural retinogeniculate pathways, two of which are the midget and parasol systems (Schiller, 2010). Midget ganglion cells have small cell bodies, small dendritic arbors and small receptive fields. They can preserve colour information from cones and generate relatively sustained output responses. Parasol ganglion cells, on the other hand, have larger cell bodies, dendritic arbors and receptive fields than those of midget ganglion cells. Due to the pooled information from a larger receptive field, parasol ganglion cells cannot effectively process colour. However, they do output more transient responses, thus preserving information about fast motion and flickers. Retinal outputs from different types of ganglion cells are projected to different layers of the LGN. In particular, signals from midget ganglion cells feed into parvocellular layers of the LGN, and parasol ganglion cells convey signals into magnocellular layers of the LGN. The parvocellular pathway (a.k.a. the midget system) provides visual signals with colour, high spatial resolution and relatively low temporal resolution; this processing pathway is crucial in the perception of fine details, pattern and texture, and stereoscopic depth (as reviewed in Schiller, 2010; Schiller & Tehovnik, 2015a). In contrast, the magnocellular pathway (a.k.a. the parasol system) conveys mostly achromatic signals of poor spatial resolution but high temporal resolution, thus playing an important role in perceiving motion and fast flickers (Cao et al., 2010; Donner, 2021). The two processing pathways supply different neuronal populations in the visual cortex. It was found that some neurons in the primary visual cortex receive inputs only from either the parvocellular or the magnocellular pathway, while some V1 neurons receive convergent inputs from both pathways (Malpeli et al., 1981). More neurophysiological research is still being carried out to extend our understanding of the early visual system, for example, the properties and functions of the visual pathway involving the koniocellular layer of the LGN (Merkulyeva, 2022). Visual signals from parallel pathways originating in the retina form the basis for more complex visual processing in the cortex, such as object perception and spatial processing.

1.2 Top-down processing in perceptual organisation

When processing inputs from the visual environment, our visual system spatially integrates different parts of the stimulus into coherent percepts, resulting in holistic representations that differ from the sum of their parts (Pomerantz & Portillo, 2011). This process of perceptual organisation is essential for making sense of the visual inputs and

effectively structuring our perceptual experience (Wagemans, 2018).

Perceptual organisation can be driven by physical features of the stimulus, such as spatial proximity or featural similarity, as described by Gestalt grouping principles (Wagemans et al., 2012). These stimulus-driven factors influence spatial integration through bottom-up processes with a functional hierarchy, in which feature detectors in the early visual areas extract local low-level features, which are pooled in later areas to form more sophisticated representations of mid-level features and high-level object percepts (Frisby & Stone, 2010; Marr, 2010; Teufel & Nanay, 2017). In addition to this conventional model, more recent studies highlight the inverse relationship, namely that high-level representations exert top-down influences on early visual processing (e.g., Christensen et al., 2015; González-García & He, 2021; Pedziwiatr et al., 2021; Teufel et al., 2018), and such top-down processes can modulate perceptual organisation by promoting the spatial integration of certain parts of the stimulus but not others based on prior knowledge about the object in the scene. One example of knowledge-driven top-down modulation of perceptual organisation is the perception of two-tone images. Photos of commonly familiar objects can be converted into black-and-white two-tone images which are perceived by naive observers as meaningless patches. However, once the observer gains knowledge of the image content by viewing the original photo, the visual system organises the black and white patches into meaningful percepts of objects. Given that the physical properties of the two-tone image remain unchanged, the drastically different perception can only be attributed to object knowledge acquired through the original photo exerting top-down influence on perceptual organisation (Moore & Cavanagh, 1998; Teufel et al., 2018).

Top-down modulation of perceptual organisation is achieved via feedback connections both within and from outside of the visual system. Within the functional visual processing hierarchy of the LGN and visual cortex, projections from higher-level areas to lower-level areas are crucial for integrating local and global levels of visual analyses (see Teufel & Nanay, 2017, for review). In addition, there are extensive connections between the visual cortex and brain regions involved in higher-level cognition. For example, connections from dorsolateral prefrontal cortex and posterior parietal cortex to the visual areas enable attentional modulation of visual processing and perceptual behaviours (Corbetta & Shulman, 2002). Expectations from object knowledge and memory also facilitate visual processes like grouping via feedback connections from memory and executive systems (as reviewed in Summerfield & Egner, 2009; Teufel & Fletcher, 2020; Teufel & Nanay, 2017). Both the ventral visual pathway associated with categorical computations and the dorsal pathway important for visuospatial processing involve extensive feedback connections exerting top-down modulations (Gilbert & Li, 2013; Goodale & Milner, 1992).

While it is widely accepted that feedback connections from within and outside the visual system modulate visual processing like perceptual organisation, it is still unclear how the feedback signals conveying object knowledge integrate with bottom-up visual processing to modulate spatial integration. Therefore, my PhD project set out to investigate the neural mechanisms of knowledge-driven top-down modulation of perceptual organisation.

1.3 Investigating top-down processing in perceptual organisation using frequency-tagging

The neural mechanisms of top-down visual processing can be studied using various methodological approaches, from animal electrophysiology, computational modelling, behavioural testing methods like psychophysics, to neuroimaging techniques like magnetic resonance imaging (MRI) and magneto-encephalography (MEG). My investigation was initially planned to use the MEG-based frequency-tagging technique.

Frequency-tagging makes use of the neural phenomenon of visual steady-state responses (VSSR), also known as steady-state visually evoked potentials (SSVEP). Neural oscillations in the visual cortex can be categorised into three types: (i) spontaneous oscillations such as endogenous alpha activity, (ii) induced oscillations in response to but not phase-locked to stimulation (in other words, occurring after a jittered latency following the stimulus onset), such as visual gamma oscillations, and (iii) evoked oscillations both time-locked and phase-locked to a stimulus, occurring after a precise and fixed latency following the stimulus onset, an example being VSSR (Herrmann, 2001; Tallon-Baudry & Bertrand, 1999). The VSSR are neural oscillations evoked by a flickering visual stimulus of which a physical attribute is periodically modulated (Norcia et al., 2015). The modulated attribute can range from low-level physical properties such as luminance, contrast, or colour, to high-level features of the presentation such as face identity and object category. The periodic changes in the stimulus drive narrow-band responses in the visual cortex at the stimulation frequency (known as the fundamental frequency) and multiples of the stimulation frequency (known as harmonic frequencies) (Regan & Regan, 1989), which can be measured non-invasively using electrophysiological recordings with high temporal resolutions, for example, EEG and MEG.

VSSR was first reported in 1934 (Adrian & Matthews, 1934) and gained popularity in the 1960s (Norcia et al., 2015). Over time, paradigms making use of this neural phenomenon have grown more complex to study both perceptual and cognitive processes. As a research tool, VSSR has multiple advantages. First, VSSR are narrow-band responses, resulting in a high signal-to-noise ratio (SNR) even with a small number of

trials. Second, multiple stimulation frequencies can be presented simultaneously, and due to the narrow-band feature of VSSR, spectral analyses can recover responses evoked by each stimulation frequency as well as responses that reveal interactions between the multiple periodic inputs in visual processing. This technique of embedding flickers of more than one frequency in the visual stimulus is called frequency-tagging (Tononi et al., 1998).

When multiple tagging frequencies are presented simultaneously, in addition to fundamentals and harmonics, the visual system also produces additional intermodulation (IM) signals. IM components are responses at the sums and differences of fundamental and harmonic frequencies. For example, when the visual presentation contains periodic stimuli at frequencies f_1 and f_2, IMs can be at frequencies $nf_1 \pm mf_2$, where n and m are integers. Intrinsically, IM responses are a result of signals driven by different periodic inputs being integrated, thus making IMs an index of neural interactions and perceptual integration (Gordon et al., 2019).

The frequency-tagging technique has been used to study a wide range of neural mechanisms of various perceptual and cognitive processes such as figure-ground segregation, perceptual binding, binocular rivalry, socioemotional processing, attention, and working memory (for reviews, see Gordon et al., 2019; Norcia et al., 2015; Vialatte et al., 2010; Wieser et al., 2016). In particular, a number of studies have used frequency-tagging to demonstrate top-down modulation of perceptual organisation.

Vergeer et al. (2018) showed that IM signals could index top-down modulated perceptual organisation in holistic shape perception. Vergeer et al. (2018) created two families of mathematically defined shapes, and the exemplars within each shape family were classified into two categories according to subtle differences in the combinations of shape features. Participants were first trained to discriminate between exemplars of the two categories in one of the shape families via perceptual learning; then in a frequency-tagging session, participants viewed exemplars with their left and right halves filled with flickers of different frequencies. Stronger IMs were found when viewing shapes of the trained shape family (both exemplars used in perceptual learning and exemplars never seen before) compared to those from the untrained shape family. In other words, the magnitude of IMs showed that components of well-learnt shapes were more strongly integrated than those of unfamiliar shapes, suggesting that object-knowledge acquired through perceptual learning enhanced perceptual organisation.

Another example of knowledge-driven spatial integration is the perception of illusory surfaces in Kanizsa figures. Kanizsa figures, most commonly seen as Kanizsa triangles or squares, position inducers in specific spatial arrangements to elicit the perception of illusory surfaces in the shape of triangles, squares, etc. (see Figure 1.1B for an example). Perception of the illusory surface reflects spatial integration, because edges

of the inducers form partial contours of the illusory surface, and these local stimuli across the visual field must be combined to give rise to the percept of a coherent illusory shape.

Gundlach and Müller (2013) and Alp et al. (2016) used IMs to demonstrate that the percept of the illusory surface in Kanizsa figures was associated with increased neural integration. In Gundlach and Müller (2013)'s study, two aligned 'packman' shapes induced the percept of an illusory rectangle between the inducers in the illusory condition, while in the non-illusory condition a circle was placed between the inducers to disrupt the percept of the illusory rectangle (see Figure 1.1A). Tagging the two inducers with luminance modulation at 8.5 Hz (f_1) and 14.17 Hz (f_2) respectively, the IMs at $f_1 + f_2$ and $2f_1 + 2f_2$ were found to be significantly stronger when viewing the illusory stimulus compared to the non-illusory stimulus, indicating stronger neural integration when an illusory surface was perceived. Similarly, in Alp et al. (2016)'s study, four inducers elicited the percept of an illusory square in the illusory condition, whereas the rotated inducers formed no illusory surface in the non-illusory condition (as shown in Figure 1.1B). The two diagonal pairs of inducers were contrast modulated at 2.94 Hz (f_1) and 3.57 Hz (f_2) respectively, and significantly greater IMs were observed at $f_1 + f_2$ and $2f_1 + f_2$ in the illusory condition than in the non-illusory condition.

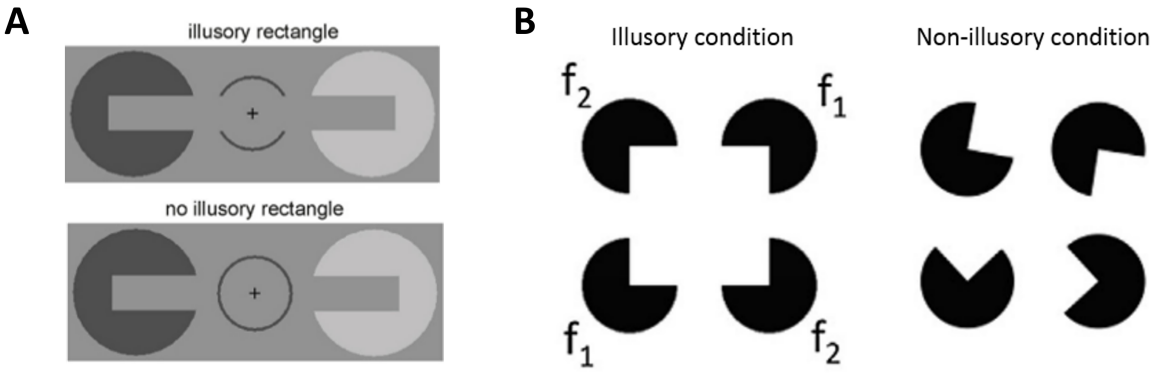

Figure 1.1: **Kanizsa stimuli used in Gundlach and Müller (2013)'s study (A) and Alp et al. (2016)'s study (B).**
Figures are from the two studies above.

The stronger IMs elicited by illusory stimuli in these two studies were interpreted by the studies' authors as the enhancement of spatial integration through knowledge-driven top-down processing. Since rectangles and squares are common and well-learnt geometric shapes, they are likely represented as holistic percepts in the visual system, just like novel shapes were represented as holistic percepts after perceptual learning in Vergeer et al. (2018)'s experiment. This object-knowledge can be conveyed by top-down signals and enhance the integration of inputs across the visual field so that partial contours

are spatially integrated to infer an illusory shape (Kogo & Wagemans, 2013). However, there are potential limitations to this interpretation. First, in both studies, the tagging frequencies were associated with the inducers rather than the illusory surface. Therefore, the increased IMs in the illusory conditions reflected the grouping of inducers, but not showing whether the area of the illusory surface itself was spatially integrated when perceived as a coherent object of a well-learnt shape. In order to provide stronger and more direct evidence for knowledge-driven spatial integration, tagging frequencies should be applied to regions within the illusory surface. This way, the amplitude of IMs would indicate the extent of spatial integration across the object onto which object-knowledge is applied. The second problem is the appropriateness of using Kanizsa figures to investigate knowledge-driven top-down modulation. The neural mechanism of perceiving illusory surfaces in Kanizsa figures has been debated extensively (for some reviews, see Kogo & Wagemans, 2013; Murray & Herrmann, 2013). Although it has been widely accepted that the perception of illusory surfaces requires enhanced spatial integration and neural convergence, it is uncertain whether this enhancement is underpinned by top-down signals conveying object-knowledge. Some proposals suggest that the illusory surface perception in Kanizsa figures is achieved through contour extraction, and this process can be completed via long-range horizontal connections in the early visual cortex converging signals from spatially separated visual fields, without the involvement of top-down feedback (Hou et al., 2003; Taylor et al., 2014; Victor & Conte, 2000). Even if the illusory surface perception does engage top-down modulation, as many have argued (e.g., Alp et al., 2016; Kok et al., 2016), the top-down modulation may not be underpinned by prior object-knowledge. To provide more direct evidence, a stimulus is required that unambiguously results in knowledge-driven top-down modulation of spatial integration. An example of such a stimulus is the two-tone images described earlier in this chapter.

To address the above limitations of the previous studies, I planned to conduct two frequency-tagging experiments. In Experiment 1, I hoped to replicate Alp et al. (2016)'s findings in a modified design, where frequency tags are implemented in the area of the illusory surface rather than in the inducers. In Experiment 2, I planned to investigate the knowledge-driven top-down modulation of perceptual organisation using a more appropriate type of stimulus, i.e., two-tone images, which allow manipulation of the presence of object-knowledge while keeping the physical properties of the stimulus constant, so that changes in the extent of spatial integration can only be attributed to the knowledge-driven top-down modulation. Furthermore, while most previous studies recorded VSSR with EEG, I chose to use MEG due to its capacity for more precise source localisation, which provides a means for more insights into the neural mechanism of the top-down modulation of perceptual organisation.

I conducted several pilot experiments but was not able to recreate the typical VSSR frequency spectra containing harmonic and IM responses as reported in past studies. By trying different tagging frequencies, I also noticed that different frequencies yielded responses of very different magnitudes. Frequency-tagging studies so far often select tagging frequencies somewhat arbitrarily. It has been hypothesised that low stimulation frequencies (< 6 Hz) elicit strong VSSR when implemented in stimuli that take longer to process (e.g., faces, object categories), whereas higher frequencies generate stronger VSSR when modulating low-level features such as contrast and luminance (Norcia et al., 2015). However, this notion has never been explicitly tested. It is also not strongly supported by the frequency choices in the current literature. While studies most commonly use tagging frequencies of 3-20 Hz (Norcia et al., 2015), frequencies as low as 1.3 Hz (Coll et al., 2020; Gordon et al., 2017) and as high as 78 Hz (Zhigalov et al., 2019) have been successfully used in frequency-tagging paradigms. Different studies have also used different tagging frequencies to investigate the same process. For example, to study the spatial integration in the perception of Kanizsa-like figures, Alp et al. (2016) used low tagging frequencies of 2.94 and 3.57 Hz, while Gundlach and Müller (2013) used higher frequencies of 8.5 and 14.17 Hz. Due to the difficulties I experienced in replicating previous frequency-tagging findings and the inconsistency of frequency selection in past studies, I saw the need to take a step back to establish a better methodological basis for the frequency-tagging technique by systematically investigating how the stimulation frequency affects the response profile of VSSR.

1.4 Overview of the current thesis

As a result of the considerations discussed in the previous section, my PhD project branched into two themes.

On the one hand, I conducted a line of MEG research to systematically investigate the power of VSSR as a function of stimulation frequency and the individual variability in this temporal response tuning profile (Chapter 2). I then explored the functional implications of the temporal response tuning profile (Chapter 3) by investigating its relationship with two other intrinsic properties of an individual's visual system, namely, the critical flicker fusion (CFF) threshold which indexes one's perceptual temporal resolution (Brenton et al., 1989) and the peak frequency of visually-induced gamma oscillations which reflects synaptic properties of the visual cortex microcircuitry (Shaw et al., 2017). Having obtained these measures, I also took the opportunity to assess the relationship between individuals' temporal resolution and induced gamma oscillations (Chapter 4).

Concurrently, in the second branch of my PhD work, I developed a psychophysical

task to study top-down processing in perceptual organisation (Chapter 5). Due to the restrictions of the COVID-19 pandemic, I had to conduct this study online. I had initially planned for the two themes of my research to be joined together by conducting frequency-tagging studies using the psychophysical task I had developed in the online study and tagging frequencies based on the results of my MEG study. However, due to the time constraint of my PhD, I did not have the opportunity to conduct such frequency-tagging studies. Therefore, this thesis will present the two lines of my research separately, with the MEG studies described in Chapters 2 to 4, and the psychophysical study detailed in Chapter 5. Each of these studies will be introduced briefly in the following sections of this chapter and in more detail in the Introduction section of Chapters 2 to 5.

1.5 Investigating dynamical properties of the visual system using MEG

1.5.1 Temporal response tuning profile

Establishing a profile of the magnitude, or power, of VSSR in response to a wide range of stimulation frequencies is an important methodological basis for all the applications of the VSSR phenomenon. As described earlier, VSSR has been used as a research tool in the frequency-tagging technique to study various perceptual and cognitive processes. Moreover, due to its stable spectral properties and high SNR, VSSR has also been used as a driver of brain-computer interface (BCI) systems (Hong & Qin, 2021; Vialatte et al., 2010) and in clinical applications to investigate pathological brain dynamics in various neurological and psychological conditions (Vialatte et al., 2010). In recent years, VSSR has also been explored as a clinical tool for the intervention of Alzheimer's disease (AD). Increasing neuronal oscillations in the gamma frequency band using flickering light stimulation at around 40 Hz is known as gamma entrainment, and it has been found to reduce AD pathologies in multiple transgenic AD mice models both by reducing beta-amyloid and phosphorylated tau in the brain and by improving cognition in abilities like recognition and spatial memory (Adaikkan et al., 2019; Iaccarino et al., 2016; Martorell et al., 2019). This new clinical application of VSSR is now being studied in humans and considered a promising non-invasive treatment for AD (K. Lee et al., 2021; Park et al., 2022). All the applications of VSSR described above require stimuli that evoke robust responses, therefore a comprehensive profile indicating what stimulation frequency elicits strong VSSR can inform the selection of stimulation frequencies and facilitate all future uses of this neural phenomenon.

In addition to forming a methodological basis for all applications of VSSR, understanding the temporal response tuning profile is also of conceptual interest, as the temporal tuning function is an important feature of the visual system and might reflect intrinsic properties of the visual cortex. For example, it is unclear whether the visual system has a "preferred" frequency or resonance frequency at which the strongest neural response occurs, as it does in the auditory system at around 40 Hz (Picton et al., 2003). Knowledge of the dynamical properties of the visual system can aid the understanding of the neuronal mechanisms underlying dynamic visual processing.

1.5.2 Functional implications of the temporal response tuning profile

In order to explore the conceptual and functional implications of the temporal response tuning profile established in Chapter 2, Chapter 3 assesses the individual differences in the VSSR tuning function in relation to observers' CFF threshold and the peak frequency of their visual gamma oscillations. Both these measures reflect intrinsic properties of an individual's visual system, and their relationship with the spectral features of one's temporal response tuning profile (or lack thereof) can provide insights into the interactions between different neural phenomena and improve our understanding of the neuronal mechanisms of dynamic visual processing (for more details, see the Introduction section of Chapter 3).

1.5.3 Relationship between the perceptual threshold for flickers and visual gamma oscillations

Having explored whether the temporal response tuning profile is associated with the CFF threshold and visual gamma oscillations, the relationship between the latter two visual properties was also assessed (Chapter 4). Even though the relationship between CFF and visual gamma is not directly relevant to VSSR or frequency-tagging, it complements the understanding of the dynamical properties of the visual system provided by Chapters 2 and 3,

As mentioned previously, visual stimulation can elicit evoked oscillations time-locked and phase-locked to the stimulus (such as VSSR) as well as induced oscillations occurring a jittered latency after the stimulus onset (Herrmann, 2001; Tallon-Baudry & Bertrand, 1999). Visual gamma oscillations are heightened neural activities at 30-80 Hz induced by intense visual stimuli such as black and white gratings (Adjamian et al., 2004). Following an initial neural response evoked by the onset of the stimulus, narrowband visual gamma oscillations occur about 300 ms after the stimulus onset and are

sustained for the duration of the stimulus (Hoogenboom et al., 2006; Swettenham et al., 2009). The frequency, bandwidth and amplitude of such visually-induced gamma rhythms are highly consistent within-subjects when the stimulus and the cognitive operation performed remain constant (Muthukumaraswamy et al., 2010), whereas large variability on gamma parameters exists between-subjects, which have also been shown to be strongly genetically determined (van Pelt et al., 2012). Such findings suggest that visual gamma oscillations reflect intrinsic properties of an individual's visual system, as does the CFF threshold.

Based on the current literature and theories, it may be speculated that visual gamma oscillations are functionally relevant to determining the highest temporal frequency one's visual system can resolve (this is explained in more detail in the Introduction section of Chapter 4). In other words, one's CFF threshold may be expected to be associated with the properties of their visual gamma oscillations. Despite the fact that both the CFF and visual gamma oscillations have been extensively studied for decades (Brenton et al., 1989; Han et al., 2021), the relationship between the two has not been well explored. The only published study on this is conducted on a patient sample and has various limitations (see section 4.1 on page 65 for more details). Therefore, in this project, I extend the current literature by assessing the relationship between the CFF and visual gamma oscillations in healthy observers and, by computationally modelling the cortical microcircuitry generating visual gamma oscillations, provide an understanding of the relationship between visual gamma and the CFF with greater mechanistic specificity.

1.6 Investigating top-down processing in perceptual organisation using psychophysics

Psychophysics and neuroimaging techniques like MEG complement each other in the investigation of the biological basis of perception. While psychophysical studies can provide insights into the mechanisms of visual processing on computational and algorithmic levels, neuroimaging and other techniques that measure neural activities can provide an understanding of the neuronal implementation of algorithmic mechanisms and inspire further psychophysical research (Read, 2015). Therefore, I conducted an online psychophysical study (described in Chapter 5) to develop a task of perceptual organisation and establish an effect which can be subsequently studied using frequency-tagging.

As mentioned earlier in this chapter, organised percepts arise from integrated bottom-up and top-down visual processing. As a part of the perceptual organisation process,

the perception of low-level features in the visual stimulus (e.g., local orientation and contrast) can be modulated by knowledge-driven top-down influences from high-level representations of objects (Teufel & Nanay, 2017). For instance, it has been repeatedly observed that the presence of object-knowledge about a high-level representation can alter the perceptual sensitivity to low-level local features compared to when no global percept is present (e.g., Christensen et al., 2015; Poljac et al., 2012; Teufel et al., 2018). However, past studies yielded inconsistent findings on whether the knowledge-driven top-down modulation enhances or suppresses the perceptual sensitivity to local low-level features (for more details, see the Introduction section of Chapter 5). I proposed a hypothesis that could reconcile these conflicting findings. Using an online psychophysical experiment, I tested the notion that the direction of top-down modulation is determined by whether or not the modulated low-level feature contributes to the high-level percept. Effects found in this experiment can be studied using frequency-tagging by implementing flickers to the stimuli of the psychophysical task. Psychophysical and frequency-tagging findings can complement each other in depicting the neural mechanisms of knowledge-driven top-down modulation of perceptual organisation.

Chapter 2

The temporal response tuning profile of the visual cortex

2.1 Introduction

2.1.1 Temporal response tuning profile

As introduced in Chapter 1, visual steady-state responses (VSSR) are neural oscillations evoked by periodically modulated visual stimuli, consisting of narrow-band responses at the stimulation frequency (fundamental frequency) and multiples of the stimulation frequency (harmonic frequencies[1]) (Regan & Regan, 1989). It is well-known that the magnitude, or power, of VSSR can vary with the stimulation frequency. This prompts the need for establishing a temporal response tuning function that describes the VSSR magnitude in response to various stimulation frequencies. Such a response tuning profile is important both in facilitating methodological choices of stimuli in frequency-tagging studies and in conceptually understanding the neuronal mechanism of the human visual system.

In frequency-tagging experiments, the flicker frequencies used must be able to evoke strong and robust VSSR (although this is not the only factor considered when selecting tagging frequencies). Studies so far have used various tagging frequencies, ranging from very low ones like 2.3 and 3 Hz (Aissani et al., 2011) and 2.94 and 3.57 Hz (Alp et al., 2016) to frequencies in the alpha and low-beta band, e.g., 8.5 and 14.17 Hz (Gundlach & Müller, 2013), 12 and 15 Hz (Parkkonen et al., 2008), to very high frequencies like 63 and 78 Hz (Zhigalov et al., 2019). Tagging frequencies are often selected somewhat

[1]In the literature, the term "first harmonic" is sometimes used to refer to the response at double the stimulus frequency and sometimes used to refer to the fundamental response. The current study uses the terms "fundamental" and "first harmonic" interchangeably, whereas the response at double the stimulation frequency is referred to as the second harmonic.

arbitrarily, given the lack of a comprehensive profile of VSSR power at a wide range of flicker frequencies. Establishing such a VSSR tuning profile can help future frequency-tagging studies make empirically-informed choices of tagging frequencies.

In addition to these methodological considerations, understanding the temporal response tuning profile is of conceptual interest, as the temporal tuning function reflects important dynamical properties of the visual system. For example, frequencies that lead to particularly strong VSSR could indicate that the visual cortical circuitry is especially efficient at generating and supporting oscillations in these frequency bands. The auditory system has been robustly shown to respond most strongly at around 40 Hz (Picton et al., 2003), but it is unclear whether the visual system also has such a "preferred" frequency or resonance frequency. Knowledge of the dynamical properties of the visual system and the individual variability in such properties forms the foundation for understanding the neuronal mechanisms underlying dynamic visual processing. It can also form the basis for future developments of using VSSR as a clinical tool, for example, as clinical biomarkers for diseases and as an intervention for preventing and modifying the course of Alzheimer's disease (AD).

Among studies that measured the VSSR power in the human visual cortex at a minimum of five stimulus frequencies (18 such studies of recent decades are summarised in Table 2.1), most studies found a predominant response peak in the fundamental component of VSSR in the alpha range (8-12 Hz) (Bakardjian et al., 2010; Bayram et al., 2011; Chen et al., 2019; Fawcett et al., 2004; Gulbinaite et al., 2019; Herrmann, 2001; Koch et al., 2006; Kuś et al., 2013; Lazarev et al., 2001; Lea-Carnall et al., 2016; Lin et al., 2012; Salchow et al., 2016; Srinivasan et al., 2006). However, some studies showed a lack of resonance in the alpha range; in these studies, the strongest VSSR was instead found in the low beta band between 14 and 16 Hz (Chen et al., 2019; Floriano et al., 2019; Kuś et al., 2013; Pastor et al., 2007; Pastor et al., 2003) or in the high beta band at 30 Hz (Lithari et al., 2016). In addition to a predominant response peak, many studies also found one or more smaller response peaks at various frequencies, ranging from 4-6 Hz theta frequencies (Bakardjian et al., 2010; Koch et al., 2006; Lazarev et al., 2001; Srinivasan et al., 2006), 13-30 Hz beta frequencies (Bakardjian et al., 2010; Bayram et al., 2011; Chen et al., 2019; Gulbinaite et al., 2019; Herrmann, 2001; Srinivasan et al., 2006), to gamma frequencies between 30 and 50 Hz (Bakardjian et al., 2010; Bayram et al., 2011; Floriano et al., 2019; Gulbinaite et al., 2019; Herrmann, 2001; Lin et al., 2012). Overall, it seems fair to say that previous studies on the VSSR power at different temporal frequencies have shown largely inconsistent findings.

Table 2.1: Summary of previous studies on the VSSR power at different temporal frequencies.

Study	**N**	**M/EEG**	**Apparatus**	**Stimulus**	**Frequencies**	**VSSR measure**	**Peak response**
Herrmann (2001)	10	EEG	LED goggles	White on/off flickers	1-100 Hz in 1-Hz steps	$Amplitude \times frequency$	Biggest peak 10 Hz, a smaller one in 20-30 Hz, the smallest peak in 35-45 Hz
Lazarev et al. (2001)	15	EEG	Xenon lamp	White on/off flickers (eyes closed)	11 freqs in 3-24 Hz (3, 4, 5, 6, 8, 10, 12, 15, 18, 21, 24 Hz)	Amplitude	Alpha band. 6 out of 14 also had a smaller peak in theta band (4-6 Hz)
Pastor et al. (2003)	16	EEG	Strobe lamp	White on/off flickers	14 freqs in 5-60 Hz (5, 10, 12, 15, 17, 20, 22, 25, 27, 30, 35, 40, 47, 60 Hz)	Amplitude	15 Hz
Fawcett et al. (2004)	6	MEG	Eizo Flexscan T562-T monitor (refresh rate 85 Hz)	Reversing checkerboard in lower right quadrant	Square-wave flicker: 0, 2, 4, 8, 21 Hz. Sine-wave flicker: 1, 2, 4, 8, 17 Hz	Normalised amplitude	8 Hz (elicited by a 4-Hz stimulus which contains 2 reversals in each cycle)
Koch et al. (2006)	11	EEG	LED goggles	Red on/off flickers (eyes closed)	22 freqs in 1-25 Hz (1 Hz, 5-25 Hz in 1-Hz steps)	Amplitude	2 peaks at 5 & 11 Hz

Continuation of Table 2.1

Study	N	M/EEG	Apparatus	Stimulus	Frequencies	VSSR measure	Peak response
Srinivasan et al. (2006)	9	EEG	Viewsonic PF790 monitor (refresh rate 120 Hz)	Random dot pattern presented centrally	16 freqs between 3-30 Hz (3, 4, 5, 6, 7.1, 8, 9.2, 10, 10.9, 12, 13.3, 15, 17.1, 20, 24, 30 Hz)	SNR	3 peaks at 3, 8 & 12-13 Hz
Pastor et al. (2007)	9	EEG	Strobe lamp	White on/off flickers	5, 10, 15, 25, 40 Hz	Amplitude	15 Hz
Bakardjian et al. (2010)	4	EEG	CRT screen (refresh rate 168 Hz)	Reversing checkerboard presented centrally	32 freqs between 5.1-84 Hz	Z-score of response power	12 Hz + smaller local peaks at 5.6, 8, 15.3, 28, 42 Hz
Bayram et al. (2011)	40	EEG	LED + mirror coated with semi-transparent paper	Diffused on/off flickers	13 freqs between 6-46 Hz (6, 8, 10, 12, 14, 18, 22, 26, 30, 34, 38, 42, 46 Hz)	Summed amplitude of first 3 harmonics	10 Hz + smaller local peaks around 20 & 40 Hz
Lin et al. (2012)	8	EEG	LED stroboscope + translucent screen	2-degree foveal disc or extra-foveal annulus	5-65 Hz in 5-Hz steps	SNR	Foveal: narrow peak at 10 Hz + broad peak at 30-35 Hz. Extra-foveal: a peak at 10 Hz

Continuation of Table 2.1

Study	N	M/EEG	Apparatus	Stimulus	Frequencies	VSSR measure	Peak response
Herbst et al. (2013)	30	EEG	LED goggles	White on/off flickers	10 freqs between 7.7-165.7 Hz (7.7, 15.7, 31.1, 41.7, 55.4, 62.3, 71.1, 82.9, 90.6, 165.7 Hz)	Amplitude	The lower the frequency, the stronger the response
Kuś et al. (2013)	10	EEG	LCD backlit by LED array	White on/off flickers	5-30 Hz in 1-Hz steps	Amplitude & SNR	Amplitude: 10-11 Hz. SNR: 16 Hz
Lea-Carnall et al. (2016)	13	EEG	Visual stimulation generator (refresh rate 140 Hz)	On/off full/half annulus made of red & green dots	10 freqs between 8.24-17.5 Hz (8.24, 8.75, 9.33, 10, 10.77, 11.67, 12.73, 14, 15.56, 17.5 Hz)	Normalised response power	8.8 or 10 Hz
Lithari et al. (2016)	21	MEG	PROPixx projector (refresh rate 180 Hz)	On/off Gabor ellipsoid centrally presented	9 freqs between 4-30 Hz (4, 6, 8.18, 10, 12.8, 15, 18, 22.5, 30 Hz)	TFR power change from baseline	30 Hz (the higher the frequency, the stronger the response)
Salchow et al. (2016)	12	MEG	LED light diffuser	On/off flickers in scotopic vision (eyes closed)	20 freqs between 0.4-2.3 times of individual alpha frequency	Amplitude	Individual endogenous alpha frequency

Continuation of Table 2.1

Study	**N**	**M/EEG**	**Apparatus**	**Stimulus**	**Frequencies**	**VSSR measure**	**Peak response**
Chen et al. (2019)	12	EEG	LCD screen (refresh rate 120 Hz)	Luminance-modulated square (sine- & square-wave)	6-40 Hz in 2-Hz steps	Amplitude & SNR	Amplitude: 2 peaks at 10 & 14 Hz. SNR: 14 Hz
Floriano et al. (2019)	12	EEG	LED-illuminated diffusion board	On/off flickers presented centrally	5-65 Hz in 5-Hz steps (except 50 Hz)	SNR	15 Hz + a smaller peak at 35-40 Hz
Gulbinaite et al. (2019)	19	EEG	LED arrays in front of a CRT monitor	White sine-wave flickers at bottom-left & bottom-right of fixation	41 freqs in 3-80 Hz (7-13 Hz in steps of 0.5 Hz)	SNR	Big alpha peak at 10 Hz + smaller gamma peak at 49 Hz. Some also had a beta peak.

A possible reason for the great variability in the VSSR tuning profiles is the varied designs of past studies. As Table 2.1 indicates, previous studies differed substantially in the apparatus used to present the stimuli, the range and sampling density of flicker frequencies, and the way VSSR magnitude was quantified. The VSSR tuning function can be affected by all those factors as well as visual properties of the stimulus (including size, eccentricity, intensity, contrast, colour, spatial frequency, and flicker waveform) (Chen et al., 2019; Labecki et al., 2016; Lea-Carnall et al., 2016; Lin et al., 2012; Salchow et al., 2016; Solf et al., 2020), the visual processing required by the task (e.g., passive viewing or needing to respond regarding certain features of the stimulus) (Norcia et al., 2015), and the observer's stage of development (infants, children, adolescents, or adults) (Lazarev et al., 2001; Morrone et al., 1996).

The designs of most previous studies differed from what is typically used in frequency-tagging experiments in one or more aspects. Frequency-tagging studies on perceptual and cognitive processing usually present visual stimuli at foveal or parafoveal locations using a monitor or projector, whereas many studies mentioned above presented flickers in peripheral vision or used LED goggles, diffused LED lights or strobe lamps to fill the entire visual field with flickering light. Such designs made the resultant VSSR tuning profiles less applicable and informative for choosing stimulus frequencies in frequency-tagging studies. Moreover, most of the studies summarised in Table 2.1 had small sample sizes of around or fewer than 10 participants, despite the considerable individual variability in the VSSR tuning profile repeatedly observed (Gulbinaite et al., 2019; Heinrich, 2010; Herbst et al., 2013; Kuś et al., 2013; Lazarev et al., 2001; Ramos-Junior et al., 2011; Solf et al., 2020).

2.1.2 The current study

As established earlier, it is both methodologically useful and conceptually important to characterise a comprehensive tuning profile of the VSSR power in response to a wide range of stimulation frequencies. However, existing literature on this yielded mixed findings and had important limitations. Most of previous studies had small sample sizes and tested only a small number of frequencies, or frequencies within a small range, or both. Moreover, the stimuli and/or presentation apparatus used in most of the past studies differed greatly to what is typically used in frequency-tagging experiments, making their results less applicable to frequency-tagging designs. The current study therefore aims to systematically investigate the VSSR tuning profile to a wide range of frequencies at a fine sampling resolution in a larger cohort than in past studies, using an apparatus and stimuli similar to those used in frequency-tagging experiments. With a larger sample size, the current study will also characterise and evaluate the individual

differences in the VSSR tuning profile.

In order to efficiently assess the VSSR power in response to flickers from 1 to 80 Hz at a fine sampling resolution of 0.5 Hz, the current study employs a visual chirp stimulus. As explained in more detail in the Method section below, a visual chirp is a flicker modulated at changing frequencies. As the stimulation frequency increases or decreases during a chirp, the visual system is stimulated at each of the frequencies contained in the chirp for a brief duration. This way, the visual system's response to a large number of stimulation frequencies can be measured within a short period of time.

Visual chirps have been used in some studies, mainly to drive BCI systems, but such BCI studies focused solely on the decoding accuracy rather than the response power at different stimulation frequencies (e.g., D. Jia et al., 2019; D. Jia et al., 2017; Tu et al., 2012; Waytowich & Krusienski, 2016). Two other studies measured the response power to visual chirp stimuli but used stimuli and presentation apparatuses very different to those used in frequency-tagging experiments and had small ranges of stimulation frequencies and small sample sizes (Fedotchev et al., 1990; Perenboom et al., 2020). Past studies using visual chirp stimuli assumed that chirp-evoked responses can approximate the VSSR evoked by fixed-frequency flickers, because fixed-frequency flickers can be seen as a specific case of visual chirp where the rate of frequency change is 0 (Fedotchev et al., 1990; Tu et al., 2012). However, the assumption that chirp-evoked responses are analogous to VSSR has not been formally tested. Therefore, the current study uses visual chirps as well as conventional fixed-frequency flickers of several frequencies across a wide range, to compare the temporal response tuning profiles resulting from fixed-frequency flickers and from visual chirps.

In summary, the aim of the current study is two-fold. First, I assess whether chirp-evoked responses can adequately approximate the VSSR evoked by fixed-frequency flickers. Second, I use a stimulus and apparatus set-up similar to those used in frequency-tagging experiments to establish the response tuning profile to a wide range of stimulation frequencies (1-80 Hz) at a fine sampling resolution (0.5 Hz). The individual differences in the tuning profile are also evaluated. The results not only provide a group-level tuning function informative for choosing stimulation frequencies in future frequency-tagging studies, but also help further our conceptual understanding of the dynamical properties of the visual system.

2.2 Methods

2.2.1 Participants

Thirty-seven students and staff of Cardiff University between 20 to 50 years of age took part in the study (28 females and 9 males, mean age = 28.19, SD = 6.16). All participants had normal or corrected-to-normal vision and no neurological or psychological conditions. All participants gave informed written consent before their first study session and were fully debriefed at the end of testing. Participants received £10 per hour in return for their time. The study was designed in accordance with the Declaration of Helsinki and approved by Cardiff University School of Psychology Ethics Committee.

2.2.2 Stimuli

Visual stimuli were programmed using Matlab (version R2015b, The MathWorks, Natwick, MI, USA) and the Psychophysics Toolbox (version 3.0.12) (Brainard, 1997; Kleiner et al., 2007; Pelli, 1997) and presented using a PROPixx DLP LED projector at a refresh rate of 1440 Hz and a spatial resolution of 1920*1080 pixels. Stimuli were projected onto a semi-translucent screen placed 120 cm from participants' eyes in a dark magnetically shielded room (MSR). A plain white stimulus spanning the entire screen resulted in a luminance of 230 cd/m^2, whereas a black presentation resulted in a luminance of 0.13 cd/m^2.

The flicker stimulus was a luminance-modulated Gaussian blob, presented centrally on a mid-grey background. The flickering region was presented through a 2D Gaussian window (clipped to a diameter of 11 degrees of visual angle with a sigma of 3.15 degrees of visual angle), so there was no sharp boundary between the flickering area and the static background. At the centre of the flicker, there was a small static mid-grey disc about 0.3 degrees of visual angle in size, on which a Gaussian window blended the boundary of the static disc with the surrounding flicker. A white fixation dot was presented at the centre of the static grey disc. The luminance of the flickering region was sinusoidally modulated between black and white, as illustrated in Figure 2.1.

Fixed-frequency flickers

In the fixed-frequency flicker task, the frequency of the stimulus was constant throughout the 4-second flicker period in each trial. Flickers were presented at eight frequencies, 5, 10, 20, 30, 40, 55, 65, and 75 Hz.

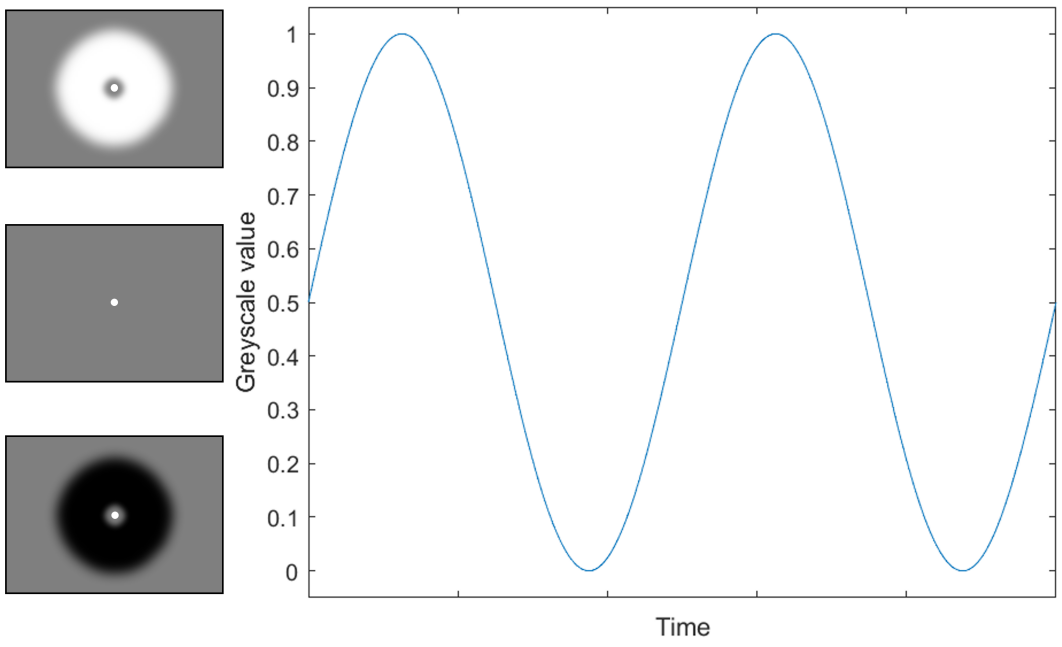

Figure 2.1: **Luminance profile of two cycles of an example flicker.**
The luminance-modulated flicker varied sinusoidally between black (denoted by a greyscale value of 0) and white (denoted by a greyscale value of 1) for two cycles in an example flicker. The appearances of the white, mid-grey and black stimuli are illustrated by the three panels on the left. When the stimulus is mid-grey, the luminance of the flickering area is the same as the background.

Visual chirps

In each trial of the visual chirp task, the stimulus frequency increased or decreased during the flicker period according to the parameters listed in Table 2.2. The luminance of the stimulus was modulated sinusoidally for one cycle at the starting frequency (e.g., 1 Hz), then for one cycle at each of the following frequency steps (e.g., 1.5, 2.0, 2.5, 3.0... Hz) until the flicker frequency reached the end frequency of the chirp. The stimulus frequency and luminance during an example chirp are illustrated in Figure 2.2.

The task used two upward and two downward chirps to cover the frequency range of 1-80 Hz in 0.5-Hz steps. Both upward and downward chirps were used to account for any possible carry-over effect from previously presented stimulus frequencies on the neural responses to subsequent frequencies. In order to keep each chirp short (under 5 s) to help participants maintain attention and minimise blinking during the chirp presentation, the frequency range was covered by high- and low-frequency chirps with overlapping frequencies rather than a continuous chirp covering the entire frequency range.

Table 2.2: **Visual chirp stimulus parameters**

Chirp type	Start frequency (Hz)	End frequency (Hz)	Step (Hz)	Chirp duration (s)
Low-frequency upward	1	9	0.5	4.99
High-frequency upward	7	80	0.5	4.95
Low-frequency downward	9	1	-0.5	4.99
High-frequency downward	80	7	-0.5	4.95

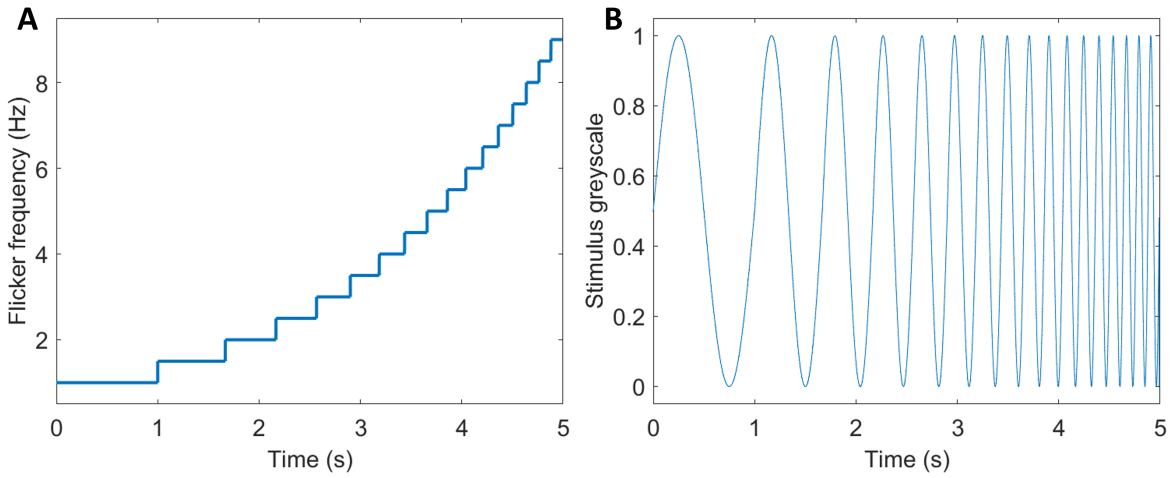

Figure 2.2: **Stimulus frequency and luminance of an example visual chirp.** The flicker frequency (A) and stimulus luminance (B) over time in a visual chirp where the frequency increases from 1 Hz to 9 Hz in steps of 0.5 Hz.

2.2.3 Procedure

As illustrated in Figure 2.3, each trial started with a fixation period of a jittered duration before the fixed-frequency flicker or visual chirp was presented. Participants were instructed to fixate at the central dot throughout the trial and make a button-press response as fast as possible when the fixation dot disappeared from the screen. This task was intended to keep participants engaged and focused.

Twenty trials were conducted for each stimulus frequency in the fixed-frequency flicker task, and 50 trials for each of the four visual chirp types described in Table 2.2. Trials of the same frequency (or chirp type) were grouped into a block, and the blocks were presented in a random order for each participant. Participants had a self-paced break after each block of trials. To mitigate the fatigue from viewing intense flickers

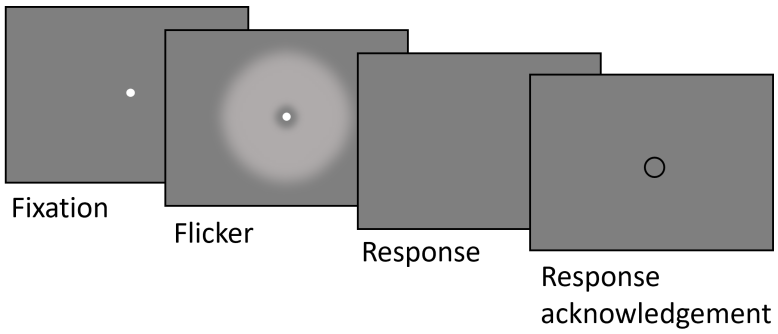

Figure 2.3: **One trial in the fixed-frequency flicker and visual chirp tasks.** After fixating for a jittered period of 1-1.5 s in the fixed-frequency flicker task or 3-3.5 s in the visual chirp task, the flicker stimulus was presented (for 4 s in the fixed-frequency flicker task and 5 s in the visual chirp tasks). Participants were instructed to press a button as fast as possible after the offset of the fixation dot. An open circle was then shown on the screen when a response was registered.

for extended periods, the two tasks were conducted on different days with the visual chirp task completed before the fixed-frequency flicker task.

2.2.4 MEG data acquisition and analysis

Neural oscillations during the tasks were recorded in a MSR with whole-head MEG using a 275-channel CTF axial gradiometer system sampled at 1200 Hz. Two of the sensors were turned off due to excessive sensor noise. An additional 29 reference channels were recorded for noise cancellation purposes. Three electromagnetic coils were placed at fiducial locations at nasion, and left and right pre-auricular. The fiducial positions and the participant's head shape were recorded using a Polhemus Digitizer (Polhemus, Colchester, VT, USA) at the beginning of each testing session.

The MEG data were first epoched into trials (-1 to 4 s around the onset of fixed-frequency flickers and -3 to 5 s around the onset of visual chirps). Using the Data Editor software (CTF MEG, Canada), visual inspection was carried out to exclude trials with muscular or head movement artefacts. The data were then processed and analysed using the Fieldtrip toolbox (Oostenveld et al., 2011) in Matlab (versions R2015a and R2017b).

Fixed-frequency flicker response tuning function

The time-series data of the fixed-frequency flicker task were band-pass filtered between 1-155 Hz and averaged across trials in the time domain. Spectral estimation was carried out for all occipital channels in the stimulus period using multitaper Fast Fourier Transform (FFT) with ± 0.34 Hz smoothing in steps of 0.25 Hz. From the resultant response

amplitude spectrum, the signal-to-noise ratio (SNR) of the response at each frequency bin in the spectrum was computed as the ratio between the response amplitude at each frequency bin and the mean amplitude of the eight adjacent frequency bins (four on each side, excluding the immediately adjacent bin), similar to the method of computing SNR used in previous studies, e.g., by Alp et al. (2016) and Liu-Shuang et al. (2014). The SNR spectra were averaged across all occipital channels in each participant. The SNR at each of the eight stimulus frequencies was then used as the basis for a response tuning function. The same procedure was used to construct response tuning functions for the harmonics.

Visual chirp response tuning function

The MEG time-series data of the visual chirp task were averaged across trials in the time domain within each chirp type described in Table 2.2. Then time-frequency analysis was performed on the sensor-space data using the Hilbert transform in the frequency range of 0-160 Hz, with steps of 0.25 Hz and a bandwidth of 2 Hz for the low-frequency visual chirps and 6 Hz for the high-frequency chirps. The resultant time-frequency representation (TFR) was baseline corrected into decibel (dB) against the responses 2.5-0.3 s before the chirp onset and averaged across all occipital channels.

For each participant, from the TFR of each visual chirp (an example can be seen in Figure 2.4A), responses at the stimulus frequencies and their harmonics were extracted by identifying peaks from the response spectrum at each time-point in the stimulus period (Figure 2.4B). In each response spectrum, a frequency range was defined around the instantaneous stimulus frequency and each of its harmonics. Then the largest response peak was identified within this frequency range. In upward chirps, the response at any given time was driven by a stimulus at a frequency lower than the instantaneous stimulus frequency (due to the time delay in sensory transduction and neural conduction), therefore the frequency ranges to identify peaks were defined as $[F - 0.4 \times F]$ to $[F + 0.1 \times F]$, with F denoting the instantaneous stimulus frequency and its harmonics up to the seventh order. Conversely, for downward chirps, responses were driven by higher frequencies than the instantaneous stimulus frequency, thus the ranges to draw the largest response peaks from were defined as $[F - 0.1 \times F]$ to $[F + 0.4 \times F]$. The peak responses identified from the response spectra at all the time points were then pooled, and the values of response power were averaged within each response frequency. This yielded a tuning function of response power at each response frequency (an example can be seen in Figure 2.4C). Such a tuning function was constructed for each response component (fundamental and harmonics) of each chirp type.

For each response component, the four response tuning functions derived from the

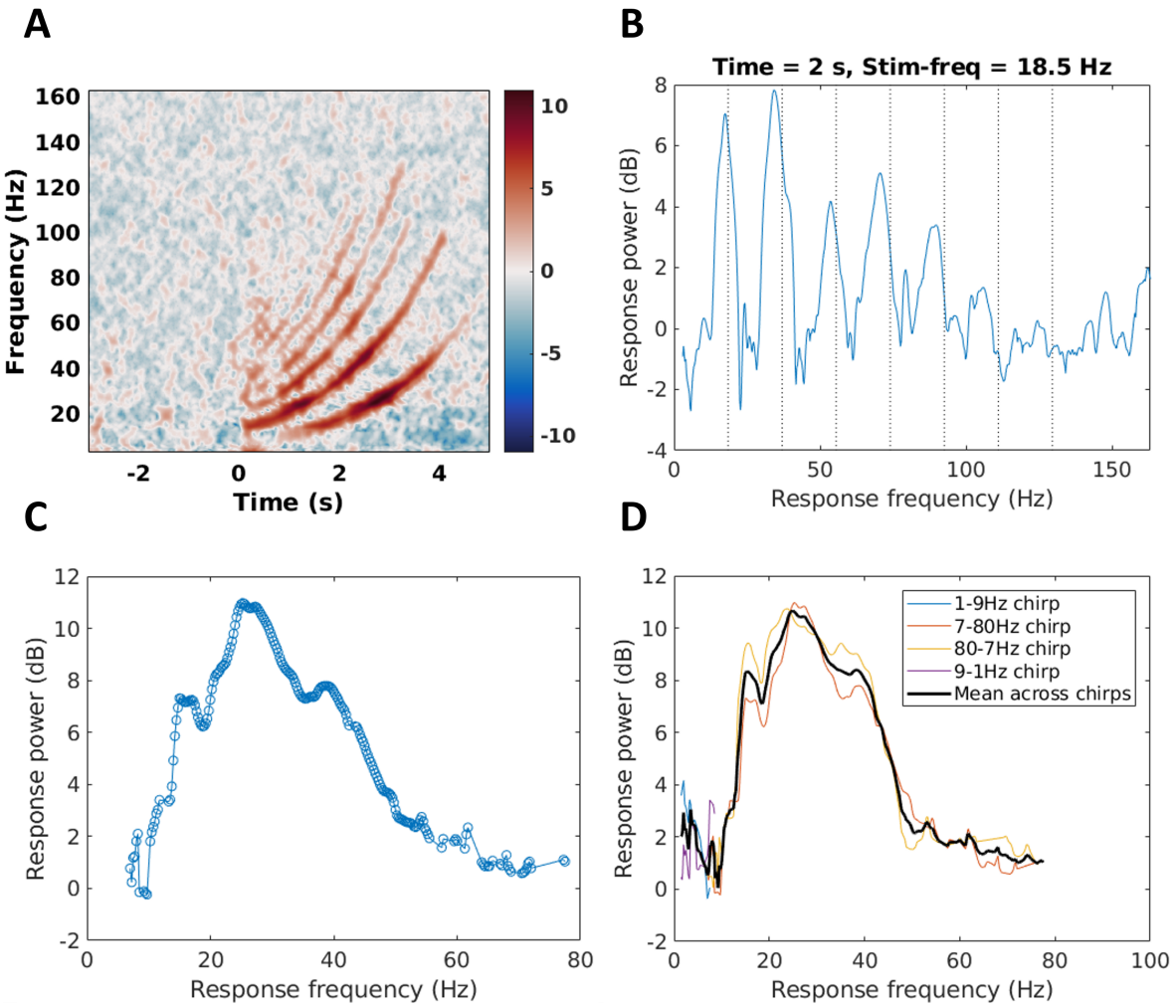

Figure 2.4: **Illustration of the visual chirp data analysis process using an example data set.**
(A) The time-frequency representation (TFR) of an example participant when viewing the 7-80 Hz visual chirp. Colours represent the response power in dB. Chirp-driven responses up to the sixth harmonic can be visually identified as red curves. **(B)** An example response spectrum extracted from the TFR in (A) at time = 2 s when the instantaneous stimulus frequency was 18.5 Hz. The y-axis here conveys information expressed by colours in sub-figure (A), whereas the x-axis here conveys information in the y-axis of sub-figure (A). The first seven harmonics of the instantaneous stimulus frequency are marked by dotted vertical lines. Chirp-driven responses at each harmonic are identified as the large peaks to the left of the dotted lines. **(C)** The power of fundamental responses derived from the TFR in (A). All the fundamental responses identified from response spectra like (B) were pooled and then averaged within each response frequency. **(D)** Response tuning functions derived from the four visual chirps (plotted as coloured lines) were interpolated onto a fine grid and averaged in overlapping frequency ranges to yield an overall response tuning function at this harmonic (the black curve).

four chirp types were first linearly interpolated onto a 0.1-Hz grid, and then averaged in overlapping frequency ranges to form a response tuning function covering the entire frequency range of the visual chirps (as demonstrated in Figure 2.4D).

2.3 Results

2.3.1 Temporal response tuning profile

The group-level temporal response tuning profiles in the fixed-frequency flicker and visual chirp tasks at each harmonic were obtained by averaging the tuning functions across participants. Figure 2.5 summarises the response profiles from the two tasks in two ways. Sub-figures A and C illustrated the neural response power as a function of stimulus frequency to assess what driving frequency evoked the strongest response. Whereas sub-figures B and D plotted the response tuning functions against response frequency to assess at what frequency the evoked oscillations in the visual cortex were the strongest.

Despite a lower frequency resolution, the fixed-frequency flicker response profiles were highly similar to the visual chirp profiles. The main difference between the responses to the two types of stimuli was that the responses at all harmonics in the visual chirp task showed a decrease in power at the response frequency of around 10 Hz (as seen in Figure 2.5D), and this was not found in the responses to fixed-frequency flickers. This is likely an artefact due to the different baseline correction methods used in the two tasks. Intrinsic alpha oscillations around 10 Hz are suppressed during stimulus viewing - a phenomenon known as event-related desynchronisation (ERD) (Pfurtscheller et al., 1994). The ERD was apparent in the visual chirp response profiles because the visual chirp data were baseline corrected against the pre-stimulus fixation period. Compared to the fixation period, less intrinsic alpha activity was present during flicker viewing, thus resulting in a dip in the response tuning function at around 10 Hz. The ERD was not apparent in the fixed-frequency flicker response profiles because the data were not contrasted to the pre-stimulus period. Instead, the SNR of responses was computed based on the amplitude at adjacent frequencies in the response spectra of the stimulus period. The ERD is not shown using this method of baseline correction. Other than the difference in the ERD, response profiles of the two tasks were highly consistent.

Plots A and C in Figure 2.5 indicated that visual stimuli at 25-35 Hz drove the strongest fundamental response, with a peak at 29 Hz. The response profile of the second harmonic had a broader peak than the fundamental, reaching maximal responses with stimuli of 15-35 Hz and peaking at 28 Hz. Stimuli lower than 35 Hz elicited a second harmonic response of a similar or higher magnitude than the fundamental response,

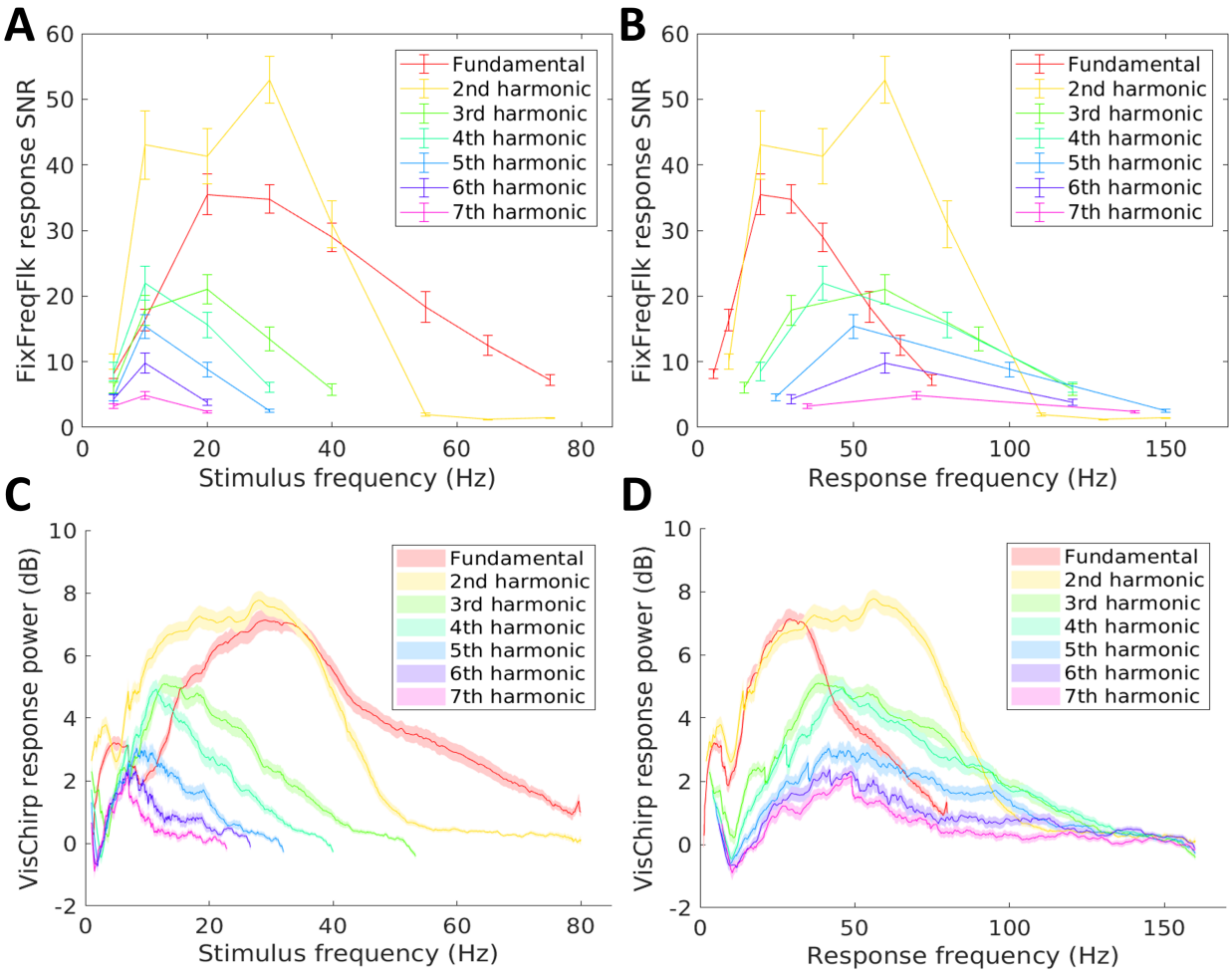

Figure 2.5: **Group average response profiles in the fixed-frequency flicker and visual chirp tasks.**
Error bars in (A) and (B) and shaded areas in (C) and (D) represent $Mean \pm 1SE$. **(A) and (C)** illustrate, for fixed-frequency flickers and visual chirps respectively, the average response power against the stimulus frequency driving the responses. For example, at the stimulus frequency of 30 Hz, the fundamental is a response at 30 Hz while the second harmonic is a response at 60 Hz. **(B) and (D)** illustrate, for the two tasks respectively, the average response power against response frequency. For example, at the response frequency of 20 Hz, the fundamental response is driven by a 20-Hz stimulus while the second harmonic response is driven by a 10-Hz stimulus.

whereas, with stimuli higher than 35 Hz, the fundamental response was stronger than the second harmonic. Beyond the second harmonic, the higher the harmonic order, the weaker the response.

Plots B and D in Figure 2.5 illustrated at what frequency the visual cortex responded the most strongly and showed that the fundamental response was strongest at around 30 Hz (29 Hz), and the second harmonic response had a broad peak at 25-65 Hz. The fundamental and second harmonic responses were of a similar magnitude at frequencies

lower than 35 Hz; after that, the second harmonic was stronger than the fundamental. The third to seventh harmonics had decreasing power but all peaked at around 45 Hz, even though at this response frequency the different harmonic components were elicited by different stimulation frequencies. In other words, higher harmonic responses were strongest around 45 Hz regardless of the stimulus driving the response. There appeared to be a resonance phenomenon around 45 Hz among third and higher harmonic responses.

2.3.2 Cross-task repeatability

To assess the extent to which the visual chirp responses could adequately represent the tuning profile in response to fixed-frequency flickers, correlation analyses were carried out between each participant's response tuning functions resulting from the two types of stimuli. These analyses provide a means to quantify the similarity of the tuning functions in response to the two stimulus types.

Visual chirp responses at the eight frequencies of fixed-frequency flickers were extracted to form a down-sampled visual chirp response tuning function. For each participant and each harmonic, Pearson's correlation coefficient was calculated between the down-sampled visual chirp tuning function and the fixed-frequency flicker tuning function (Figure 2.6). One-sample t-tests were then conducted to assess whether the correlation coefficients at each harmonic were different from zero (results in Table 2.3).

Harmonic	Mean	SD	t(36)	p	p_{adj}
1	0.79	0.13	38.01	$< .001^{***}$	$< .001^{***}$
2	0.91	0.06	95.23	$< .001^{***}$	$< .001^{***}$
3	0.70	0.27	15.56	$< .001^{***}$	$< .001^{***}$
4	0.70	0.32	13.41	$< .001^{***}$	$< .001^{***}$
5	0.69	0.44	9.61	$< .001^{***}$	$< .001^{***}$
6	0.44	0.64	4.15	$< .001^{***}$	$.001^{**}$
7	0.27	0.65	2.50	$.017^{*}$	.120

Table 2.3: **Results of t-tests comparing correlation coefficients to zero**
Note. Pearson's correlation coefficients were computed between each participant's response tuning functions resulting from fixed-frequency flickers and visual chirps. Each row displays the mean and SD of the correlation coefficients and the results of a one-sample t-test comparing the correlation coefficients to zero. The table shows both uncorrected p-values and p-values adjusted by Bonferroni corrections for multiple comparisons. $^{*}p < .05$, $^{**}p < .01$, $^{***}p < .001$.

For most participants and at most harmonics, response tuning functions of the two tasks had a strong positive correlation. One-sample t-tests showed that the correlation

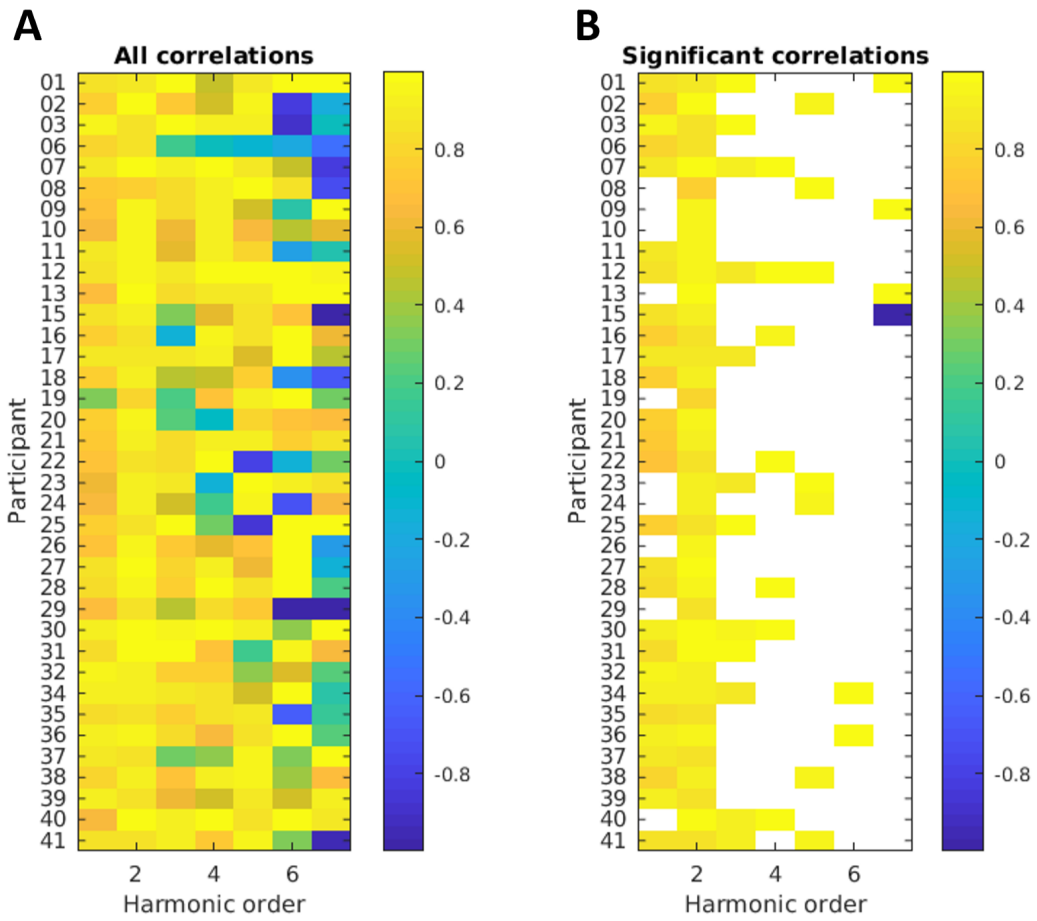

Figure 2.6: **Within-subjects correlations between the response profiles of fixed-frequency flickers and visual chirps.**
(A) For each participant at each harmonic, the colour in the cell shows the Pearson's correlation coefficient between the response profile of fixed-frequency flickers and the down-sampled response profile of visual chirps. **(B)** For correlations where $p < .05$ (uncorrected for multiple testing), the correlation coefficients are shown as the colour in cells. Cells of non-significant correlations are white.

coefficients at fundamental and harmonics up to the sixth order were all significantly higher than zero. This indicated that the response profiles of the two tasks were largely similar.

The response tuning profiles at the fundamental and second harmonic showed the highest cross-task repeatability. In particular, the similarity between the two tasks was the strongest at the second harmonic, with correlation coefficients significantly higher than for the fundamental responses, $t(36) = 5.96, p = 7.88 \times 10^{-7}$. The correlations became weaker and less significant at higher harmonic orders. This could be for two reasons. First, many participants had little response at high harmonic orders. Second, there are fewer data points in the correlation with increased harmonic order. Since only the responses between 1-160 Hz were analysed, there are eight data points in the tuning

function of the fundamental response, but only three data points (responses driven by the 5-, 10- and 20-Hz stimuli) in the tuning functions of the sixth or seventh harmonic.

Overall, the strong positive correlations between the responses in the two tasks showed that, at the level of individual participants, the two types of flicker stimuli resulted in similar response patterns; visual chirp responses are an adequate analogue to the VSSR elicited by fixed-frequency flickers.

2.3.3 Individual variability

Individual variability in the response tuning profile

As shown earlier, visual chirp responses can adequately represent the responses evoked by fixed-frequency flickers and have a much higher frequency resolution. Therefore, visual chirp response tuning functions were analysed to explore the individual differences in participants' response tuning profiles.

The response power in each tuning function of each participant at each harmonic was re-scaled to a range of 0 to 1 so that the response patterns can be compared across participants. In order to visualise individual tuning functions in a way that groups together participants with similar response profiles, hierarchical clustering analyses using Euclidean distance and average linkage were conducted at each harmonic. Clustered individual response profiles at the first seven harmonics are illustrated in Figure 2.7.

Figure 2.7A showed that many participants had a similar fundamental response pattern. Most participants had the strongest response in the range of 20-40 Hz. This response peak was relatively broad in most participants, with the highest 60% of the response spanning approximately 20 Hz. However, there was substantial variability on the width of the response peak. Some participants also had one or more smaller local peaks in addition to the most prominent peak response. Over a third of the participants had a secondary response peak in the gamma range between 40-70 Hz. The frequency at which the fundamental response diminished below 30% of the maximal varied considerably across participants, ranging from under 40 Hz to over 80 Hz.

The peak of the second harmonic response varied across participants from 15 Hz to 70 Hz. The width of the response peak also varied considerably. By contrast, the response diminished in a comparatively consistent manner to below 30% of the maximal at around 80-100 Hz.

The strongest response of the third and fourth harmonics occurred in the range of 30-70 Hz. Responses at harmonics of higher orders were not robust in many participants, thus the response patterns seemed noisier with the tuning profile and the frequency of the peak response becoming less consistent across participants.

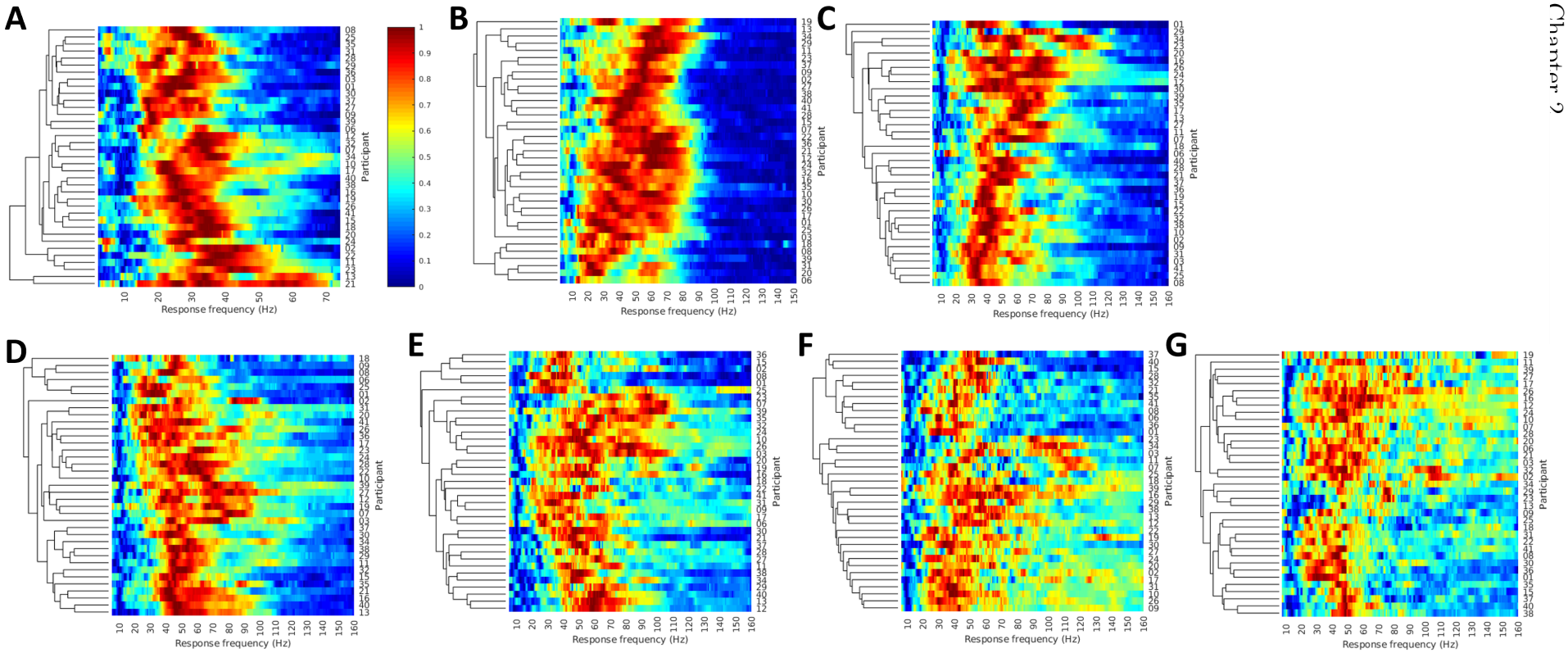

Figure 2.7: **Re-scaled visual chirp response tuning functions of each participant.**
Each row in the heatmap is one participant's response tuning function, re-scaled to a range of 0 to 1, for the fundamental response (A), second harmonic (B), third harmonic (C), fourth harmonic (D), fifth harmonic (E), sixth harmonic (F) and seventh harmonic (G). Hierarchical clustering analyses were conducted to group together participants with similar response profiles, and the resultant dendrograms are plotted to the left of each heatmap.

Cross-task consistency of individual variability

The response profile varied considerably across participants in the visual chirp task. This individual variability may be a result of data noise or reflect genuine differences in the temporal tuning properties of individuals' visual systems.

To test whether the latter was the case, a differentiability measure, D_{self}, similar to the methods described by da Silva Castanheira et al. (2021), was calculated for each participant. Let N be the total number of participants. First, an $N \times N$ correlation matrix was created for each harmonic, with each row containing the Pearson's correlation coefficients between the fixed-frequency flicker response tuning function of a particular participant and the down-sampled visual chirp tuning functions of all participants in the cohort. Then the D_{self} score differentiating participant i (P_i) in task-A from all participants in task-B can be calculated as the z-score of P_i's correlation to themselves between the two tasks ($Corr_{ii}$) with respect to the correlations between P_i's task-A response and each participant's task-B response, noted: $D_{self} = (Corr_{ii} - \mu_{ij})/\sigma_{ij}$, where μ_{ij} is the mean of correlations between P_i's task-A response and each participant's task-B response (i.e., the mean along the i^{th} row or column of the correlation matrix), and σ_{ij} is the standard deviation of the same correlations. For each participant at each harmonic, a D_{self} score can be calculated to differentiate the correlation between their fixed-frequency flicker and visual chirp responses from the correlation between their fixed-frequency flicker and the cohort's visual chirp responses (i.e., along the rows in the correlation matrix) and another D_{self} score can be calculated to differentiate the correlation of their responses from the correlation between their visual chirp response and the cohort's fixed-frequency flicker responses (i.e., along the columns in the correlation matrix). A large D_{self} score suggests that the participant's response in task A is more similar to their own response in task B than to other participants' task-B responses, thus they can be easily differentiated from other participants. A small D_{self} score, on the other hand, indicates that it is difficult to differentiate a participant's response from others in the cohort.

D_{self} scores were calculated for each harmonic. In addition, D_{self} scores were also calculated from a total correlation matrix where the correlation coefficients in the correlation matrices of all seven harmonics were summed, because the differentiability of an individual's response tuning profile might be improved by taking into account the response pattern in all harmonics. One-sample t-tests were conducted to assess whether participants' D_{self} scores were significantly different from zero.

As seen in Table 2.4, at most harmonics and from the total correlation matrices, participants' differentiability scores were significantly higher than zero, indicating that a given participant's response tuning function is differentiable from other participants

Harmonic	From task	Mean	SD	$t(36)$	p	p_{adj}
1	FFF	0.88	0.57	9.42	$< .001^{***}$	$< .001^{***}$
	VC	0.97	0.65	9.17	$< .001^{***}$	$< .001^{***}$
2	FFF	0.93	0.37	15.39	$< .001^{***}$	$< .001^{***}$
	VC	1.12	0.44	15.65	$< .001^{***}$	$< .001^{***}$
3	FFF	0.50	0.84	3.59	$.001^{**}$	$.016^{*}$
	VC	0.65	0.70	5.64	$< .001^{***}$	$< .001^{***}$
4	FFF	0.44	0.69	3.87	$< .001^{***}$	$.007^{**}$
	VC	0.53	0.88	3.70	$.001^{**}$	$.012^{*}$
5	FFF	0.61	0.83	4.48	$< .001^{***}$	$.001^{**}$
	VC	0.48	1.01	2.90	$.006^{**}$	.101
6	FFF	0.52	0.90	3.51	$.001^{**}$	$.019^{*}$
	VC	0.47	0.88	3.26	$.002^{**}$	$.039^{*}$
7	FFF	0.26	0.77	2.05	$.047^{*}$	.756
	VC	0.23	0.94	1.50	.144	1.000
Total	FFF	0.93	0.63	8.97	$< .001^{***}$	$< .001^{***}$
	VC	0.90	0.90	6.06	$< .001^{***}$	$< .001^{***}$

Table 2.4: **Results of t-tests comparing differentiability scores to zero**
Note. From the correlation matrix for each harmonic and from the total correlation matrix summing the correlation matrices of all harmonics, a differentiability score, D_{self}, was computed for each participant to differentiate their visual chirp response from all participants' fixed-frequency flicker responses. These D_{self} scores are shown in the rows "From task FFF". A D_{self} score was also calculated for each participant to differentiate their fixed-frequency flicker response from all participants' visual chirp responses, as summarised in rows "From task VC". Each row displays the mean and SD of the D_{self} scores and the results of a one-sample t-test comparing the D_{self} scores to zero. The table shows both uncorrected p-values and p-values adjusted by Bonferroni corrections for multiple comparisons. $^{*}p < .05$, $^{**}p < .01$, $^{***}p < .001$.

based on their tuning function in the other task. The cross-task differentiability was lower at higher-order harmonics. The D_{self} scores were not significantly different from zero at the seventh harmonic and in one differentiation direction at the fifth harmonic.

Although most of the D_{self} scores were significantly higher than zero, the values were relatively low compared to more easily differentiable individual data reported in previous studies as neuronal fingerprints with D_{self} scores around 4 (da Silva Castanheira et al., 2021). D_{self} scores in the current study were relatively close to zero, indicating that distinguishing each participant's response tuning profiles was somewhat difficult. This could be the result of two reasons. First, participants' response profiles in one task were very different to their own response profiles in the other task. Second,

the response profiles were too similar across participants. The small values of D_{self} scores at lower-order harmonics were likely due to the highly similar response profiles across participants, as indicated by Figure 2.7 and by strong correlations between participants' response tuning functions, especially in the first four harmonics (correlation matrices can be found in Appendix 1). Whereas at high-order harmonics, responses were usually weak and sometimes absent. Thus, the response tuning functions might be contaminated by data noise. This could lead to varied response profiles within the same participant across tasks, resulting in low differentiability scores.

Despite the generally low D_{self} values, the significantly higher-than-zero scores overall suggested that individual participants' response profiles were adequately unique across tasks to distinguish individuals from the rest of the cohort. This suggests that the individual differences in the response tuning functions were not merely noise in the data, but reflect meaningful and consistent variability in the temporal tuning functions, potentially indexing properties of the individual's visual cortex.

2.4 Discussion

The aim of the current study was to establish a tuning profile of the VSSR power in response to a wide range of finely-sampled stimulation frequencies, as such a comprehensive tuning function is both conceptually important for understanding the dynamical properties of the human visual system and methodologically useful in informing the choices of stimulation frequencies in future frequency-tagging studies.

Frequency-tagging studies typically use fixed-frequency flickers, but using them to test a large number of stimulation frequencies is extremely time-consuming. Thus the current study used visual chirp stimuli to efficiently establish the response tuning profile to a wide range of stimulation frequencies (1-80 Hz) at a fine sampling resolution (0.5 Hz). Besides visual chirps, fixed-frequency flickers of several frequencies were also tested to assess whether the two types of stimuli yielded analogous response tuning functions. After confirming that chirp-evoked responses were an adequate approximation to the VSSR elicited by fixed-frequency flickers, the temporal response tuning profile was both characterised at a group level and evaluated in terms of individual differences.

2.4.1 Chirp-evoked responses versus VSSR

Visual chirps and conventionally used fixed-frequency flickers yielded highly similar temporal response tuning profiles both at the group level, as seen in Figure 2.5, and at the individual level, as indicated by the strong within-subjects correlations between response tuning functions of the two tasks. These findings provide strong evidence that

chirp-evoked responses are an adequate analogue to the VSSR evoked by flickers of fixed frequencies, and therefore can be used as an efficient alternative to assess the responses of the human visual system to a large number of visual temporal frequencies.

2.4.2 Fundamental responses

At the group level, visual stimulation at around 30 Hz led to the strongest fundamental response. This is consistent with the findings of Lithari et al. (2016)'s study but disagrees with other previous studies summarised in Table 2.1. In particular, most past studies found the most prominent fundamental response in the alpha range (8-12 Hz; Bakardjian et al., 2010; Bayram et al., 2011; Chen et al., 2019; Fawcett et al., 2004; Gulbinaite et al., 2019; Herrmann, 2001; Koch et al., 2006; Kuś et al., 2013; Lazarev et al., 2001; Lea-Carnall et al., 2016; Lin et al., 2012; Salchow et al., 2016; Srinivasan et al., 2006) or low beta range (14-16 Hz; Chen et al., 2019; Floriano et al., 2019; Kuś et al., 2013; Pastor et al., 2007; Pastor et al., 2003), sometimes with smaller local peaks in various other frequency ranges. In addition to studies described in Table 2.1, a few studies presented observers with broadband flickers and computed a temporal response function by cross-correlating between the stimulation frequency and M/EEG responses. These studies observed heightened response power in alpha band (known as an alpha echo; J. Jia et al., 2017; VanRullen & Macdonald, 2012; Zhigalov et al., 2021) and gamma band (gamma echo; Zhigalov et al., 2021). These response functions driven by broadband flickers agree with the results of many aforementioned studies presenting narrow-band flickers, but the current study did not observe heightened response power in the alpha or gamma band on the group level.

The inconsistency between the current and previous studies and among the previous findings may be the result of differences in stimuli and experiment designs. For example, several past studies only tested stimulation frequencies below 30 Hz, thus directly limiting the resultant response peaks to the low-frequency range tested. Moreover, the current and past studies vary substantially in the apparatus used to present flickers, stimulus attributes, and the method of quantifying response magnitude. All these factors have been previously shown to modulate the VSSR profile (Bieger & Garcia-Molina, 2010; Chen et al., 2019; Kuś et al., 2013; Labecki et al., 2016; Lea-Carnall et al., 2016; Lin et al., 2012; Salchow et al., 2016; Solf et al., 2020; Zhu et al., 2010). Among the past research summarised in Table 2.1, Lithari et al. (2016)'s study is the only one using the same presentation apparatus and similar stimulus as the current study, it is also the only past study that found the peak fundamental response at around the same frequency as the current study.

It is likely that there are different temporal response tuning functions when different

photoreceptors (rods or cones) and visual pathways (magnocellular or parvocellular) are stimulated. Rods are sensitive to low-luminance stimuli; at such scotopic light levels, a relatively long temporal integration period is required to accumulate the sparse photon flux, resulting in a low temporal resolution of rod responses (Donner, 2021; Schiller & Tehovnik, 2015b). In contrast, cones function at photopic light levels and have relatively short temporal integration periods, enabling cones to detect fast-changing stimuli (Schiller & Tehovnik, 2015b; Wandell, 1995). Therefore, flickers presented at photopic luminance levels can stimulate cones and elicit photoreceptor responses up to a higher temporal frequency, compared to low-luminance stimuli that mainly drive rods. Moreover, different types of retinal ganglion cells also have different temporal properties. While the parasol ganglion cells feeding retinal outputs to the magnocellular visual pathway are capable of generating transient and fast responses, midget ganglion cells generate more sustained output responses, and as a result, the parvocellular visual pathway receiving inputs from midget ganglion cells can only process stimuli at low temporal frequencies (Donner, 2021; Schiller & Tehovnik, 2015a). Due to the different spatial distributions of parasol and midget ganglion cells in the retina, the stimulus size and location in the visual field can affect which visual pathway is stimulated. Inputs in the central fovea are exclusively processed by midget ganglion cells, whereas parasol ganglion cells are more abundant in the periphery (Schiller & Tehovnik, 2015a). Thus, a large and/or peripheral stimulus would elicit stronger VSSR at high frequencies than would a small and foveal stimulus. Given that past studies have used a wide range of stimulus luminance, size and location, it is unsurprising that the observed temporal response tuning functions varied largely across studies. My current experiment used a high-luminance stimulus, hence most likely saturating rods and driving only cones (Cao et al., 2010). Cones sensitive to short, middle and long wavelengths should all be stimulated by my achromatic (white) stimulus. The large flickering area spanning across foveal and peripheral visual fields should have driven both parvocellular and magnocellular pathways. The stimulation of cones and both visual pathways enabled neural responses to both low and high temporal frequencies, as demonstrated by the VSSR tuning profile reported earlier.

Since the luminance, colours, size and retinal location of flickers can all affect the VSSR tuning profile, and frequency-tagging studies use flickering stimuli at various sizes and locations, future frequency-tagging experiments should take an empirical approach to determine the flicker frequency that elicits the strongest neural responses, by implementing a visual chirp in the stimuli of the study to establish a VSSR tuning function specific for such stimuli. Further research is also needed to systematically control the various aspects of stimulus set-up to comprehensively investigate how they influence the VSSR tuning profile.

2.4.3 Harmonic responses

The current study characterised the temporal response tuning profiles to stimulation of 1 to 80 Hz at the first seven harmonics, a topic that most previous studies treated in far less detail. At the group level, the second harmonic power had a broad peak when the stimulation frequency was 15-35 Hz. While most previous studies comparing the VSSR at different stimulus frequencies only focused on the fundamental responses, the studies that did report second harmonic response profiles showed inconsistent results, and all are different to the findings of the current study. Two past studies found that among stimulus frequencies of 5-40 Hz, the lower the stimulus frequency, the greater the second harmonic response (Chen et al., 2019; Pastor et al., 2007), which is the opposite pattern observed in the current study in the same range of stimulus frequencies. Two studies showed that the strongest harmonic response occurred when either the stimulus frequency (Gulbinaite et al., 2019) or the harmonic response frequency (Lazarev et al., 2001) was in the alpha band. Yet other studies found the strongest second harmonic to be driven by stimuli of 12-15 Hz (D. Jia et al., 2019; Lithari et al., 2016; Perenboom et al., 2020).

At harmonics higher than the second order, the current study observed a resonance phenomenon around the response frequency of 45 Hz. This has not been reported before. The preferred oscillation frequency in a sensory system may have functional implications for the neuronal processing in this modality. For example, computational modelling and empirical testing have suggested that the cortical resonance frequency of a network is determined by the size of the activated network, the number of connections within the network and the transmission delay between units of the network (Lea-Carnall et al., 2016).

With respect to the relative magnitudes of fundamental and harmonic components, the second harmonic response was found to be stronger than the fundamental response when the stimulus frequency was below 35 Hz. Whereas stimuli above 35 Hz evoked stronger fundamental than harmonic responses. Moreover, the response tuning profile at the second harmonic showed the most robust cross-task repeatability, more so than the fundamental response (see Figure 2.6). In contrast, most previous studies found stronger fundamental responses than second harmonic responses (e.g., Chen et al., 2019; Gulbinaite et al., 2019; D. Jia et al., 2019; D. Jia et al., 2017; Pastor et al., 2007; Waytowich & Krusienski, 2016). However, a few studies reported that most participants had a stronger harmonic response than the fundamental (Heinrichs-Graham & Wilson, 2012; Lazarev et al., 2001), at least in response to a particular range of stimulation frequencies (Lithari et al., 2016).

This mixed pattern of results relating to harmonic power may be due to differences

in stimulus attributes in different studies. For example, it has been proposed that, compared to foveal stimulation, peripheral stimuli and simultaneous foveal and extrafoveal stimulation could increase the likelihood of a larger VSSR response at the second harmonic than at the fundamental (Solf et al., 2020). This is consistent with the findings of the current study where a large flicker stimulated both the foveal and parafoveal regions and the strongest response was observed at the second harmonic for stimulus frequencies below 35 Hz.

Another possible reason for the strong second harmonic response in the current study is that, as illustrated in Figure 2.1, the luminance of the flicker stimulus oscillated between black and white on a mid-grey background. This means that twice in each cycle when the stimulus luminance was 0.5, the stimulus had the same luminance as the background thus transiently "disappearing" from the screen. In other words, in each cycle, two visual stimuli (one white and then one black) appeared to emerge from the mid-grey background. This twice-per-cycle occurrence could drive the visual system at twice the frequency as the luminance modulation, thus evoking a response at twice the intended stimulus frequency and contributing to the response power at the second harmonic frequencies. This is similar to the studies evoking VSSR using a square-wave reversing checkerboard stimulus (e.g., Fawcett et al., 2004). In a cycle of the stimulus, a pixel that started white would change colour to black halfway into the cycle and then back to white at the beginning of the next cycle. This meant that the checkerboard would reverse colour twice in each cycle. Such stimuli were found to evoke strong VSSR at the second harmonic of the stimulus frequency rather than at the fundamental frequency. In the current study, strong responses were found at both the fundamental and second harmonic frequencies. It is possible that the stimulus used in the current study drove different neuronal populations at the fundamental frequency and at twice this frequency.

Finally, the profile of VSSR harmonic responses may be affected by not only stimulus attributes but also the perceptual and cognitive processing involved in the visual task. There has been evidence suggesting that harmonic responses have different functional roles than fundamental responses. It is frequently observed that fundamental and harmonic responses have differential topographical distributions, indicating that they originate from different neuronal populations, especially during cognitive tasks such as face discrimination and attention (Gulbinaite et al., 2019; Heinrichs-Graham & Wilson, 2012; Y. J. Kim et al., 2011; Liu-Shuang et al., 2014; Pastor et al., 2007; Perenboom et al., 2020). Fundamental and harmonic responses are also differentially affected by cognitive modulations, for example, visual-spatial attention was shown to modulate the magnitude of the second harmonic but not the fundamental (Y. J. Kim et al., 2011). It has been proposed that harmonic responses may serve complementary functions to

the fundamental response (J. W. Kim & Robinson, 2007; Norcia et al., 2015). Therefore, tasks that require different perceptual and cognitive processing are likely to evoke different harmonic profiles. In the current study, participants performed only passive viewing and no cognitive task, thus the harmonic response pattern reported here cannot be applied to frequency-tagging studies involving higher-level visual processing.

2.4.4 Individual variability

Both the current study and previous research have observed considerable variability in the temporal response tuning functions between individuals (Gulbinaite et al., 2019; Heinrich, 2010; Herbst et al., 2013; Kuś et al., 2013; Lazarev et al., 2001; Ramos-Junior et al., 2011; Solf et al., 2020). With a large extent of individual variability, group-level response tuning profiles averaged across individuals can be skewed and unreliable when the sample size is small. This could have contributed to the difference between the findings of the current study and those reported in past studies with typically small sample sizes.

Furthermore, given the substantial individual differences, group-averaged results are not sufficient for a comprehensive understanding of the VSSR tuning profile in the human visual cortex. The current study characterised the individual differences in much greater detail than previous work. Individual tuning functions (Figure 2.7) revealed patterns that were hidden by the group-averaged response profiles (Figure 2.5). For example, in the fundamental component of chirp-evoked responses, over a third of the participants had a secondary peak response in the gamma range in addition to the most prominent response around 30 Hz. At the second harmonic, while the group-averaged response tuning function showed a broad peak at 25-65 Hz, most individual observers had a much narrower response peak, and the peak response frequency varied across the range of 20-70 Hz. It was also revealed that the extent of individual variability was different for different harmonics, with the second harmonic response having the most consistent pattern across individuals.

Importantly, the individual differences in tuning profiles were repeatable across tasks, especially at the first three harmonic components, as shown by the strong within-subject correlations between the tuning functions from the two tasks. Moreover, the greater-than-zero cross-task differentiability scores indicated that individuals' response tuning profiles were also distinctive, so that a given observer's response in one task can be distinguished from others in the cohort based on this observer's response pattern in the other task. The repeatability and distinctiveness of individual response profiles indicated that the individual differences are more than random noise, instead, they could reflect intrinsic properties of an individual's visual system.

Therefore, features of the temporal response tuning profile have the potential to be biomarkers with functional relevance. Further research can assess the relationship between features of the temporal response profile and other properties of an individual's visual system, for example, the endogenous alpha oscillation frequency, the peak frequency of visually induced gamma oscillations, the perceptual threshold for flickers (the critical flicker fusion threshold), and the microstructure and connectivity of the visual cortex. In addition to the response power and spectral properties at each harmonic component of VSSR, further individual differences analyses can assess the relative magnitudes among different harmonic components and if that is associated with anatomical or connectivity properties of the visual cortex.

Large individual differences also have methodological implications for using VSSR in frequency-tagging studies or as a potential intervention for Alzheimer's disease (AD). Such applications require selecting stimulation frequencies that maximise the evoked responses, but the stimulation frequency that yields a response peak in the group-level tuning function may not be the optimal stimulus frequency for many, if not most, individuals. Given that the VSSR tuning function can be specific to the individual, the stimulus attributes and the study set-up, to achieve maximal VSSR in all participants of a frequency-tagging study or intervention, it is best to use the particular stimulus and apparatus to establish a response tuning function for each individual. This can be quickly and efficiently conducted using visual chirp stimuli, as demonstrated in the current study.

2.4.5 Limitations

Analyses in the current study were done in the sensor space on the averaged signals of all occipital channels. Several previous studies suggested that different harmonic components of the VSSR response originated from different neuronal populations and could serve different functions in visual processing. It would therefore be important for further analyses to reconstruct the signals in the source space. It has also been proposed that stimulation of different frequencies may evoke the most potent response in different cortical regions (Chai et al., 2019; Lea-Carnall et al., 2016). Source-space analyses of the current rich data set could therefore add valuable insights to our understanding of the neuronal processing of dynamic visual stimuli.

2.4.6 Conclusions

In conclusion, the current study demonstrated that visual chirps evoke neuronal responses closely approximating the VSSR evoked by fixed-frequency flickers, and thus can be used as an alternative to fixed-frequency flickers to efficiently measure the re-

sponse power to a large number of stimulation frequencies. Using visual chirps, a finely-sampled temporal response tuning profile was established at the first seven harmonic components for stimuli of 1-80 Hz. This group-level response tuning profile can inform the choice of stimulation frequencies in future frequency-tagging studies. Moreover, considerable individual variability was observed in the temporal response tuning functions. Such individual differences were repeatable within-subjects and distinctive between-subjects, therefore likely to reflect intrinsic properties of an individual's visual system and can potentially be used as a biomarker for the dynamic processing in the visual system.

Chapter 3

Relationships between the temporal response tuning profile and other properties of the visual system

3.1 Introduction

The previous chapter established a finely sampled tuning function describing the power of visual steady-state responses (VSSR) to stimulation of 1-80 Hz. This temporal response tuning profile varied substantially across individuals, and the individual variability was found to be repeatable within-subjects and distinctive between-subjects. It suggests that the individual profile of VSSR power likely reflects intrinsic properties of the neural mechanisms underpinning one's visual processing.

To explore the functional implications of the temporal response tuning profile, this chapter will test whether individuals' VSSR tuning profiles are related to other properties of the visual system. Specifically, features of the temporal response tuning profile will be assessed in relation to the individual variability in two aspects of visual processing: first, the critical flicker fusion (CFF) threshold, which indexes the limit of an individual's temporal resolving ability (Brenton et al., 1989); and second, the peak frequency of visually-induced gamma oscillations, which is thought to be determined by intrinsic synaptic properties of the microcircuitry in the visual cortex (Shaw et al., 2017).

3.1.1 Temporal response tuning profile and CFF

The limit of an observer's temporal-resolving ability can be measured by the perceptual threshold above which a fast train of visual stimuli is likely perceived as static rather than flickering (the critical flicker fusion threshold, CFF). It has long been used to

index the temporal resolution and thus determine the neural efficiency of an individual's visual system, especially in clinical populations (Brenton et al., 1989; Brown et al., 2018; Kircheis et al., 2002; Mankowska et al., 2021; Peters et al., 2020). The CFF threshold can vary substantially between individuals depending on the observer's age and health (Misiak, 1951; Sharma et al., 2007). It can also vary within the same observer with varied levels of alertness and cortical arousal (Mankowska et al., 2021; Parrott, 1982), when varying stimulus attributes such as the retinal location, size, colour, luminance and contrast (Brown et al., 2018; Hartmann et al., 1979; Hecht & Verrijp, 1933; Liu et al., 2015) and when using different measurement methods and criteria to estimate the CFF threshold (Eisen-Enosh et al., 2017; Fernandez-alonso et al., 2019).

The temporal-resolving ability of the visual system is thought to reach its limit when multiple cycles of stimulus occur within the temporal integration period of the neurons involved in temporal summation (Barlow, 1958; Burr, 1981). While the exact physiological mechanism of the CFF remains unclear (Kahlbrock et al., 2012), it has been found that the CFF threshold is consistently lower than the highest frequency that can evoke VSSR (e.g., Herbst et al., 2013; Ramos-Junior et al., 2011). In fact, flicker frequencies that observers report not being able to perceive have been successfully used in frequency-tagging experiments (Zhigalov et al., 2019) and brain-computer interface (BCI) systems (L. Jiang et al., 2022) to drive the visual cortex while minimising visual discomfort.

It has been argued, albeit in the auditory domain, that individuated percepts of a particular temporal frequency require this frequency to be represented and processed in the sensory system (Allen, 2019). If this is the case, an individual's upper limit of VSSR responsiveness (i.e., the highest stimulation frequency that can evoke VSSR in an individual) will be a factor determining the highest frequency the individual perceives as a flicker rather than a static stimulus. In other words, this notion predicts a positive relationship between an individual's VSSR upper limit and their CFF threshold.

To my knowledge, whether this predicted relationship holds in visual perception has only been tested in one study so far (Herbst et al., 2013). No correlation was found between the participants' CFF and VSSR upper threshold, contrary to my prediction. However, the aim of that study was not to assess the relationship between CFF and VSSR; as a result, the task design was not optimal for this purpose. Herbst et al. (2013) measured the VSSR power at only 10 stimulation frequencies in the range of 7.7-165.7 Hz, and the highest stimulation frequency that evoked significant VSSR was regarded as the VSSR upper limit. Such a sparse sampling of stimulation frequencies makes it difficult to locate the precise frequency above which the VSSR diminishes for a given participant. Moreover, the CFF threshold was measured by a yes/no task, where the participant reported whether the stimulus appeared flickering or static in each trial.

This design choice is problematic because threshold indices derived from yes/no tasks are known to be contaminated by response biases (Kingdom & Prins, 2016).

Thus, the current study adopted a design that derived the upper limit of VSSR from a finely sampled temporal response tuning profile (as described in Chapter 2) and measured the CFF using a criterion-free 2-interval forced choice (2IFC) task. In addition to assessing the relationship between the CFF and the upper limit of VSSR, the current study will also explore whether the CFF relates to other aspects of the temporal response tuning profile. I will assess the relationship between CFF and the resonance frequency of the visual system (frequency of the strongest VSSR) and analyse whether CFF is particularly related to certain parts of the temporal response tuning function by relating the CFF to the VSSR power at each response frequency in the temporal response tuning function.

3.1.2 Temporal response tuning profile and visual gamma

As introduced in Chapter 1, visual gamma oscillations are heightened neural activities at 30-80 Hz induced by intense visual stimuli such as black and white gratings (Adjamian et al., 2004). Features of one's visual gamma oscillations, such as the peak frequency, have been shown to reflect intrinsic properties of an individual's visual system, as does the temporal response tuning function of VSSR. Even though VSSR and visual gamma belong to two different categories of oscillations (VSSR are evoked responses phase-locked to the stimulus, whereas visual gamma rhythms are induced oscillations occurring in response to but not phase-locked to the stimulus), both are involved in feedforward visual processing. It has been proposed that VSSR, especially those evoked by periodically modulated low-level visual attributes, are the temporal superposition of transient event-related potentials (ERPs) (Capilla et al., 2011) or the result of neuronal oscillators entrained by an external stimulus train (Thut et al., 2011). Either way, VSSR represents sensory stimulation in primary visual cortex and reflects bottom-up sensory processing (Norcia et al., 2015). On the other hand, gamma oscillations have been shown in both monkey and human brains to propagate from V1 to downstream areas like V4 and convey feedforward information flow across the visual cortex (Bastos et al., 2015; Jensen et al., 2015; Michalareas et al., 2016; van Kerkoerle et al., 2014). Given that both the VSSR and visual gamma play a role in supporting feedforward visual processing, relationships may be expected between the features of an individual's VSSR tuning profile and the features of their visual gamma oscillations. An understanding of how the two relate to each other could shed light on the way evoked and induced oscillations interact in feedforward sensory processing.

While there are arguments suggesting that there might be a relationship between

VSSR and visual gamma, the literature on this topic is mixed, with some studies indicating a dissociation between the underlying mechanisms. For instance, the Pyramidal INterneuron Gamma (PING) model suggests that visual gamma oscillations arise from the interactions between excitatory superficial pyramidal cells and inhibitory interneurons within the visual cortex (Börgers, 2017; Spaak et al., 2012; Xing et al., 2012). In contrast, the generation of VSSR involves information flow from visual cortex to frontal areas (Li et al., 2015) and is best modelled by large-scale models at the whole-brain level (Roberts & Robinson, 2012; Zhang et al., 2021). Therefore, properties of VSSR are thought to relate to functional and structural connectivity of a large-scale brain network (Zhang et al., 2021) whereas properties of visual gamma, such as the peak gamma frequency, are determined by the balance between coupled neuronal populations within visual cortex (Shaw et al., 2017).

In sum, the current literature on the relationship between VSSR and visual gamma is mixed, with some studies suggesting common processing involving both phenomena, while other studies point to distinct mechanisms. To date, there has not been a study that directly relates different aspects of VSSR and visual gamma responses. Therefore, the current study explores the relationship between spectral features of the VSSR temporal tuning profile and visually-induced gamma rhythms. Specifically, the peak gamma frequency will be assessed in relation to the peak VSSR frequency and the upper limit of VSSR. In addition, I will also explore whether the peak gamma frequency is particularly related to certain parts of the temporal response tuning profile by computing the correlations between the peak gamma frequency and the VSSR power at each response frequency in the VSSR tuning function. Whether or not the gamma frequency is related to particular parts or features of the temporal response tuning function can provide insights into whether and how induced and evoked responses interact in visual processing.

3.2 Methods

3.2.1 Participants

The same 37 participants who completed the visual chirp task described in Chapter 2 also completed the CFF and visual gamma tasks described in the current chapter. Each participant's testing was conducted in two sessions on different days, with the visual chirp and visual gamma tasks conducted in the first session and the CFF threshold measured in the second session.

3.2.2 Temporal response tuning function

As described in Section 2.2 of Chapter 2, participants' temporal response tuning profiles were established using the visual chirp task and derived from MEG signals of occipital channels. To index the frequency above which VSSR ceased to be evoked, a VSSR upper limit was computed for each participant. At the group level, chirp-evoked fundamental response power peaked at around 30 Hz then gradually decreased but did not completely diminish to the baseline level even at the highest stimulation frequency tested (as seen in Figure 2.5 on page 28). Thus, in this study, I defined the VSSR upper limit for each harmonic as the lowest frequency at which the response power decreased to 15% of the participant's peak response at this harmonic. This threshold was selected based on inspecting individuals' VSSR tuning functions. If the cut-off value is set too high, for example, at 20% of the peak response, instead of indicating a frequency above which the VSSR diminishes to low power, the cut-off point can be reached at a local trough in the tuning function after which the VSSR power rises again (an example is illustrated in Figure 3.1). On the other hand, the threshold cut-off cannot be set too low, for example, at 10% of the maximum response. Because for several participants, the power of their fundamental response never dropped to below 10% of the maximal response even at the highest stimulation frequency tested (80 Hz). Thus a cut-off that is too low will result in the VSSR upper limit being capped at 80 Hz for a substantial proportion of participants and restrict the variability of this measure. A cut-off threshold of 15% was optimal, as it largely avoided both problems described above.

3.2.3 CFF threshold

Stimulus

Visual stimuli were programmed using Matlab (version R2015b, The MathWorks, Natwick, MI, USA) and the Psychophysics Toolbox (version 3.0.12) (Brainard, 1997; Kleiner et al., 2007; Pelli, 1997) and presented using a PROPixx DLP LED projector at a refresh rate of 1440 Hz and a spatial resolution of 1920*1080 pixels. Stimuli were projected onto a semi-translucent screen placed 120 cm from the participants' eyes in a dark magnetically shielded room (MSR). The luminance of the presentation was 230 cd/m^2 when the entire screen was white, and 0.13 cd/m^2 when the entire presentation was black. The task measuring the CFF threshold was carried out in the same room where the MEG recording of participants' visual gamma was conducted, with an identical set-up as in the MEG recording.

The luminance-modulated flicker stimulus was a Gaussian blob, presented centrally on a mid-grey background. The flickering region was presented through a 2D Gaussian

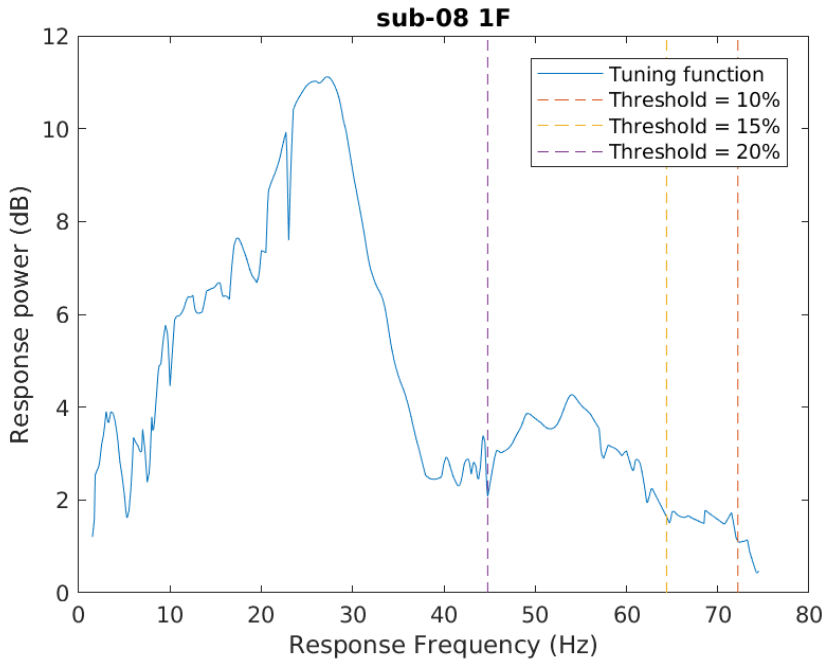

Figure 3.1: **An illustration of defining the VSSR upper limit using three cut-off thresholds.**
An example participant's temporal response tuning function at the fundamental component is plotted in blue. The purple, yellow and orange dotted lines indicate the respective frequencies at which the response power first drops to 20%, 15% or 10% of the maximal response after the maximal response. A secondary response peak in the gamma range occurs after the response power decreases to 20% of the maximal, therefore the 20% threshold cannot adequately indicate the frequency above which the VSSR diminishes to low power.

window (clipped to a diameter of 11 degrees of visual angle with a sigma of 3.15 degrees of visual angle), so there was no sharp boundary between the flickering area and the static background. At the centre of the flicker, there was a small static mid-grey disc about 0.3 degrees of visual angle in size, on which a Gaussian window blended the boundary of the static disc with the surrounding flicker. A white fixation dot was presented at the centre of the static grey disc. The luminance of the flickering region was sinusoidally modulated between black and white, as illustrated in 3.2.

Procedure

Participants' CFF threshold was measured using an adaptive staircase procedure, following the recommendation of a study comparing the three most commonly used psychophysical methods for measuring the CFF and showing that the adaptive staircase procedure was an optimal method with high test-retest repeatability and time efficiency (Eisen-Enosh et al., 2017).

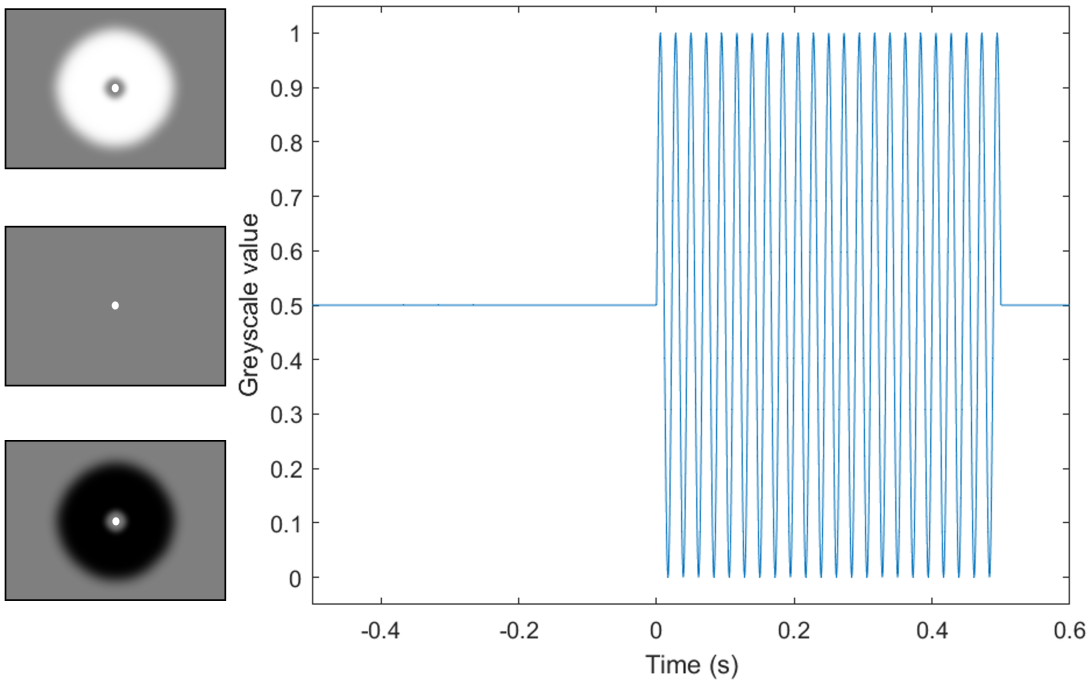

Figure 3.2: **Luminance profile of an example 45-Hz flicker.**
During the pre-interval fixation period (before stimulus onset at time 0), the stimulus region is mid-grey, same as the background. During the flicker interval (0-0.5 s), the luminance-modulated flicker varied sinusoidally between black (denoted by a greyscale value of 0) and white (denoted by a greyscale value of 1). The appearances of the white, mid-grey and black stimuli are illustrated by the three panels on the left.

Based on the procedure described by Eisen-Enosh et al. (2017), a two-interval-forced-choice (2IFC) paradigm was used, as shown in Figure 3.3. Each trial consisted of two temporal intervals, one containing a test flicker (the 'flicker interval') and the other interval containing no visible flicker (the 'static interval'). The frequency of the test flicker in each trial was determined by an adaptive staircase procedure. The order of the two intervals was randomly sampled. After viewing the two intervals, the participant was asked to report by a button-press whether the flicker occurred in the first or the second interval. Text feedback ('Correct' or 'Incorrect') was given following their response to drive participants to their best performance, so the upper limit of their temporal resolution could be measured.

As in Eisen-Enosh et al. (2017), in the static interval, instead of a static mid-grey presentation, a 120-Hz flicker was presented, which is above human's CFF thresholds and thus should be perceived as a static image (Alais et al., 2016; Eisen-Enosh et al., 2017). Because high-frequency flickers many times higher than an observer's CFF threshold can still produce luminance artefacts even though they are not perceived as flickering (Davis et al., 2015). Using a 120-Hz flicker in the static interval can prevent

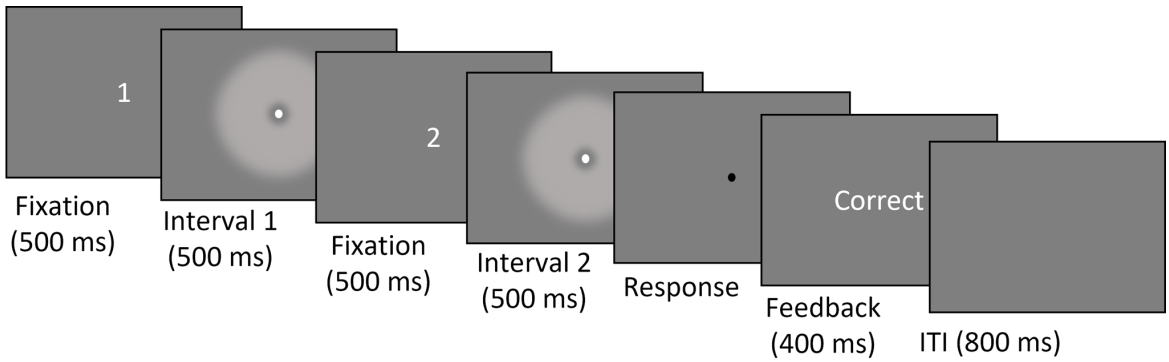

Figure 3.3: **One trial of the 2IFC task measuring the CFF threshold.** The participant views a flicker interval and a static interval and makes a key-press response to indicate in which interval they see a flicker. The number '1' or '2' is presented in the place of the fixation dot during each pre-interval fixation period to indicate which interval the participant is about to view. The fixation dot is white during the two intervals and turns black to indicate the response period. Participants receive feedback after their responses.

participants from distinguishing between the static and flicker intervals based on the presence of luminance artefacts when the stimulus in the flicker interval is above their CFF threshold.

The flicker frequency in each flicker interval was determined by an adaptive staircase procedure with a step size of 2 Hz. In the first trial of a staircase run, the flicker frequency was 45 Hz. The flicker frequency then moved up a step after each correctly responded trial until the first incorrect trial, after which a 3-up 1-down staircase rule was applied. The flicker frequency increased by 2 Hz after three consecutive correct trials and decreased by 2 Hz after each incorrect trial, yielding a CFF estimate reflecting a 79% correct response level (Eisen-Enosh et al., 2017). Four staircase runs were carried out in parallel with their trials randomly interleaved. A staircase run was terminated when the change of flicker frequency in this run had achieved 12 reversals, or when the total number of trials across all runs had reached 300. The adaptive staircase procedure was implemented using the Palamedes toolbox (Prins & Kingdom, 2018). The procedure included a self-paced break after every 50 trials.

Participants started the task with 20 practice trials where the flicker frequency in the flicker interval was fixed at 45 Hz. If necessary, the practice block was repeated until the experimenter was sure that the participant understood the task instructions.

Analysis

Due to unforeseen technical faults of the button box, false responses were recorded in some trials. In particular, responses generated by the faulty button box were recorded

instead of the responses made by participants in those corrupted trials, sometimes affecting the progression of the response-dependent adaptive staircase procedure. The corrupted trials were identified post-hoc by extremely short response times of less than 1 ms. The proportion of corrupted trials in the sample had a median of 2.33% (mean = 6.55%, SD = 9.14%). In order to eliminate the effect of corrupted trials in the CFF threshold estimation, the CFF threshold was not computed by the conventional method of averaging the last several reversals in each staircase run. Instead, after removing trials in which the response time was less than 1 ms, trials of all four staircase runs of each participant were pooled and fitted with a psychometric function (PF) using the Palamedes toolbox (Prins & Kingdom, 2018). Setting the threshold and slope measures of the PF as free parameters and fixing the guess rate and lapse rate to 0.5 and 0.02 respectively, a cumulative Gaussian function was fitted to each participant's data using a maximum likelihood criterion. From the fitted PF, the CFF threshold was derived as the flicker frequency at which the response accuracy would be 79% (data from one example participant illustrates the procedure in Figure 3.4).

One participant was excluded because a PF could not be fitted to their data. A goodness-of-fit test was performed for the rest of the participants to measure how well the fitted PF accounted for each participant's data. Six out of 37 participants had a goodness-of-fit p-value smaller than 0.05, indicating poor fit (Prins & Kingdom, 2018), but the CFF thresholds of these six participants were still retained in subsequent analyses. Because these participants had low numbers of corrupted trials (fewer than 5% in four participants, fewer than 10% in the other two participants), and after removing staircase runs most affected by corrupted trials using criteria described in Appendix 2, each participant had at least two staircase runs minimally influenced by corrupted trials. CFF thresholds computed from reversals in those staircase runs were highly correlated with the CFF estimates derived from those participants' PFs (see Appendix 2). This high correlation suggested that the PF-derived CFF estimates adequately reflected those participants' temporal resolution despite the low p-values in the goodness-of-fit test. Thus, the six participants were not excluded.

While the approach of fitting PFs to estimate CFF thresholds was adopted primarily to mitigate corrupted data, it has been shown in a previous simulation study that, compared to computing thresholds as averaged reversals, fitting PFs to staircase data resulted in threshold estimates closer to the veridical threshold (C. Manning et al., 2018). Furthermore, both previous studies (e.g., C. Manning et al., 2018) and the current study (see Appendix 2) showed that averaging staircase reversals and fitting PFs to the staircase data yielded highly correlated threshold estimates.

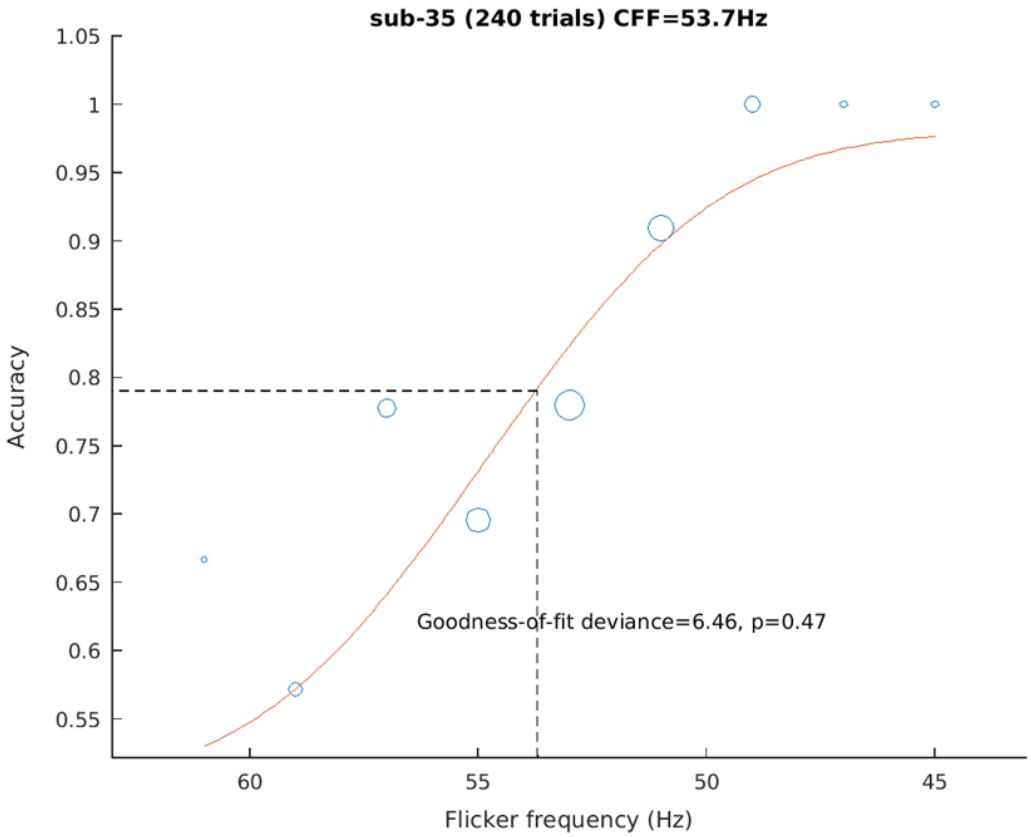

Figure 3.4: **An example participant's response accuracy at various flicker frequencies.**
The size of each data point reflects the number of trials carried out at this flicker frequency. The orange curve illustrates the psychometric function (PF) fitted to the data. Black dotted lines indicate the flicker frequency where the response accuracy is 79%. This frequency is used as the index of this participant's CFF threshold.

3.2.4 Visual gamma oscillations

Stimulus

Visual gamma oscillations were induced using a stationary vertical grating shown to yield robust visual gamma (Muthukumaraswamy & Singh, 2013) and recorded using MEG. The apparatus set-up was identical to that in the CFF tasks. Following the methods of the Muthukumaraswamy and Singh (2013) study, the stationary black-and-white square-wave vertical grating was eight-by-eight degrees in size and had a spatial frequency of three cycles per degree. The grating was centrally placed on a mid-grey background with a red fixation dot 0.2-degrees in size at the centre (see Figure 3.5).

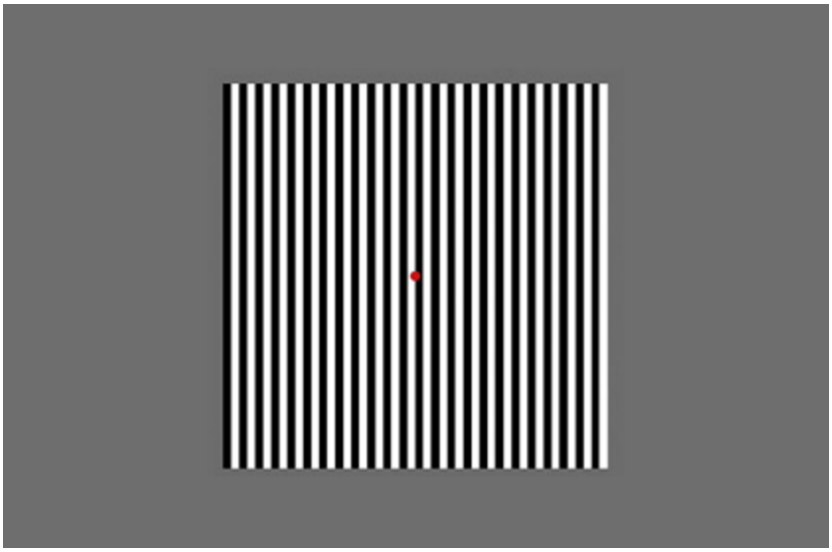

Figure 3.5: **An example grating stimulus.**

Procedure

As illustrated in Figure 3.6, each trial started with a fixation period of 1.5 s during which only the red fixation dot was present on the mid-grey background. Then the grating was presented for a jittered duration of 1.2-1.5 s while the fixation dot remained on the screen. Participants were instructed to fixate on the central red dot throughout the trial and to press a button as fast as possible at the offset of the grating (to maintain the participants' attention). The trial was repeated 100 times.

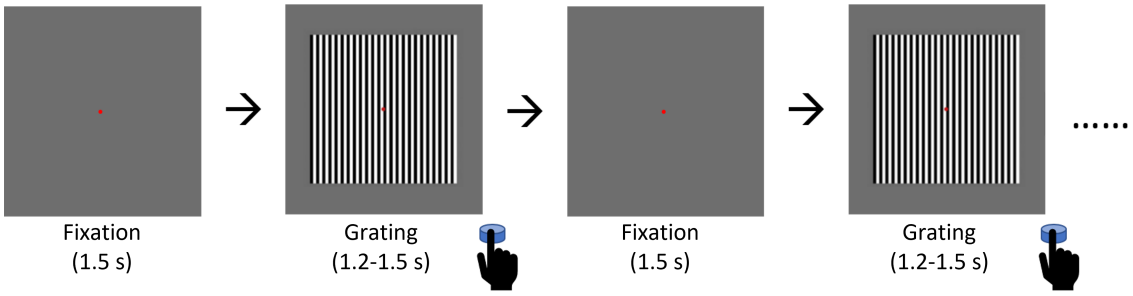

Figure 3.6: **Trial events in the visual gamma task.**
Each trial contained a fixation period and a grating presentation period. Participants were instructed to press a button as fast as possible after the offset of each grating.

MEG data acquisition and analysis

Neural oscillations during the task were recorded in a magnetically shielded room (MSR) with whole-head MEG using a 275-channel CTF axial gradiometer system sampled at 1200 Hz. Two of the sensors were turned off due to excessive sensor noise. An additional

29 reference channels were recorded for noise cancellation purposes. Three electromagnetic coils were placed at fiducial locations at nasion, left and right pre-auricular. The fiducial positions and the participant's head shape were recorded using a Polhemus Digitizer (Polhemus, Colchester, VT, USA) at the beginning of the scanning session. To localise the sources of the MEG signals, each participant's MEG data were co-registered with a whole-head T1-weighted anatomical MRI scan with 1 mm isotropic voxel resolution, obtained using a Fast Spoiled Gradient-Recalled-Echo (FSPGR) pulse sequence on a 3T MRI scanner (General Electric). For 14 participants, an anatomical MRI scan was not obtained due to practical restrictions during the COVID-19 pandemic. For these participants, a surrogate MRI scan closely matching the participant's head shape (as measured by the Polhemus Digitizer) was selected from a pool of 177 scans from existing MRIs on the CUBRIC database (Holliday et al., 2003).

The MEG data were first epoched from 1.5 s before the grating onset to 1.5 s after the grating onset in each trial. Visual inspection was carried out to exclude trials with muscular or head movement artefacts using the Data Editor software (CTF MEG, Canada). The data were then processed and analysed using the Fieldtrip toolbox (Oostenveld et al., 2011) in Matlab (version R2015a). The time-series data were band-pass filtered between 30-80 Hz, and the source of gamma oscillations was localised using linearly constrained minimum variance (LCMV) beamformer global covariance matrix. By contrasting the baseline period with the stimulus period containing sustained gamma oscillations (0.3-1.2 s after stimulus onset), a peak voxel in the visual cortex showing the greatest percentage increase in gamma power (between 30-80 Hz) from the baseline was identified as the localised source of the participant's visual gamma oscillations. A virtual sensor was then reconstructed at the source of the peak gamma activities. The time-series data of the virtual sensor was computed by multiplying the sensor-space data with the spatial-filter weights obtained from the beamformer analysis.

Each participant's peak amplitude and frequency of gamma oscillations were computed from the virtual sensor data in two ways. Firstly, spectral estimation was carried out using multitaper Fast Fourier Transform (FFT) for the baseline and stimulus periods respectively, using ± 2 Hz smoothing in steps of 0.5 Hz. The response power spectrum was computed as the percentage change from the baseline, and the gamma oscillation frequency was computed from the power spectrum as the centre of mass (total frequency weighted by amplitude) in the gamma range (30-80 Hz). The second estimate of peak gamma frequency was derived from the results of time-frequency analyses using the Hilbert transform with a bandwidth of 8 Hz and steps of 0.5 Hz (Swettenham et al., 2009). In the time-frequency representation (TFR) yielded from the time-frequency analysis, the frequency at which the greatest response power in the gamma range (30-80 Hz) occurred was regarded as the peak gamma frequency.

3.3 Results

3.3.1 Temporal response tuning profile and CFF

Correlation analyses were conducted to assess the relationship between the perceptual threshold for flicker and three features of the temporal response tuning profile, namely, the peak response frequency, the upper limit of chirp-evoked response, and the temporal tuning function across frequencies.

To explore whether an individual's CFF threshold was associated with their preferred response frequency to periodic visual stimuli, the frequency of the highest response power was identified from the temporal response tuning function at each harmonic. Since Spearman's correlations can be considerably skewed by outliers in a relatively small sample like in the current study, analyses were carried out using Shepherd's pi correlation which is robust to outliers (Schwarzkopf et al., 2012). This method identifies outlier observations by computing the Mahalanobis distance between each observation and the bivariate mean of all observations over 10,000 bootstrapping iterations. Observations with an average bootstrapping Mahalanobis distance of 6 or greater were regarded as outliers and excluded from the subsequent Spearman's correlation analysis (all correlation results reported in this Chapter were Spearman's correlations unless specified otherwise). There were no significant relationships between the CFF threshold and the peak response frequencies for the fundamental or any harmonic (Shepherd's pi correlation with 10,000 bootstrapping iterations; $p > .45$, figures in Appendix 3). This finding suggests that the perceptual threshold for flicker is unrelated to the temporal frequency evoking the strongest neuronal response.

Another feature of the temporal response tuning profile is the frequency above which chirp-evoked responses diminish to low response power (as defined in Section 3.2.2). A positive relationship was found between this upper limit of the chirp-evoked fundamental response and the CFF threshold, $r(33) = 0.44, p = .02$ without correction for multiple testing (as seen in Figure 3.7). This relationship was not observed between the CFF and the upper limits of harmonic responses (figures in Appendix 4).

To explore whether the CFF threshold was more relevant to particular parts of the temporal response tuning function, correlation analyses were conducted between the CFF threshold and the power of chirp-evoked responses at each frequency in the response tuning function. Spearman's correlation coefficients were computed, as the data were not normally distributed. After correcting for multiple testing using omnibus randomised testing with 1,000 permutations, the CFF threshold positively correlated with chirp-evoked fundamental responses at 57.4-57.7 Hz (see Figure 3.8A), and negatively correlated with third-harmonic responses at 158.8-159.5 Hz (see Figure 3.8B). The lat-

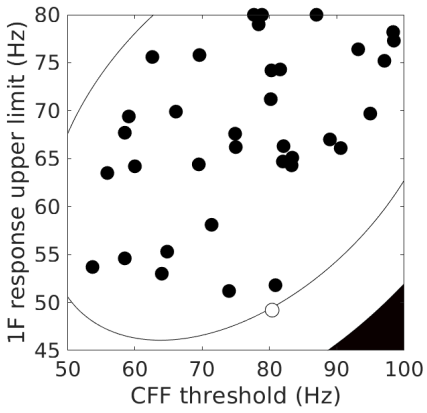

Figure 3.7: **Relationship between the CFF threshold and the upper limit of chirp-evoked fundamental response.**
Scatter plots, with contour plots of the Mahalanobis lines, illustrating the relationship between the CFF threshold and the frequency above which the fundamental chirp-evoked response diminishes to below 15% of the peak response. The contour lines and colours indicate ranges of the average bootstrapping Mahalanobis distance between each observation and the bivariate mean of all observations. The open circle indicates an outlier observation excluded from the correlation analysis due to an average bootstrapping Mahalanobis distance of 6 or greater.

ter correlation at high frequencies in the third harmonic response is not meaningful, because almost all participants ceased to have third harmonic responses beyond around 130 Hz (as seen in Figure 2.5D and Figure 2.7C in Chapter 2).

Since the CFF threshold was related to both the VSSR upper limit and the response power at around 57 Hz, a supplementary analysis assessed the relationship between the VSSR upper limit and the response power at each frequency in the fundamental response tuning function. Significant positive correlations were found between the upper limit of VSSR and the VSSR power at 45-74 Hz (see Appendix 5).

Given the CFF was associated with the upper limit of VSSR but not its peak response frequency, a supplementary analysis was conducted to assess the relationship between the upper limit and peak response frequency in the VSSR tuning function. As seen in Appendix 6, Shepherd's pi correlations found no relationship between the peak response frequency and the upper limit of response in the first four harmonics. Note, however, that a significant positive correlation was observed at the fifth, sixth and seventh harmonic.

Overall, the temporal response tuning profile was related to the CFF threshold in two ways. The CFF threshold was positively correlated with the upper limit of the chirp-evoked fundamental responses and with the power of fundamental responses at around 57 Hz. These latter two measures were also strongly related. No relationship was observed between the CFF threshold and the peak frequency in the temporal

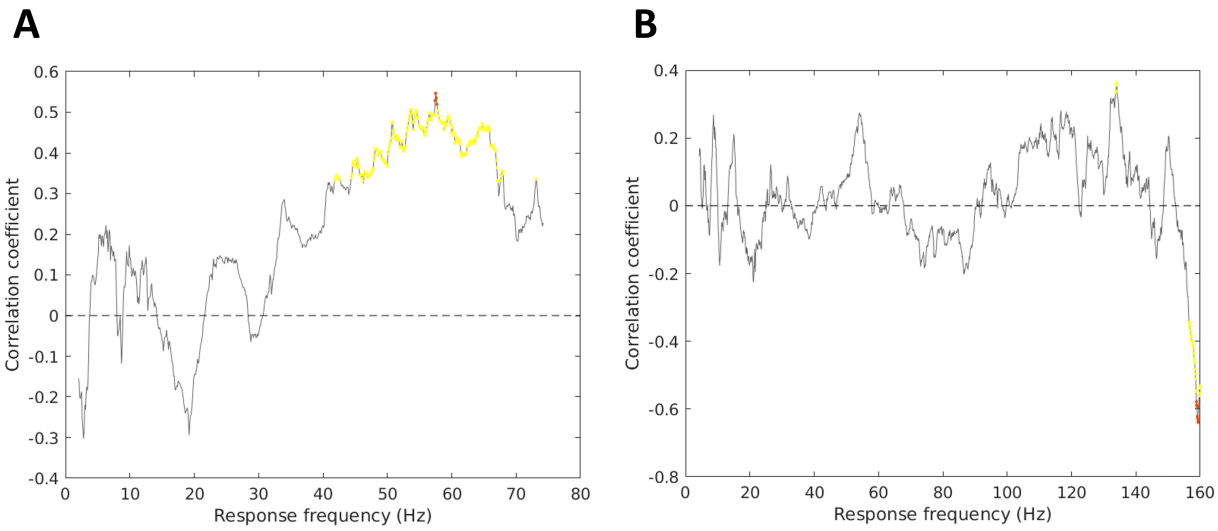

Figure 3.8: **Correlation between the CFF threshold and chirp-evoked response tuning functions.**
Spearman's correlation coefficients between the CFF threshold and chirp-evoked response tuning functions at the fundamental (A) and third harmonic (B). Yellow dots mark correlations with $p < .05$ before correction for multiple testing. Orange dots mark significant correlations after omnibus correction.

response tuning function. The peak temporal response frequency was unrelated to the upper limit of the VSSR at the fundamental and low-order harmonics, but a strong relationship was found at the fifth to seventh harmonics.

3.3.2 Temporal response tuning profile and visual gamma

Using Shepherd's pi correlation with 10,000 bootstrapping iterations, no significant relationships were found between the peak gamma frequency estimated by either method (deriving the peak gamma frequency from the FFT power spectrum or from the Hilbert transform TFR) and the peak visual chirp response at the fundamental (shown in Figure 3.9) or any other harmonic (see Appendix 7), $p > .25$ for all correlations.

The relationship between the peak gamma frequency and the upper limit of chirp-evoked responses (defined as the frequency at which the VSSR power decreased to 15% of the maximal response) was also assessed. As seen in Figure 3.10, Shepherd's pi correlation analyses found no significant relationship between the peak gamma frequency estimated by either method and the VSSR upper limit at any harmonic ($p > .17$ in all correlations, figures for harmonic components can be found in Appendix 8).

Finally, an exploratory analysis assessed whether the peak gamma frequency was related to the chirp-evoked response power at any particular frequency by analysing the correlations between the peak gamma frequency and the chirp-evoked response at each point in the temporal response tuning function. Results of Spearman's correlation

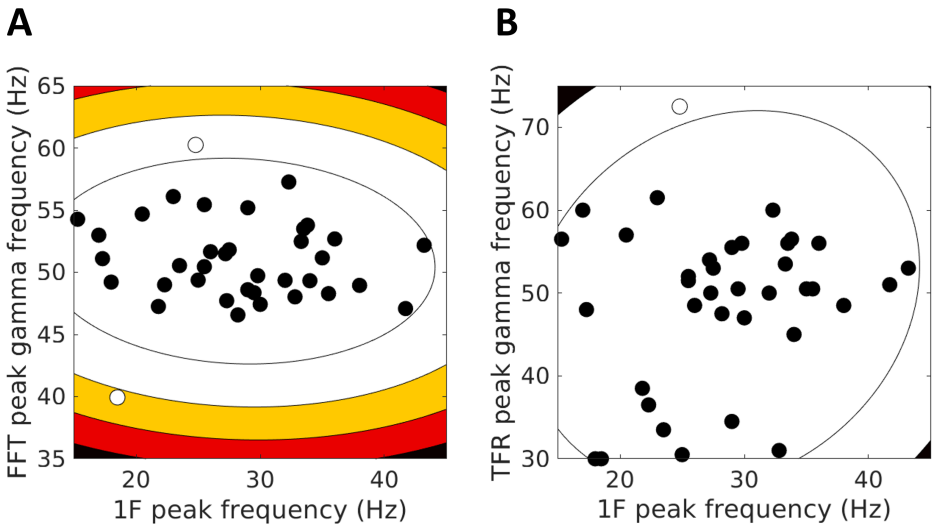

Figure 3.9: **Relationship between peak gamma frequency and the peak frequency of chirp-evoked fundamental responses.**
Scatter plots with contour plots of the Mahalanobis lines illustrating the relationship between the two estimates of peak gamma frequency and the peak fundamental response frequency in the visual chirp task. The contour lines and colours indicate ranges of the average bootstrapping Mahalanobis distance between each observation and the bivariate mean of all observations. Open circles indicate outlier observations excluded from the correlation analysis due to an average bootstrapping Mahalanobis distance of 6 or greater. **(A)** The peak frequency of chirp-evoked fundamental response was not correlated with the peak gamma frequency derived from the FFT power spectra, $r(33) = -0.16, p = .73$. **(B)** The peak frequency of chirp-evoked fundamental response was not correlated with the peak gamma frequency derived from time-frequency analysis TFRs, $r(34) = 0.13, p = .90$.

analyses were corrected for multiple testing using omnibus randomised testing with 1,000 permutations. No correlations were significant after the correction of multiple testing.

Overall, individuals' temporal response tuning profiles were unrelated to the frequency of grating-induced gamma oscillations.

3.4 Discussion

In order to explore the functional implications of the temporal response tuning profile, the current study assessed the individual differences in the VSSR tuning profile in relation to two other intrinsic properties of an individual's visual system, namely, the temporal resolution indexed by the CFF threshold and the peak frequency of grating-induced gamma rhythms. It was found that spectral features of the temporal response tuning function associate with the individual's perceptual threshold for flicker, but were

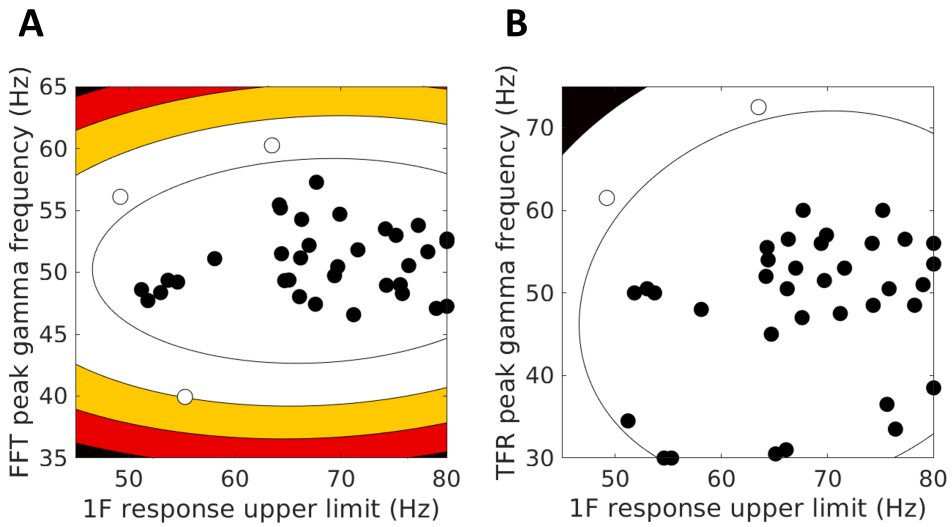

Figure 3.10: **Relationship between peak gamma frequency and the upper limit of chirp-evoked fundamental responses.**
Scatter plots with contour plots of the Mahalanobis lines illustrating the relationship between the two estimates of peak gamma frequency and the upper limit of fundamental response in the visual chirp task. The contour lines and colours indicate ranges of the average bootstrapping Mahalanobis distance between each observation and the bivariate mean of all observations. Open circles indicate outlier observations excluded from the correlation analysis due to an average bootstrapping Mahalanobis distance of 6 or greater. **(A)** The upper limit of chirp-evoked fundamental response was not correlated with the peak gamma frequency derived from the FFT power spectra, $r(32) = 0.07, p = 1.00$. **(B)** The upper limit of chirp-evoked fundamental response was not correlated with the peak gamma frequency derived from time-frequency analysis TFRs, $r(33) = 0.28, p = .21$.

unrelated to grating-induced gamma oscillations.

3.4.1 Temporal response tuning profile and CFF

As predicted, the CFF threshold was found to be positively related to the upper limit of VSSR. It indicated that the temporal limit of the visual system's neural responsiveness contributes to the determination of the temporal resolution of perception. This finding contrasts with Herbst et al. (2013)'s results that suggested no such relationship. One possible explanation for the contrasting findings of the two studies is the differences in task design. As described in the Introduction of this chapter, Herbst et al. (2013) indexed the upper limit of the VSSR as the highest stimulation frequency that evoked a significant response. However, only 10 stimulation frequencies were tested over the large range of 7.7-165.7 Hz. Thus the possible values of the VSSR upper limit were likely too sparsely sampled to capture the individual variability adequately. In contrast, the current study quantified the upper limit of VSSR using a cut-off threshold on a finely-

sampled temporal tuning function with a frequency resolution of 0.1 Hz. This allowed a much more precise estimate than the method used in Herbst et al. (2013)'s study, enabling even small individual differences to be captured. Moreover, the CFF threshold was also measured differently in my study and in the previous study. Compared to the criterion-dependent yes/no task used in the previous study, the criterion-free 2IFC paradigm I used is less prone to response biases. Overall, it is possible that Herbst et al. (2013)'s methods of measuring the VSSR upper limit and the CFF were not sensitive enough and/or biased, thus the relationship between the two was not observed.

The relationship between the VSSR upper limit and the CFF observed in the current study was consistent with the correlation profile found between CFF and the temporal tuning function (Figure 3.8A). Since participants' VSSR power generally decreased throughout the range of 45 to 70 Hz, the response power at a given frequency in this range could reflect how much the VSSR has diminished in a participant. In other words, the variability in the response power at 45-70 Hz conveys similar information as the variability in participants' VSSR upper limits, as confirmed by the supplementary analysis showing high correlations between the response power in this range and the upper limit of VSSR. Therefore, high correlation coefficients between the CFF and responses in this frequency range (indicated by the yellow section in Figure 3.8A) are consistent with the positive relationship between the CFF and the VSSR upper limit. However, only the responses in the middle of this range at around 57 Hz reached significance in their correlation with the CFF. This is likely because, at frequencies lower than 57 Hz, most participants had strong responses; as a result, with many data points clustered at high VSSR powers, there was not sufficient variability in the response power to form a linear relationship with the participants' CFF. Oppositely, at frequencies much higher than 57 Hz, many participants' VSSR has diminished too much thus clustered at the low end of the response power scale, not providing sufficient variability to form a correlation with the CFF threshold. Whereas at around 57 Hz, there was a sweet spot where the variability across participants' response power was maximal and most closely matched the CFF.

Overall, the correlation analyses described above demonstrated that higher perceptual thresholds for flicker were associated with the presence of relatively high power of the VSSR response at higher frequencies. This supports the notion that VSSR upper limit is a factor determining the limits of the temporal resolution of perception. In other words, for a periodic stimulus to be consciously perceived, neural activity in visual cortex needs to represent frequencies at least as high as the stimulus, which is measured here in the form of VSSR. Of course, the presence of enough power at a VSSR frequency at or above the stimulus frequency alone may not be sufficient for individuated perception of the flicker, but it provides a necessary condition. Other

factors that might also contribute to conscious awareness of individuated flickers might be connections between the visual cortex and other cortical regions such as the frontal cortex (Crick & Koch, 1995; Y. Jiang et al., 2007; Lamme, 2001). It is also important to keep in mind that the current study is correlational and future research is needed to establish that the relationships I found are based on a causal link.

Another spectral feature of the VSSR tuning profile assessed in relation to the CFF was the peak response frequency, also known as the resonance or preferred frequency of the visual system. It was found that the peak response frequency of a visual system was not related to its temporal resolution as indexed by the CFF threshold. The findings that the CFF was associated with the upper limit of VSSR but not its peak response frequency could indicate that these two characteristics of the temporal response profile are underpinned by different mechanisms. This notion is supported by the supplementary analysis showing no correlation between the peak response frequency and the upper limit of response in the first four harmonics but a strong positive correlation at the fifth to seventh harmonics. One possible interpretation of these findings is that the tuning functions of lower-order harmonics are underpinned by multiple interacting mechanisms, and different spectral features could carry different functional implications. For instance, the mechanism underlying the upper limit of the VSSR is associated with the temporal resolution of perception, but the function of the mechanisms underpinning the peak response frequency is still unclear. Given that the variability of different spectral features was more congruent at higher-order harmonics, this result might suggest that higher-order harmonics of VSSR are more likely underpinned by a single mechanism. This is consistent with the notion that high-order harmonics may be an artefact of nonlinear neuronal processing across the visual system and are unlikely to play a functional role in visual processing as do the fundamental and second harmonic of VSSR (Burns et al., 1992; Labecki et al., 2016; Norcia et al., 2015).

3.4.2 Temporal response tuning profile and visual gamma

Correlation analyses between individuals' peak gamma frequency and several measures of the spectral features of their VSSR temporal tuning profile showed that induced visual gamma and evoked VSSR were unrelated. This dissociation between the individual variability in visual gamma and VSSR is consistent with computational models indicating distinct neuronal mechanisms for induced visual gamma and evoked VSSR. Modelling and empirical studies have suggested that the generation of the two types of oscillations involves neuronal networks of different scales. While the peak gamma frequency is determined by the balance of excitation and inhibition of coupled neuronal populations within the visual cortex (Börgers & Kopell, 2003; Shaw et al., 2017), VSSR

properties are related to structural and functional connectivity of a large-scale brain network involving the visual cortex and other brain regions (Roberts & Robinson, 2012; Zhang et al., 2021). The dissociation between the neuronal mechanisms underpinning the two phenomena likely led to the dissociated spectral features of an individual's visual gamma and temporal response tuning function.

However, unrelated spectral properties do not necessarily indicate a lack of interaction between the two types of oscillations. Zhigalov et al. (2021) observed that broadband visual flickers led to predominant neural responses in the gamma band (a gamma echo), and this gamma echo was successfully modelled by the PING model which is previously known to generate induced visual gamma oscillations. This suggests that the PING circuit underlying induced visual gamma might also be driven in a resonant manner by visual flickers. In addition, both induced visual gamma and VSSR have been shown to be involved in the feedforward processing of visual information (e.g., Michalareas et al., 2016; Norcia et al., 2015), it is possible that the two neural phenomena have functional interactions in the bottom-up visual processing despite being originated from different mechanisms. The current finding of no relationship between the spectral features of the two types of oscillations indicates that it is still unclear whether or how visual gamma and VSSR might interact or influence each other.

Notably, in the current study, the peak visual gamma frequency was derived from source-localised virtual sensor data, whereas the temporal response tuning profile was derived from MEG data averaged across all occipital channels in the sensor-space. This might have contributed to the lack of relationship between spectral features of visual gamma and VSSR. Because stimuli of different frequencies have been found to evoke the strongest VSSR in different cortical regions (Chai et al., 2019; Srinivasan et al., 2006), this suggests that different regions within the visual cortex would have different temporal response tuning functions. As a result, the spectral properties of visual gamma oscillations may be more likely to be related to the properties of the temporal response tuning function derived from the same virtual sensor as the visual gamma, compared to the tuning function averaged across all occipital channels. Further analyses could compute the VSSR profile from source-localised data and test this possibility.

Moreover, the stimuli driving visual gamma and VSSR in the current study were substantially different, with gamma oscillations induced by a stationary grating and VSSR evoked by an unstructured flicker. The considerably different stimuli could have driven different visual processes that are not functionally related. In particular, visual gamma induced by a stationary and sustained stimulus can have different properties, such as peak frequency, from the gamma rhythms induced by a dynamic stimulus (Muthukumaraswamy & Singh, 2013). Since VSSR only occurs in response to dynamic and periodic stimulation, if VSSR and gamma rhythms were interacting and cooper-

ating in the feedforward visual processing of such stimuli, the properties of the VSSR tuning function would be more likely to be related to the spectral properties of the gamma rhythms during dynamic periodic stimulation, rather than during stationary stimulation. Future research could test this notion by measuring visual gamma using stimuli more similar to those used to evoke VSSR.

It is also noteworthy that the current study only analysed the peak frequency of induced gamma oscillations. While this measure is often used in the literature as a functional correlate with various perceptual and cognitive functions, other spectral properties of induced gamma, such as the peak amplitude and the diminishing frequency, could also be assessed in relation to the VSSR tuning profile. For example, a positive relationship between the amplitude of induced gamma oscillations and the VSSR power in the gamma range could indicate that the neuronal mechanisms generating induced visual gamma are also involved in regulating evoked responses. Whereas a positive relationship between the highest frequency of visual gamma and the highest frequency of VSSR would suggest that common factors restrict the upper limits of visually induced gamma rhythms and the temporal responsiveness in the visual cortex. Moreover, other types of measures to characterise the VSSR response function besides the peak frequency and upper limit could also be explored. For example, an inspection of individuals' VSSR fundamental tuning functions (see Section 2.3.3 in Chapter 2) revealed that over a third of the participants had a secondary peak response in the gamma range of 40-70 Hz in addition to the most prominent response at around 30 Hz. The properties of the gamma peak in the temporal response tuning function can be extracted and assessed in relation to the induced visual gamma, for instance, whether the frequency of grating-induced gamma is related to the frequency of the largest peak within the gamma range in the VSSR tuning function. If such a relationship is found, it could imply that the neuronal mechanisms underlying induced gamma rhythms also play a role in the evoked responses of the same frequency range.

3.4.3 Conclusions

Having established the tuning function for VSSR power at different temporal frequencies, the individual variability in this temporal response tuning profile was assessed in relation to two other measures that reflect intrinsic properties of the visual system, namely, the CFF threshold and the peak frequency of visually-induced gamma oscillations. The CFF threshold was positively related to the upper limit of VSSR responsiveness and the VSSR power at around 57 Hz, suggesting that the temporal resolution of perception is associated with the presence of VSSR at high frequencies. This supports the notion that the neuronal representation of a stimulation frequency

in the visual cortex is a necessary condition for the individuated perception of periodic stimuli at this frequency. The VSSR tuning profile was found to be unrelated to the peak frequency of grating-induced visual gamma, consistent with previous literature indicating differential neuronal mechanisms underlying VSSR and visual gamma. While analyses in the current study revealed no evidence for an association between the temporal response tuning profile and the peak gamma frequency, further analyses can explore the relationships between more spectral features of the VSSR profile and the visual gamma response spectrum to investigate whether and how evoked and induced oscillations interact in feedforward visual processing.

Chapter 4

The relationship between visual gamma oscillations and the critical flicker fusion threshold

4.1 Introduction

As described in the Introduction of Chapter 3, visually induced gamma oscillations play a role in feedforward visual processing, and properties of the visual gamma, such as its frequency, bandwidth and amplitude, are highly consistent within-subjects and variable between-subjects. Recent computational models suggest that visual gamma is a window into the intrinsic synaptic properties of the microcircuitry in visual cortex. The Pyramidal INterneuron Gamma (PING) model indicates that visual gamma oscillations are generated via the interactions between synaptically connected excitatory superficial pyramidal cells and inhibitory interneurons within the visual cortex (Börgers & Kopell, 2003; Spaak et al., 2012; Xing et al., 2012), and the frequency of the gamma oscillations is determined by synaptic connection parameters of the cortical microcircuit (Shaw et al., 2017; Shaw et al., 2020). Consequently, the frequency of an individual's visual gamma represents the intrinsic resonant frequency in the early processing columns of the visual system (Lewis et al., 2021; Moca et al., 2014), indicating the speed of temporal processing in early visual cortex. This, in turn, could determine the visual system's ability to temporally resolve fast consecutive stimuli.

Following the notion of perceptual cycles (VanRullen, 2016), it has been proposed that fast neuronal oscillatory cycles provide a high number of opportunities for neural representations over a short period of time, thus enabling fast consecutive stimuli to be represented as discrete representations, allowing conscious awareness of each stimulus (Allen, 2019). As a result, the observer would perceive a fast train of stimuli as flick-

ering rather than a time-averaged static image. Therefore, it may be predicted that an individual's intrinsic frequency of visual gamma oscillations is associated with the temporal resolution of their visual system.

The temporal resolution of the visual system can be indexed by the critical flicker fusion (CFF) threshold (introduced in more details in Chapter 3). While it is known that the CFF threshold can vary between and within individuals depending on stimulus attributes (Mankowska et al., 2021) and a number of observer-related factors such as age (Misiak, 1951), health condition (Sharma et al., 2007), and alertness and cortical arousal (Mankowska et al., 2021; Parrott, 1982), the exact mechanism underpinning the perceptual threshold for flickers remains poorly understood (Kahlbrock et al., 2012).

Although the CFF threshold has been used and studied for over a century (Brenton et al., 1989) and the visual gamma oscillations in humans have also been a focus of research for more than 20 years (Han et al., 2021), to my knowledge, so far only one published study has explored the relationship between the CFF threshold and the peak visual gamma frequency. Kahlbrock et al. (2012) measured the CFF threshold and recorded the visual gamma activity during an attention task using magnetoencephalography (MEG) in a sample of 20 patients with liver cirrhosis and 5 healthy controls. Twelve of the patients manifested hepatic encephalopathy (HE), a neuropsychiatric syndrome resulting from liver dysfunction (Häussinger et al., 2022). A significant positive correlation was found between the CFF threshold and the peak frequency of attention-related visual gamma in the pooled sample of patients and controls. Since the CFF threshold is known as an index of the severity of HE (Butz et al., 2013; Kircheis et al., 2002), Kahlbrock et al. (2012) interpreted their result of correlated CFF threshold and peak gamma frequency as an association between HE severity and attention-related gamma oscillations.

While this finding provides some initial support for the notion that visual gamma might determine the temporal limits of visual perception, conclusions that can be drawn from this mixture of clinical and healthy samples are limited. The first aim of the current study is therefore to test whether a relationship between the CFF threshold and peak visual gamma frequency can be observed in a healthy sample of participants. The second aim of the study is to gain a more mechanistic understanding of this potential relationship by computationally modelling the microcircuitry that generates visual gamma oscillations, and assess the relationship between synaptic properties that determine the peak visual gamma frequency and the temporal resolution of the visual system.

Visual gamma activity can be modelled using Dynamic Causal Modelling for steady-state responses (DCM-SSR) (Shaw et al., 2017) which is a neurophysiologically-informed approach that models the neuronal populations and connectivity underlying the gener-

ation of gamma oscillations in the primary visual cortex. It allows insights into synaptic properties of the V1 microcircuitry, such as the synaptic connectivity parameters and time constants of specific neuronal populations. Previous DCM modelling and pharmacological intervention have shown that three synaptic properties in the simulated microcircuitry determine the peak visual gamma frequency (Shaw et al., 2017). In particular, the peak gamma frequency is positively associated with the gain and the synaptic delay time-constant of superficial pyramidal cells in V1 macro-columns, and negatively related to the synaptic delay time-constant of inhibitory interneurons in the same macro-columns. By relating the model parameters indexing these mechanistic features of the visual cortex to the CFF threshold, the current study assesses if any aspect of the microcircuitry underlying visual gamma explains the temporal limits of our perception.

In summary, this study tests the notion that visual gamma oscillations may determine the temporal limit of visual perception. It is done by first assessing the relationship between healthy observers' visual temporal resolution and their peak frequency of visually induced gamma oscillations. This relationship is then explored mechanistically by assessing the link between the CFF threshold and the computationally modelled synaptic properties of the microcircuitry underlying the generation of visual gamma oscillations.

4.2 Methods

4.2.1 Participants

Data from the 37 participants who completed the tasks described in Chapter 3 were analysed in the current study.

4.2.2 Stimuli and procedure

Details of the tasks measuring the CFF threshold and grating-induced visual gamma oscillations can be found in Section 3.2 of Chapter 3. The CFF threshold was derived from psychometric functions fitted to data obtained in a 2-interval forced choice (2IFC) task. Participants' peak frequency of visual gamma oscillations was estimated in two ways, respectively from the Fast Fourier Transform (FFT) power spectrum and the Hilbert transform time-frequency representation (TFR) (see Section 3.2.4 for details).

4.2.3 Dynamic Causal Modelling

Dynamic Causal Modelling for steady-state responses (DCM-SSR) was carried out using a modified version of the SPM8 package (Moran et al., 2009). Details on the model structure and modelling procedure were described by Shaw et al. (2017). In summary, the model simulates a three-layer structure of V1 macro-columns by a variation of the canonical microcircuit (CMC), including four neuronal populations (superficial and deep excitatory pyramidal cells, excitatory stellate cells and inhibitory interneurons) and local synaptic connectivity between and within these cell populations (see Figure 4.1).

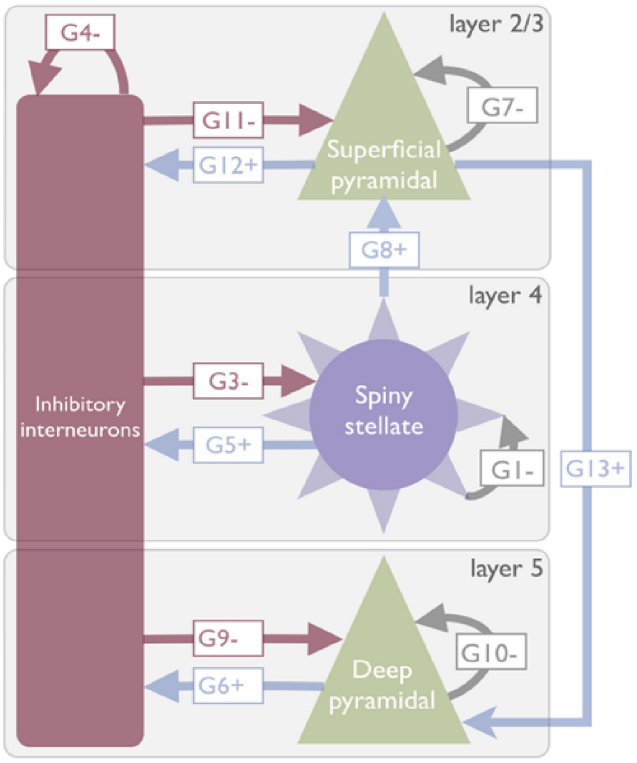

Parameter		Description	Prior π (σ)
G1	*i*	Spiny Stellate Population Gain	800 [1/8]
G3	*i*	Inhibitory Interneurons to Spiny Stellates	800 [1/8]
G4	*i*	Inhibitory Interneurons Population Gain	800 [1/8]
G5	*e*	Spiny Stellate to Inhibitory Interneuron	800 [1/8]
G6	*e*	Deep Pyramidal to Inhibitory Interneuron	400 [1/8]
G7	*i*	Superficial Pyramidal Population Gain	800 [1/8]
G8	*e*	Spiny Stellate to Superficial Pyramidal	800 [1/8]
G9	*i*	Inhibitory Interneuron to Deep Pyramidal	400 [1/8]
G10	*i*	Deep Pyramidal Population Gain	200 [1/8]
G11	*i*	Inhibitory Interneuron to Superficial Pyramidal	800 [1/8]
G12	*e*	Superficial Pyramidal to Inhibitory Interneuron	800 [1/8]
G13	*e*	Superficial Pyramidal to Depp Pyramidal	800 [1/8]
b		Noise Model: [Noise Power Exponent, Noise Amplitude, Alpha Amp, Alpha Frequency, Alpha Width]	[0 0 0.03, 10, 2]
T1		Time constant: SS	2 ms [1/8]
T2		Time constant: SP	2 ms [1/8]
T3		Time constant: II	10 ms [1/8]
T4		Time constant: DP	20 ms [1/8]
J		Contributing states [ss sp ii dp]	[20 80 0 20] % [0]
D		Intrinsic delay constant	1 ms [0]
R (set from P.S)		Slope of sigmoid function	2/3 [0]

Figure 4.1: **Illustration of the canonical microcircuit (CMC) used in the DCM procedure.**
The left panel illustrates the neuronal populations, excitatory and inhibitory connections between cell populations (blue and red arrows respectively), and self-inhibition within each cell population (grey arrows) in the three-layered CMC model. The right panel lists parameters that define the model and their respective prior values (π) and precision (σ). This figure is Fig. 2 of Shaw et al. (2017)'s study.

Through time differential equations, the CMC model generates a time course of membrane potentials and postsynaptic currents of the cell populations. This time-series output is then transferred to the frequency domain, and the frequency-domain model output can be compared with the frequency spectral density of participants' MEG virtual sensor data. Figure 4.2 illustrates a schematic of the analysis and mod-

elling procedure. Each participant's MEG virtual sensor data were transferred into the frequency domain via a standard Fourier approach using the smoothed periodogram. The spectral density was then "pre-whitened" to eliminate the effect of the strong power-law dominating the frequency spectra and reveal the presence of alpha, beta and gamma peaks (J. R. Manning et al., 2009). The pre-whitened spectral density was averaged across participants, and the CMC model was fitted to the mean spectrum using a standard Bayesian inference procedure. The values of model parameters from the best fit model were used as prior values in the subsequent fitting of the model to each participant's spectral density data.

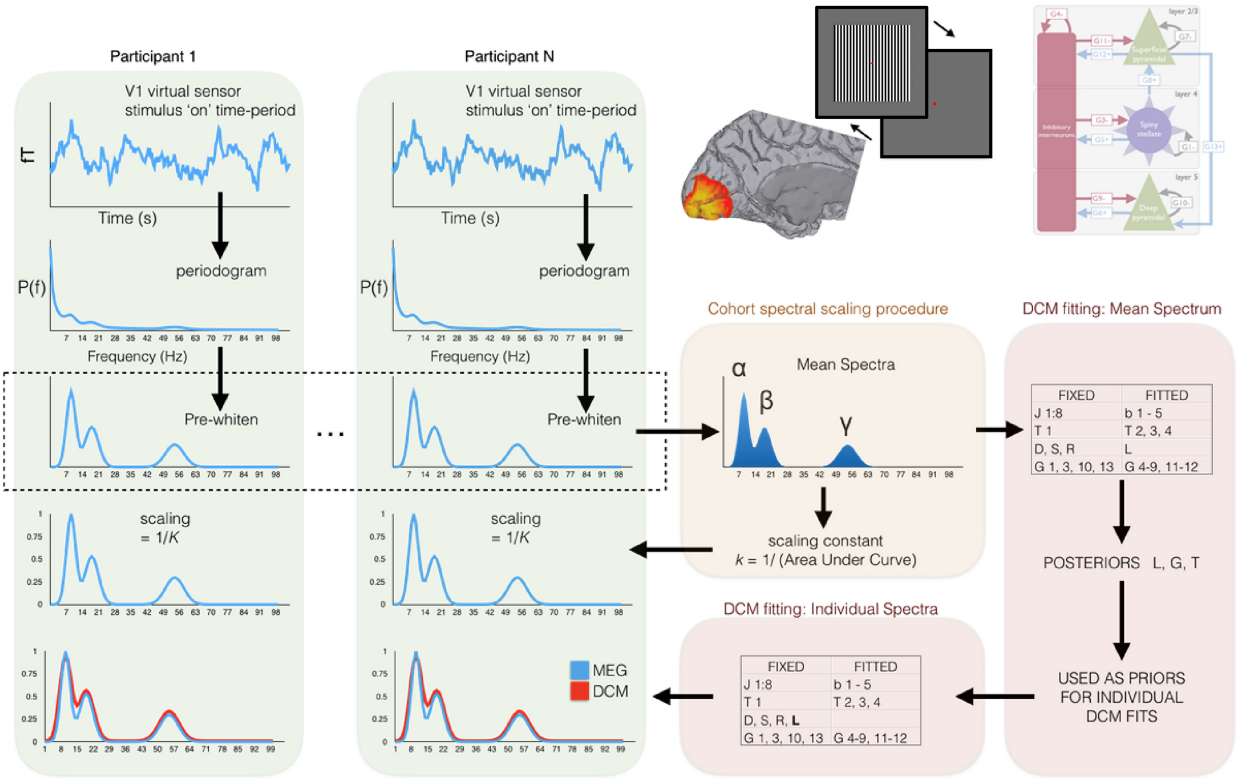

Figure 4.2: **A flowchart illustrating the DCM-SSR analysis and model fitting procedure.**
This figure is taken and adapted from Fig. 1 of Shaw et al. (2017)'s study.

Before fitting the DCM-SSR model to each individual participant's data set, the individual's virtual sensor spectral density was normalised in relation to the area-under-the-curve of the global mean spectrum. In the individual model fitting process, a number of model parameters (G1, G2, G3, G10, G13 and T1) were fixed to their prior means to reduce model complexity, because these parameters either had little or no effect on the fitted spectral density or severely impacted the model stability when not fixed (Shaw et al., 2017). The current CMC model can generate clear gamma and beta response peaks, but an alpha peak cannot be simultaneously generated by a single

source model without a more extensive neuronal network including thalamocortical 'loops' (Shaw et al., 2017). Therefore, the presence of the alpha response peak was explicitly modelled by adding a Gaussian function to the SPM8 noise function.

Three key DCM model parameters have been previously shown to determine the peak gamma frequency (Shaw et al., 2017). Specifically, the peak frequency of gamma oscillations was found to be positively correlated with the self-inhibition parameter controlling the gain of superficial pyramidal cells (G7) and the time constant of superficial pyramidal cells (T2), whereas the time constant of inhibitory interneuron (T3) was found to be negatively correlated with peak gamma frequency. Therefore, these three model parameters in the best fit model for each participant's MEG virtual sensor data were correlated with the participants' CFF threshold to explore any relationship between the synaptic properties related to the gamma frequency and the perceptual temporal resolution of the visual system.

4.3 Results

4.3.1 Relationship between peak gamma frequency and CFF threshold

To test whether there is a relationship between the temporal resolution of the visual system and the peak visual gamma frequency in a sample of healthy participants, correlation analyses were conducted between participants' CFF threshold and peak visual gamma frequency.

Each participant's peak gamma frequency was estimated by three methods - the centre of mass in the gamma range derived from the FFT power spectrum, the peak frequency derived from the maximum gamma response in the time-frequency analysis TFR, and the peak gamma frequency obtained from each participant's pre-whitened spectral density in the process of fitting the DCM model (the first two measures were described in section 3.2.4 on page 53, the third measure was described in section 4.2.3 on page 68). Participants' CFF thresholds were correlated with each of the three measures of peak gamma frequency. Shepherd's pi correlations (Schwarzkopf et al., 2012) were used to remove outliers before carrying out Spearman's correlation analysis (all correlation results reported in this Chapter were Spearman's correlations unless specified otherwise).

As shown in Figure 4.3, none of the three peak gamma frequency estimates significantly correlated with participants' CFF thresholds ($p \geq .90$ for all three correlations). In other words, no relationship was found between participants' peak gamma frequency and their temporal resolution.

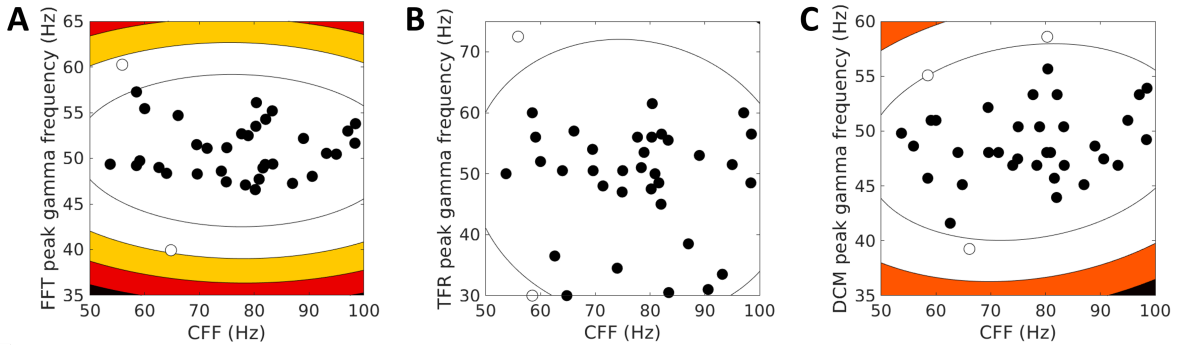

Figure 4.3: **Correlations between the CFF threshold and the peak gamma frequency.**
Scatter plots with contour plots of the Mahalanobis lines illustrating the relationship between the CFF threshold and the three estimates of peak gamma frequency. The contour lines and colours indicate ranges of the average bootstrapping Mahalanobis distance between each observation and the bivariate mean of all observations. Open circles indicated outlier observations excluded from the correlation analysis due to an average bootstrapping Mahalanobis distance of 6 or greater. **(A)** The CFF threshold was not correlated with the peak gamma frequency derived from the centre of mass in the FFT power spectra, $r(32) = 0.05, p = 1.00$. **(B)** The CFF threshold was not correlated with the peak gamma frequency derived from time-frequency analysis TFRs, $r(32) = -0.05, p = 1.00$. **(C)** The CFF threshold was not correlated with the peak gamma frequency derived from the pre-whitened spectral density (computed in the process of fitting the DCM model), $r(31) = 0.14, p = .90$.

4.3.2 Relationship between peak gamma frequency and DCM parameters

Before analysing the relationship between participants' temporal resolution and DCM parameters underpinning the peak visual gamma frequency, I first checked whether the three key model parameters demonstrated the expected relationships with the peak visual gamma frequency, as reported by Shaw et al. (2017).

Shepherd's pi correlation was used to analyse the relationship between the peak gamma frequency estimated from the pre-whitened spectral density of the virtual sensor signals and three key DCM model parameters, specifically, the self-inhibition parameter controlling the gain of superficial pyramidal cells (G7), the time constant of superficial pyramidal cells (T2), and the time constant of inhibitory interneuron (T3).

As seen in Figure 4.4, DCM parameters G7, T2 and T3 were all significantly related to the participants' peak gamma frequency. Specifically, the self-inhibition parameter controlling the gain of superficial pyramidal cells (G7) was positively correlated with the frequency of gamma oscillations, $r(32) = 0.63, p = 1.16 \times 10^{-4}$. The time constant of superficial pyramidal cells (T2) was also positively correlated with the peak gamma frequency, $r(31) = 0.46, p = .02$, whereas the time constant of inhibitory interneuron (T3)

was negatively correlated with peak gamma frequency, $r(30) = -0.78, p = 3.20 \times 10^{-7}$. These relationships closely match previous findings of Shaw et al. (2017), demonstrating that G7, T2 and T3 values reflect synaptic properties modulating the peak gamma frequency in our simulated visual cortex.

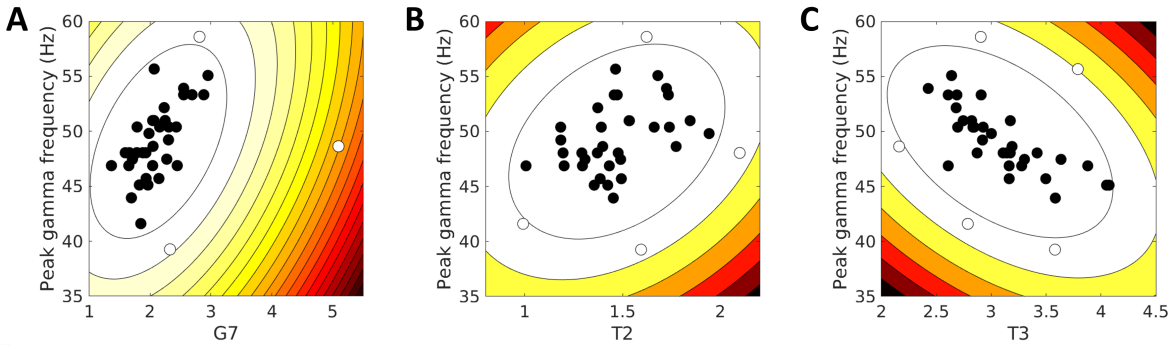

Figure 4.4: **Correlations between key DCM model parameters and the peak gamma frequency.**
Scatter plots with contour lines of the Mahalanobis distance illustrating the relationship between the peak gamma frequency estimated from the pre-whitened spectral density of virtual sensor signals and three key DCM model parameters. The contour lines and colours indicate ranges of the average bootstrapping Mahalanobis distance between each observation and the bivariate mean of all observations. Open circles indicated outlier observations excluded from the correlation analysis due to an average bootstrapping Mahalanobis distance of 6 or greater. The peak gamma frequency was positively correlated with G7, the self-inhibition parameter controlling the gain of the simulated superficial pyramidal cells **(A)**, and the time constant of the simulated superficial pyramidal cells, T2 **(B)**. The time constant of the simulated inhibitory interneuron, T3, was negatively correlated with the peak gamma frequency **(C)**.

4.3.3 Relationship between DCM parameters and CFF threshold

To assess whether the temporal resolution of the visual system is linked to properties of the synaptic microcircuitry underpinning the visual gamma frequency, Shepherd's pi correlation analyses were conducted to explore the relationship between the CFF threshold and the three DCM parameters shown by Shaw et al. (2017) and the current study to determine the peak gamma frequency (G7, T2 and T3).

As seen in Figure 4.5, none of those model parameters had any significant correlation with the CFF threshold ($p > .95$ for all three correlations). This suggested a lack of relationship between the temporal resolution of the visual system and the synaptic properties determining the peak visual gamma frequency.

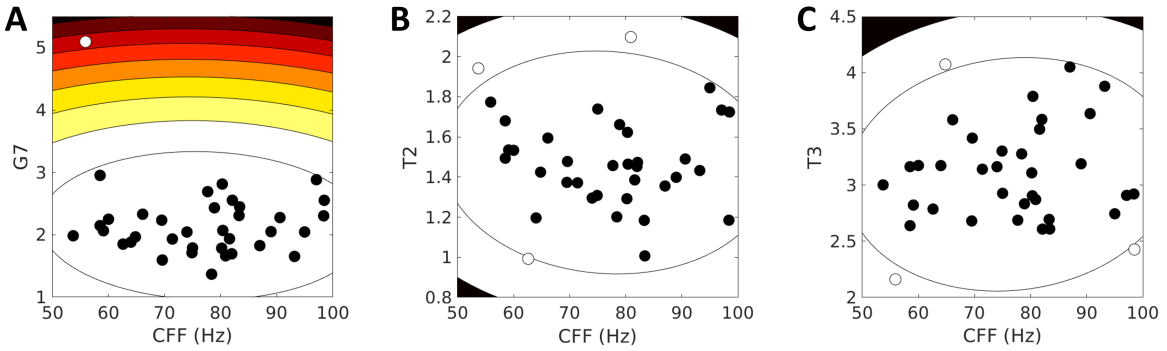

Figure 4.5: **Correlations between key DCM model parameters and the CFF threshold.**
Scatter plots with contour plots of the Mahalanobis lines illustrating the relationship between the CFF threshold and three key DCM model parameters. The contour lines and colours indicate ranges of the average bootstrapping Mahalanobis distance between each observation and the bivariate mean of all observations. Open circles indicated outlier observations excluded from the correlation analysis due to an average bootstrapping Mahalanobis distance of 6 or greater. **(A)** The self-inhibition parameter controlling the gain of the simulated superficial pyramidal cells (G7) was not correlated to CFF, $r(33) = 0.12, p = .97$. **(B)** The time constant of the simulated superficial pyramidal cells (T2) was not correlated to CFF, $r(31) = -0.12, p = 1.00$. **(C)** The time constant of the simulated inhibitory interneuron (T3) was not correlated to CFF,$r(31) = 0.11, p = 1.00$.

4.3.4 Exploratory correlation analyses

Correlation between CFF threshold and gamma response spectrum

Given that the CFF threshold was found to be unrelated to the peak frequency of gamma oscillations, exploratory analyses were conducted to assess if the CFF threshold related to any other features of the response spectrum during the viewing of a gamma-inducing grating. In each participant's time-frequency representation (TFR) yielded from the Hilbert transform, neural activities that occurred 300-1200 ms after the grating onset were averaged across time to produce a spectrum of response power at each frequency during grating viewing.

First, the upper limit of gamma oscillations was assessed in relation to the CFF threshold. If gamma oscillations facilitate the individuation of flickers, the highest stimulus frequency the gamma oscillations can accommodate would be the upper limit of the visual gamma. Thus the CFF threshold would be expected to be positively correlated with the upper limit of participants' visual gamma oscillations. From each participant's time-averaged response spectrum described earlier, the upper limit of gamma oscillations was defined as the frequency at which the response power decreased to 15% of the participant's peak gamma response. Shepherd's pi correlation analysis showed

no significant relationship between the CFF threshold and the upper limit of visual gamma oscillations, $r(33) = 0.004, p = 1.00$.

Second, participants' response power at each frequency was correlated with the CFF thresholds to determine if the responses at any particular frequencies were especially relevant to the perceptual temporal resolution. Since data were not normally distributed, Spearman's correlation coefficients were computed for each response frequency. After an omnibus correction for multiple testing using randomised testing with 10,000 permutations, the CFF threshold was not significantly correlated with responses at any frequency during grating viewing (see Figure 4.6).

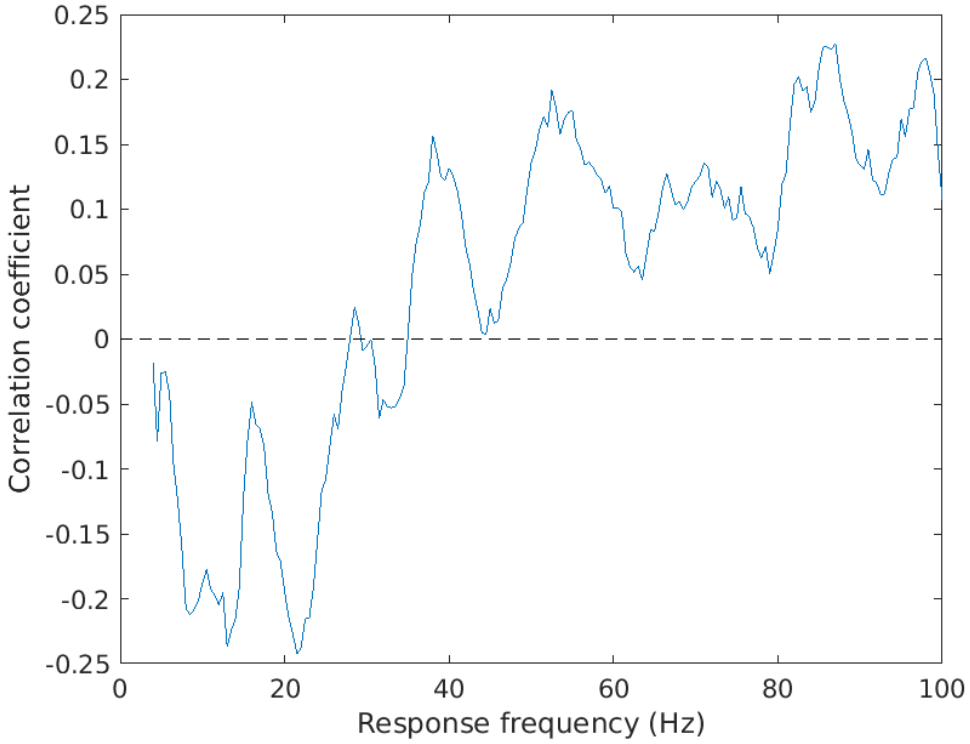

Figure 4.6: **Correlation coefficients between the CFF thresholds and the response power at each frequency during grating viewing.**
After omnibus correction for multiple testing, neural responses at none of the frequencies were significantly correlated with participants' CFF thresholds.

These exploratory analyses showed that the temporal resolution of the visual system could not be explained by the upper limit of the observer's visual gamma oscillations or the response power at any frequency during the viewing of a gamma-inducing grating.

Correlation between CFF threshold and all DCM parameters

While the CFF threshold was not related to the three DCM parameters known to determine the peak frequency of visual gamma oscillations, exploratory analyses were

conducted to assess if any other model parameters were linked to the temporal resolution of the visual system.

Therefore, exploratory correlation analyses were carried out between the CFF threshold and all the free model parameters in the DCM-SSR (G4, G5, G6, G7, G8, G9, G11, G12, T4, alpha peak amplitude, alpha peak frequency, Gaussian width of the alpha peak) and spectral features of the data estimated before model fitting (beta peak amplitude, beta peak frequency, gamma peak amplitude, the intercept and slope of the background power-law noise in the frequency spectral density). None of the model parameters or spectral features listed above had a correlation with the CFF threshold that survived any p-value correction for multiple comparisons. The temporal resolution of the visual system was found to be unrelated to all DCM parameters and spectral features during the viewing of gamma-inducing grating.

4.4 Discussion

The frequency of visually induced gamma oscillations reflects the intrinsic resonant frequency of V1 cortical microcircuit. In other words, it indicates the temporal processing speed of the early visual cortex, which may determine the limit of the visual system's ability to temporally resolve fast consecutive stimuli. Therefore, the current study assesses whether healthy observers' visual temporal resolution is explained by the peak frequency of their visual gamma and the synaptic properties of the computationally modelled cortical microcircuitry underlying visual gamma generation. No relationship was found between the peak visual gamma frequency and the CFF threshold reflecting the temporal resolution of visual perception. Neither was the CFF threshold related to any parameters of the DCM model indexing the synaptic properties of the V1 microcircuitry underlying visual gamma oscillations. Exploratory analyses also showed no association between the CFF threshold and any spectral feature of the grating-induced visual neural responses or any free parameters of the DCM model. These findings suggest that the temporal limit of visual perception was not determined by visually induced gamma oscillations or the V1 synaptic functions controlling the timing properties of gamma oscillations.

The CFF thresholds yielded from the current study ranged from 50 to 100 Hz, much higher than the CFF measures in most previous studies, typically between 30 to 50 Hz (e.g., Baumgarten et al., 2018; Eisen-Enosh et al., 2017; Kahlbrock et al., 2012). This was anticipated, as the CFF threshold is known to be modulated by various factors, including the age and health of the observers (Misiak, 1951; Sharma et al., 2007), the task and threshold criterion used to obtain the measure (Eisen-Enosh et al., 2017; Fernandez-alonso et al., 2019), as well as visual properties of the stimulus such as retinal

size, eccentricity, luminance, contrast and colour (Brown et al., 2018; Hartmann et al., 1979; Hecht & Verrijp, 1933; Liu et al., 2015). The flicker stimulus used in the current study is large, centrally positioned, high-luminance, full-contrast and achromatic; all are features known to yield higher CFF thresholds. In addition, participants of the current study are healthy and substantially younger (with a mean age of 28.19) than previous studies such as Kahlbrock et al. (2012) and Baumgarten et al. (2018), where the mean age of participants (many are patients) is around 60. The younger age and better health of our participants could have also contributed to the higher CFF thresholds than in other studies. Due to the high observer- and stimulus-dependent specificity of the CFF performance, the absolute values of CFF thresholds cannot be directly compared across studies.

When testing the relationship between the CFF threshold and the peak frequency of visual gamma oscillations, I used three different methods of estimating the peak gamma frequency but found no significant relationship between any of these measures and the CFF thresholds. This result contrasts with Kahlbrock et al. (2012)'s finding of a positive correlation between the CFF threshold and peak gamma frequency. The Kahlbrock et al. (2012) study differed from the current study in important ways: First, the current study measured participants' CFF threshold using an adaptive staircase procedure, which has been shown to be more robust in test-retest repeatability than the method of adjustment used by Kahlbrock et al. (2012) and many other studies of patient samples (Eisen-Enosh et al., 2017). Second, I derived the peak gamma frequency from neural activity during simple viewing of gratings with minimal cognitive demand, whereas visual gamma oscillations were recorded in Kahlbrock et al. (2012)'s study while participants were performing an attention task that involved gratings. This methodological choice is potentially problematic because the spectral characteristics of visually induced gamma oscillations can vary with the cognitive processes involved in the task. For example, attention, grouping and conscious awareness have been shown to modulate activities in different frequency components of gamma oscillations (Vidal et al., 2006; Wyart & Tallon-Baudry, 2008). Therefore, compared to attention-related gamma oscillations measured by Kahlbrock et al. (2012), visual gamma activities measured during simple viewing of stationary grating without any cognitive task can potentially better capture intrinsic properties of the visual system in perceptual processing with minimal interference from higher-level cognitive functions, and therefore more appropriate in assessing if gamma oscillations play any role in determining the temporal resolution of the visual system. Third, and most importantly, 20 out of the 25 participants in Kahlbrock et al. (2012)'s study were patients with liver cirrhosis, some manifesting hepatic encephalopathy (HE), while all participants in the current study had no history of neurological conditions. HE is a neuropsychiatric syndrome resulting

from liver dysfunction (Häussinger et al., 2022). A key pathomechanism of HE is the global slowing of oscillatory activity in the brain (Butz et al., 2013), and symptoms of HE consist of a wide range of neurological and cognitive impairments, including both attentional deficits and impairments in visual processing. The CFF threshold has been a commonly-used measure to index the severity of HE, even though the indicative role of CFF for HE is based solely on correlational findings without a mechanistic understanding of any causal relationship between HE pathology and the lowering of the CFF threshold (Butz et al., 2013).

The positive relationship between the CFF threshold and the peak frequency of attention-related gamma oscillations found in Kahlbrock et al. (2012)'s study may be the result of the attention task performed while recording gamma. The peak frequency of gamma oscillations during the attention task could have encoded attentional modulation rather than the intrinsic cortical properties of the visual system. Thus, its correlation with the CFF may have reflected the increased extent of attentional deficits with increased HE severity (indexed by the CFF), rather than the role of gamma oscillations in determining the temporal resolution of the visual system. An alternative interpretation of the positive relationship could be that the HE pathology of the global slowing of oscillatory activities led to both lowered visual gamma frequency and reduced temporal resolution. In other words, the relationship found was mediated by HE; the link between visual gamma and CFF in patients could be different from that in healthy individuals.

Investigation into this relationship in healthy individuals is needed. Since the exact physiological mechanism underlying the CFF is largely unclear (Kahlbrock et al., 2012), assessing whether the CFF is explained by visual gamma aids the understanding of how the temporal resolution of perception is determined. In contrast to the poorly understood neuronal mechanism of CFF, much progress has been made in gaining mechanistic insights into the generation of visual gamma with the help of recent computational modelling techniques (Shaw et al., 2017; Shaw et al., 2020). Due to the neurophysiologically-informed model structure and validation via pharmacological manipulations, the DCM-SSR model enables a highly specific understanding of the visual gamma generation at the level of cortical microcircuitry. Compared to phenomenological data features such as peak gamma frequency, the synaptic properties of the gamma-generating microcircuitry modelled by the DCM have the potential to better explain inter-individual variability and any relationship between visual gamma and CFF with high mechanistic specificity.

The current study on healthy individuals found the CFF to be unrelated to both the spectral properties of visual gamma and modelled synaptic properties of the gamma-generating cortical microcircuitry. This lack of association indicates that visual gamma

oscillations cannot explain the ability to temporally resolve visual stimuli. This may be interpreted in one of two ways.

First, the temporal resolution of visual stimuli may not be directly facilitated by the neuronal mechanism that generates visual gamma oscillations; the individuation of high-frequency visual stimuli may be underpinned by other neuronal processes. For example, it has been proposed that the conscious awareness of visual stimuli requires feedforward and feedback connections between V1 and other cortical areas, in addition to being processed in the visual cortex (Crick & Koch, 1995; Y. Jiang et al., 2007; Lamme, 2001). Moreover, the temporal resolution can also be affected by pre-cortical factors influencing the temporal processing efficiency, as the CFF threshold has been shown to be positively related to macular pigment density in the retina (Hammond & Wooten, 2005) and the conduction rate of neuronal axons (Namerow, 1971). Visual gamma may not be one of the factors determining the upper limit of perception.

Second, oscillations in the gamma band may indeed play a role in the temporal processing of stimuli and facilitate stimulus individuation, but such gamma activity would be expected to occur during the viewing of flickers, and it could be underpinned by a different neuronal mechanism to the gamma oscillations induced by a stationary grating. Even though the grating-induced gamma assessed in the current study reflects some intrinsic properties of the visual cortex, it may not be the properties functionally relevant to the temporal resolving of flickering stimuli. Further research could investigate the gamma activity during the viewing of high-frequency stimuli and whether it relates to the individual's temporal resolution.

In summary, in healthy individuals, the temporal resolution of the visual system was found to be unrelated to visual gamma oscillations induced by stationary grating. The temporal limit of visual perception is not determined by the cortical properties underlying grating-induced gamma oscillations.

Chapter 5

The early sensory processing of a feature is modulated by the feature's contribution to high-level object perception

5.1 Introduction

Visual perception arises through a combination of noisy sensory inputs and expectations based on the observer's prior knowledge and experience (de Lange et al., 2018; Teufel & Fletcher, 2020). The conventional model of visual processing indicates that early feature detectors in the primary visual cortex form representations of local low-level features, and these representations converge into more sophisticated representations of mid-level features and high-level object percepts (the process known as bottom-up processing) (Frisby & Stone, 2010). More recently, it has been recognised that high-level representations also exert top-down influences on early visual processing (e.g., Christensen et al., 2015; González-García & He, 2021; Teufel et al., 2018). The current study explores one specific hypothesis that may allow reconciliation of seemingly contradictory findings about the effects of top-down processing on early vision.

Effects of the dynamic interaction between high-level representations of global percepts and low-level representations of local features have been studied using various methodological approaches. While animal electrophysiology, neuroimaging and computational modelling provide insights into the effects of top-down modulation on the neural encoding across the cortical processing hierarchy (e.g., Gilbert & Li, 2013; González-García & He, 2021; Spratling, 2016), effects on visual behaviour are revealed by behavioural methods like psychophysics. Such behavioural studies have demonstrated

that an observer's perceptual sensitivity to low- and mid-level visual features can be modulated by high-level representations. However, interestingly, these studies did not agree on the direction of the modulation by high-level representations.

A number of studies have shown that high-level representations based on object knowledge can sharpen early feature detectors and lead to an enhancement in the perceptual sensitivity to local low-level features. For instance, the sensitivity to orientation and position in visually noisy stimuli was found to be higher when the images contained objects compared to when they lacked objects but contained fractal textures with an orientation structure of similar complexity (Christensen et al., 2019; Christensen et al., 2015). Similarly, high-level percepts have been shown to increase the perceptual sensitivity to the motion and temporal coherence of local elements (Tadin et al., 2002), the blurriness of letter strings (Lupyan, 2017), and the distance between facial features (Namdar et al., 2015). However, other studies found an opposite direction of modulation. For instance, Poljac et al. (2012) showed that the high-level percept of a walking human figure reduced conscious accessibility to local colour changes within the walker and led observers to perceive local colour changes to be slower when the walker percept was strong compared to when the walker percept was diminished. Similarly, Mamassian and Zannoli (2020) found that eliciting a high-level representation of an object, whether by physically connecting vertical lines, grouping them by colour or using cross-modal auditory cues, resulted in impaired precision and accuracy in binocular depth perception of vertical lines. Taken together, there is conflicting evidence on whether high-level representations enhance or suppress perceptual sensitivity in lower-level visual processing.

These seemingly contradictory findings may be reconciled by a moderating factor that determines the direction of the top-down modulation. This notion is inspired by Teufel et al. (2018)'s study which showed that the presence of top-down enhancement on local sensitivity was influenced by whether the local feature was congruent with the global percept. Teufel et al. (2018) manipulated the presence of high-level representations using two-tone images, which are perceived as meaningless black-and-white patches on initial viewing, but once the observer has acquired relevant prior knowledge of the image content, the patches are perceptually organised into meaningful objects. Psychophysical testing measured the perceptual sensitivity to local contrast and orientation by embedding a small edge probe in the two-tone image. For local probes with an orientation congruent to the high-level percept, the perceptual sensitivity in both contrast detection and orientation discrimination was better when the two-tone image was perceived as a coherent object rather than as meaningless patches. This difference was not observed when the probe orientation was orthogonal (incongruent) to the local orientation predicted by the high-level representation. In other words, the results

indicated an enhancement in the sensitivity to local features that are congruent with the global percept, while no suppression was found in the sensitivity to local features incongruent with the global percept.

These findings suggest that the relationship between local low-level features and the high-level representation may be important for the direction of top-down modulation. However, Teufel et al. (2018)'s study only observed a top-down enhancement to local sensitivity and no suppression to local features incongruent with the high-level percept. This may be explained by the fact that the high-level representation in the stimulus was created by the two-tone image, thus the edge probe with an incongruent local orientation was a completely irrelevant visual element to the high-level percept and not a component of it, resulting in its perception not modulated by the high-level representation. Therefore, I propose that when a local low-level feature is an integral part of a stimulus that elicits a high-level representation, the top-down processing may have the potential to both sharpen and dampen perceptual sensitivity to the local feature; what determines the direction of the top-down modulation is whether or not the low-level feature in question contributes to the high-level representation. Specifically, when a low-level feature contributes to the high-level representation, the sensitivity to this feature is enhanced, whereas the sensitivity to features that do not contribute to the global percept gets suppressed by top-down modulation.

The current study tests this hypothesis using a dynamic point-light walker stimulus, in which the locations and motion trajectories of local points lead to a robust high-level percept of a walking person. The presence of the high-level walker Gestalt is manipulated by presenting the stimulus in its normal configuration or scrambling the position of points, which prevents the generation of a high-level percept. An additional low-level feature, local orientation, is implemented in the stimulus by embedding gratings at the locations of joints in the point-light walker. To manipulate the extent to which local orientations contribute to the global walker percept, orientations of the gratings are either aligned or not aligned with the limbs of the walker. Specifically, local orientations contribute to the global walker percept in the Gestalt-Collinear (G-C) condition, in which all gratings are aligned with the limbs of the walker (see Figure 5.1A). Local orientations in such an arrangement are not only congruent with the high-level percept but also have been shown to actively contribute to the robust perception of the walker Gestalt (Poljac et al., 2011). In contrast to the G-C condition, in the Gestalt-NonCollinear (G-NC) condition, local orientations do not align with the walker's limbs and do not contribute to the high-level percept (as seen in Figure 5.1B). It is predicted that observers are more sensitive to local orientations when they contribute to the high-level walker percept (in the G-C condition) than when they do not contribute (in the G-NC condition). To further investigate whether such a difference is underpinned

by enhanced sensitivity to the contributing features, suppressed sensitivity to the non-contributing features, or both, orientation sensitivity in Gestalt conditions is compared to control conditions, in which the high-level representation of a walker is absent.

Unlike most psychophysical studies on the effect of top-down modulation in early visual processing, the current study employs a browser-based online task with a comparatively large sample size ($N > 520$) which enables individual differences analyses. If both an enhancement of contributing features and a suppression of non-contributing features are found, the relationship between the extent of these two types of top-down modulation can be assessed. An understanding of this relationship could constrain the theorising about different aspects of top-down processing. For instance, it may be possible to infer whether contribution enhancement and non-contribution suppression arise from the same underlying mechanism, or whether they are independent processes. Moreover, the individual differences analyses will also assess whether there is a relationship between the extent of an observer's top-down modulation and their baseline orientation sensitivity, as predicted by Bayesian observer and predictive processing models (e.g., Aitchison & Lengyel, 2017; T. S. Lee & Mumford, 2003; Rao & Ballard, 1999).

In sum, this study aims to examine whether high-level representations differentially modulate the perceptual sensitivity to low-level local features, depending on whether the low-level features contribute to the high-level representation. Specifically, the study provides a means to test the hypothesis that top-down modulation is underpinned by enhanced perceptual sensitivity to contributing local features, and suppressed sensitivity to non-contributing local features, integrating seemingly contrasting findings of previous studies. In addition, individual differences analyses explore the relationship between top-down enhancement and suppression of local features and link these effects to the baseline sensitivity of early visual processing.

5.2 Methods

5.2.1 Participants

A total of 541 participants (299 females and 239 males, the remainder chose "other" or did not report their gender. Mean age = 26.80, SD = 9.63) with normal or corrected-to-normal vision took part in the study. Among them, 432 were recruited via the participant recruitment website Prolific (https://www.prolific.co/) and were each paid £8 per hour in return for their time, the rest were undergraduate Psychology students at Cardiff University taking part in the study for course credits and a potential £4 cash bonus. All participants gave informed consent before the study and were fully debriefed

at the end of testing. The study was designed in accordance with the Declaration of Helsinki and approved by Cardiff University School of Psychology Ethics Committee.

5.2.2 Stimuli

The experiment was written in JavaScript using the jsPsych library (de Leeuw, 2015) and was hosted on Pavlovia (https://pavlovia.org/). The stimulus images used in the experiment were generated using Matlab (The MathWorks, Natwick, MI, USA) and Psychophysics toolbox extensions (Brainard, 1997; Kleiner et al., 2007; Pelli, 1997).

Stimuli of the Gestalt-Collinear (G-C) condition (see Figure 5.1A) were based on Vanrie and Verfaillie (2004)'s point-light walking motion sequence obtained via motion capture. The 30-frame motion sequence contains a loopable one-second gait cycle from the side view. The coordinates of the point-lights were interpolated to the frame rate used in the experiment (60 Hz). Each of the 13 point-lights in the walking motion sequence was replaced by a noisy grating (the method for generating noisy gratings is detailed below). The whole point-light walker stimulus had a dimension of 314*198 pixels.

Stimuli of the Gestalt-NonCollinear (G-NC) condition (see Figure 5.1B) were generated by pseudo-randomly permuting the orientation profiles of all the non-head patches in the G-C stimulus, so that the temporal orientation profile of each non-head patch was allocated to a different patch location. Consequently, G-C and G-NC stimuli contain identical orientations and temporal orientation profiles but these were assigned to different locations.

To quantify the top-down modulation from the high-level walker percept on the sensitivity to local orientations, the G-C and G-NC conditions were contrasted with control stimuli without any high-level gestalt. Two NoGestalt control conditions were created to match the collinearity profiles of local orientations in the two Gestalt conditions. In the G-C stimuli, local orientations are collinear, in other words, they align with each other. Its control condition, the NoGestalt-Collinear (NG-C) condition, retains the same local collinearity while removing the high-level percept of a walker. By contrast, the local orientations in the G-NC stimuli do not align, and this lack of collinearity is replicated in the NoGestalt-NonCollinear (NG-NC) control condition.

Stimuli of the NG-C condition (see Figure 5.1C) were created based on the G-C stimuli via the following steps. First, the G-C stimulus was inverted vertically. Then each of the four limbs of the inverted walker was given a random starting phase within the walking cycle. Finally, the positions of the four limbs were re-arranged: positions of the shoulder and hip patches were reassigned by rotating the positions of these four joints counterclockwise by one position. The remaining limb patches were moved

accordingly so that the relative position of patches within each limb remained the same as in the walker. Stimuli of the NG-NC condition (see Figure 5.1D) were created from the G-NC stimuli in the same way (i.e., inversion, limb phase randomisation, limb position re-assignment).

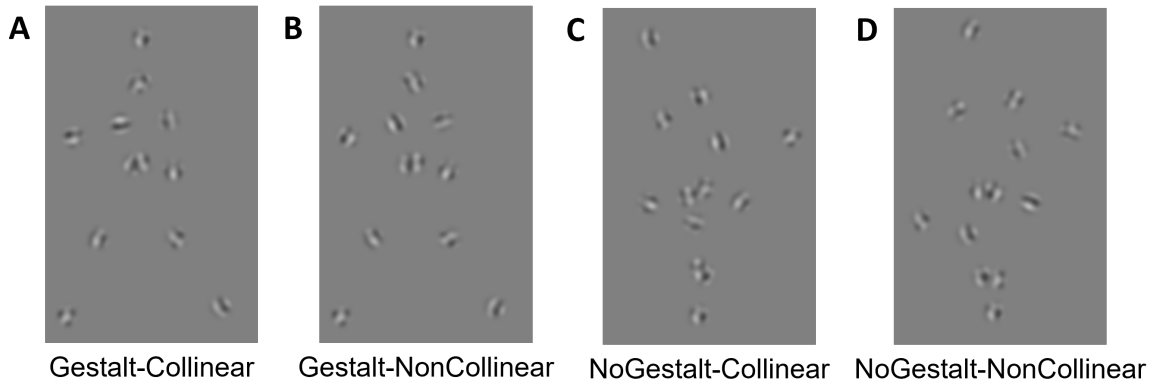

Figure 5.1: **Static illustrations of the dynamic stimuli in the four conditions.** **(A)** Gestalt-Collinear (G-C) condition, **(B)** Gestalt-NonCollinear (G-NC) condition, **(C)** NoGestalt-Collinear (NG-C) condition, **(D)** NoGestalt-NonCollinear (NG-NC) condition. Example dynamic stimuli can be found via this link. The two Gestalt conditions both led to the perception of a walker. However, in the G-C condition, the gratings were arranged in such a way that the local orientations contributed to the high-level walker percept. Conversely, local orientations did not contribute to the walker percept in the G-NC condition. The two NoGestalt conditions led to no organised high-level percept but matched the local collinearity properties of the two Gestalt conditions.

Stimuli of all four conditions were made of the same set of 13 noisy gratings. The same noisy grating was used as the head patch (or its equivalent in NoGestalt stimuli) in all conditions. The remaining 12 noisy gratings were randomly allocated to the 12 non-head patch locations. Two stimuli were generated for each condition, differing only by the allocation of noisy gratings to non-head positions.

As suggested by theoretical considerations (Teufel & Fletcher, 2020), previous empirical findings (de Lange et al., 2018) and my own pilot data, the influence of top-down processing increases with sensory uncertainty. Therefore, orientation noise was injected into the gratings in the following way (for a similar procedure, see Neri, 2014). Each noisy grating was generated by overlaying a target grating (with a spatial frequency of 0.0781 cycles/pixel, a contrast of 1 and a random phase) with 15 noise gratings (with the same spatial frequency as the target grating and random phases). The orientations of the noise gratings were linearly spaced around the orientation of the target grating to cover the full range of orientations. The contrast of each noise grating was drawn from a normal distribution with a mean of 0.2 and a sigma of 0.05. The greyscale values of

target and noise gratings were summed and then normalised to between 0.25 and 0.75 (with a greyscale value of 0 being black and 1 being white). Finally, the noisy grating was wrapped in a circular envelope with a sinusoidally modulated edge to make a round patch with a smooth boundary.

The grating presented during the response period in each trial was free from orientation noise and had a contrast of 1 (its greyscale value varied between black and white). Otherwise, it was identical to the noisy gratings.

5.2.3 Procedure

The study was conducted as a browser-based online task. Most of the participants (432) completed the task using their own laptop or workstation at a location of their choice, while 109 participants completed the same browser-based testing in a computer room at Cardiff University with an experimenter present.

As illustrated in Figure 5.2, in each trial of the experiment, participants viewed a one-second dynamic presentation of the stimulus, which consisted of one walking cycle in the Gestalt conditions (or the equivalent in the NonGestalt conditions). The dynamic presentation in each trial started at a random phase within the loopable cycle. As the dynamic presentation finished, it paused at the ending frame for 400 ms. Then one of the non-head patches (or the NG equivalents) was indicated as the target patch by enlarging it from 27*27 pixels to 45*45 pixels for 300 ms before returning to its original size for 700 ms. After a blank screen of 400 ms, a noise-free response patch appeared at the location of the target patch with a random orientation. The participants were instructed to rotate the response patch to recreate, as closely as possible, the orientation of the target patch by pressing the 'G' and 'H' keys on their keyboard. In order to drive performance to its optimum, after submitting the answer by pressing the space bar, participants were given feedback on the difference between the orientation of their answer and the orientation of the target patch (e.g., '6.05 degrees from target'). Participants were instructed to recreate the target orientation as accurately as possible to minimise this response error.

As described earlier, two stimuli were generated for each condition, differing only by which patch position each noisy grating was allocated to. Each of the 12 non-head patches in each stimulus was used as the target patch in one trial (for 219 participants) or two trials (for 322 participants), resulting in 24 or 48 trials in each condition. The shorter version of the experiment was conducted initially, but after more experience with online testing I decided to double the number of trials to reduce the effect of noisy data in online testing. Trials of the four conditions were randomly interleaved, and participants could take a self-paced break after every 16 trials. At the beginning of the

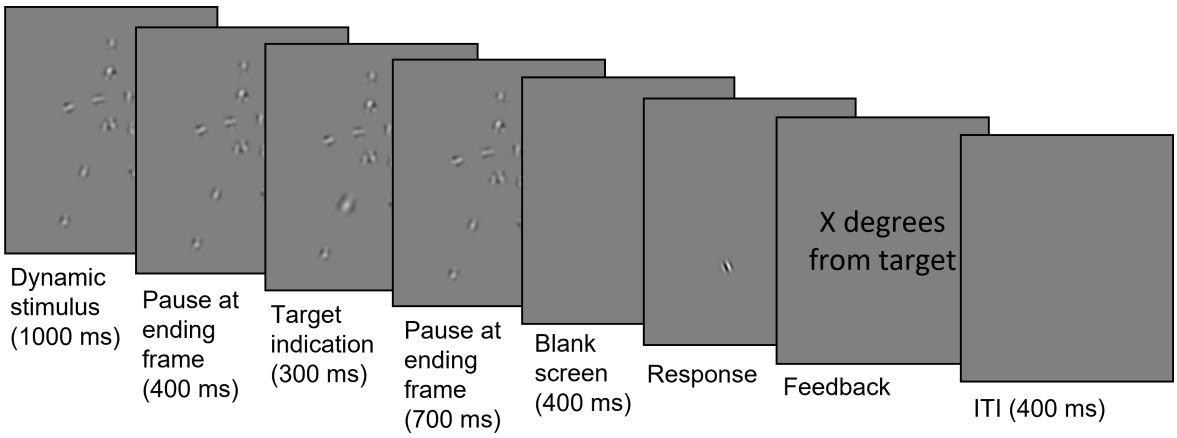

Figure 5.2: **Illustration of an example trial.**
Observers viewed a dynamic stimulus that, depending on the condition, was experienced as a walking person or as gratings moving without forming a coherent high-level percept. This illustration used an example Gestalt-Collinear stimulus. Once the dynamic presentation stopped, one of the gratings was enlarged to indicate the target patch. Finally, observers were asked to adjust the orientation of the response grating in such a way that it matched, as closely as possible, the orientation of the target grating.

experiment, participants were given task instructions and did eight practice trials (two trials of each condition, with the trial order randomised) before starting the main task. Only results of the main task were analysed.

5.2.4 Data processing

Data processing and analysis were carried out in RStudio (version 2022.02.3) with R version 4.2.0. Given that the study was conducted as an online experiment, the data were noisier than what could be expected from a lab-based study. To remove trials in which participants might have been distracted or not doing the task as instructed, trials with an outlier reaction time or outlier response error were excluded from each participant's data. Outliers were defined as values above $Q3 + 3 \times IQR$ or below $Q1 - 3 \times IQR$ within each participant's data set. On average, 2.94% trials were excluded from each participant's data (SD = 2.34%).

Following trial exclusions, participants who did not engage with the task were excluded. A participant was considered as non-engaged if they consistently submitted answers without first rotating the response patch. More specifically, each participant's data were divided into four blocks, each containing the first, second, third and fourth 25% of trials, respectively. A participant was excluded from analysis if any of their blocks had (i) a mean rotation of below 20 degrees before submitting answers or (ii) an outlier mean rotation or an outlier standard deviation of rotation among all par-

ticipants. After excluding 20 non-engaged participants (3.70%), 521 participants were entered into the analyses (287 females and 231 males, mean age = 26.72, SD = 9.54). Among these participants, 2.90% of trials were excluded in total.

The measure of interest in this experiment is the perceptual sensitivity to local orientations in each condition. Since the response error in each trial can range between -90 and 90 degrees, and a greater deviation from 0 degrees indicates a less accurate recreation of the target orientation, the more tightly response errors cluster around 0 degrees, the more precise the recreation of the target orientation. Therefore, the perceptual sensitivity to local orientations can be indexed by a measure of the spread of response errors in a particular condition. I chose the interquartile range (IQR) as an appropriate measure of spread and did not use standard deviation (SD) due to the noisiness of the data. SD can be easily skewed by a small number of trials whose response errors substantially deviated from most trials. In contrast, the IQR was a more robust measure of the spread of response errors. Note, however, that all analyses were also carried out using the SD of response errors as the dependent measure, which yielded the same pattern of results as those reported below (see Appendix 9).

5.3 Results

Data of all conditions in the current study were non-normally distributed (Shapiro-Wilk test $p < .05$), thus pairwise comparisons were conducted using non-parametric Wilcoxon Signed-Rank Tests and correlational analyses were conducted using non-parametric Spearman's correlations. A total of five pairwise comparisons and three correlations were carried out. All tests were planned, and each tested an individual null hypothesis, thus the significance threshold was not corrected for multiple testing (Rubin, 2021).

5.3.1 Differential modulation of contributing and non-contributing features

Local orientations contributed to the walker percept in the G-C condition but not in the G-NC condition. The response error IQR was significantly smaller in the former (Mdn = 16.21, M = 17.34, SD = 7.05) than in the latter condition (Mdn = 17.35, M = 19.31, SD = 9.47), Z = 50559, $p = 3.97 \times 10^{-7}$, as illustrated in Figure 5.3A and the left panel of Figure 5.3C. Although the effect was small, this result is consistent with the notion that perceptual sensitivity is higher for local orientations that contributed to the high-level percept than for non-contributing orientations.

It may be argued that this difference could be the result of different local collinearity in the two conditions instead of differential top-down modulations. Local orientations

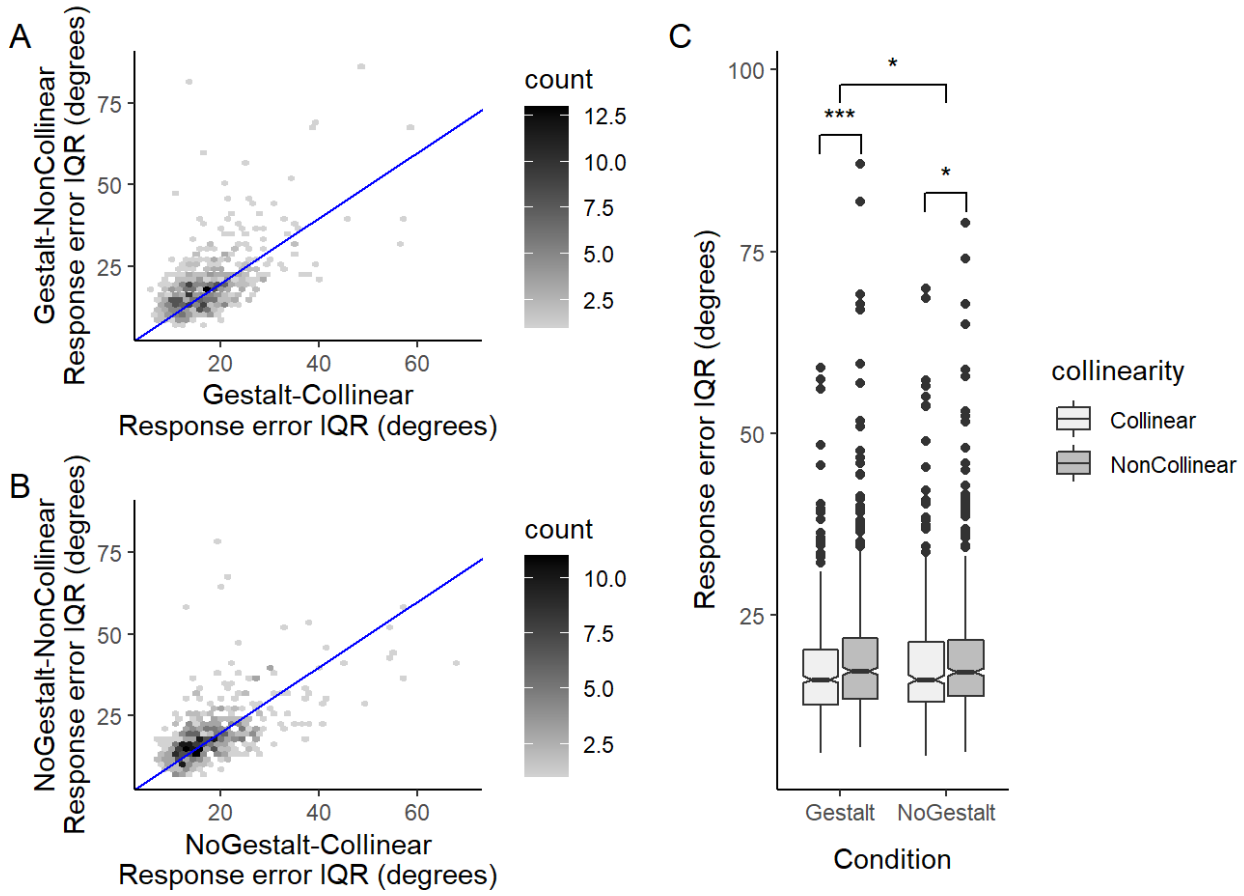

Figure 5.3: **Comparisons of perceptual sensitivity between the two Gestalt conditions and between the two NoGestalt conditions.**
In the hexagonal heatmaps illustrating the relationship between the two Gestalt conditions **(A)** and between the two NoGestalt conditions **(B)**, the greyscale colour indicates the density of data points in each hexagonal bin. The blue line indicates equal response error IQR in the two plotted conditions. The larger the response error IQR, the lower the perceptual sensitivity; thus more data above the blue line suggests that most participants' perceptual sensitivity was worse in the NonCollinear condition than in the Collinear condition. **(C)** The perceptual sensitivity was significantly better in the Collinear stimuli than in the NonCollinear stimuli for both Gestalt and NoGestalt conditions, but this difference was larger between Gestalt conditions than between NoGestalt conditions. $^{*}p < .05$, $^{***}p < .001$.

of patches assigned to the same limb align with each other in the G-C condition but not in the G-NC condition. This local collinearity could contribute to performance and make it easier to recreate orientations and thus yield smaller response errors. To test this notion, the extent of the collinearity effect was quantified by the difference between the two NoGestalt control conditions. As seen in Figure 5.3B and the right panel of Figure 5.3C, the perceptual sensitivity was indeed slightly better in the NG-C condition ($Mdn = 16.19$, $M = 18.25$, $SD = 8.17$) than in the NG-NC condition ($Mdn = 17.18$,

$M = 19.10$, $SD = 9.07$), $Z = 60867$, $p = .038$, suggesting that local collinearity led to slightly better task performance. However, the difference between Collinear and NonCollinear conditions was significantly bigger in the Gestalt comparison ($Mdn = 1.11$, $M = 1.97$, $SD = 7.84$) than in the NoGestalt comparison ($Mdn = 0.38$, $M = 0.85$, $SD = 7.50$), $Z = 75853$, $p = .011$, indicating that the collinearity effect could not fully explain the difference in sensitivity for contributing and non-contributing local orientations in the Gestalt stimuli.

5.3.2 Direction of modulation

Two further pairwise comparisons were carried out to explore whether the differential top-down modulations were driven by enhanced sensitivity to contributing local orientations, suppressed sensitivity to non-contributing local orientations, or both. This was achieved by comparing the two Gestalt conditions to their respective NoGestalt control condition. The NoGestalt conditions provided measures for the baseline orientation sensitivity without the influence of top-down modulation while matching the local collinearity in the Gestalt conditions.

As illustrated in Figure 5.4, the response error IQR in the G-C condition ($Mdn = 16.21$, $M = 17.34$, $SD = 7.05$) was significantly smaller than in the NG-C condition ($Mdn = 16.19$, $M = 18.25$, $SD = 8.17$), $Z = 56846$, $p = .001$, indicating enhanced orientation sensitivity when local orientations contributed to the global percept than when there was no global percept (but with matched collinearity). By contrast, the response error IQR in the G-NC condition ($Mdn = 17.35$, $M = 19.31$, $SD = 9.47$) did not differ from that in the NG-NC control condition ($Mdn = 17.18$, $M = 19.10$, $SD = 9.07$), $Z = 69487$, $p = .663$, suggesting no suppression in the sensitivity to non-contributing local orientations compared to when there was no top-down modulation from a global percept.

5.3.3 Individual differences

Three correlation analyses were conducted to explore individual differences in how top-down modulation affects early sensory processing. First, to assess whether the top-down modulations for contributing and non-contributing local features are independent processes or arise from the same underlying mechanism, I analysed the relationship between the extents of top-down enhancement for contributing local orientations and suppression for non-contributing orientations. As illustrated in Figure 5.5, no correlation was found between the two variables, $p = .565$, suggesting that top-down modulation for contributing local features was not related to that for non-contributing local features.

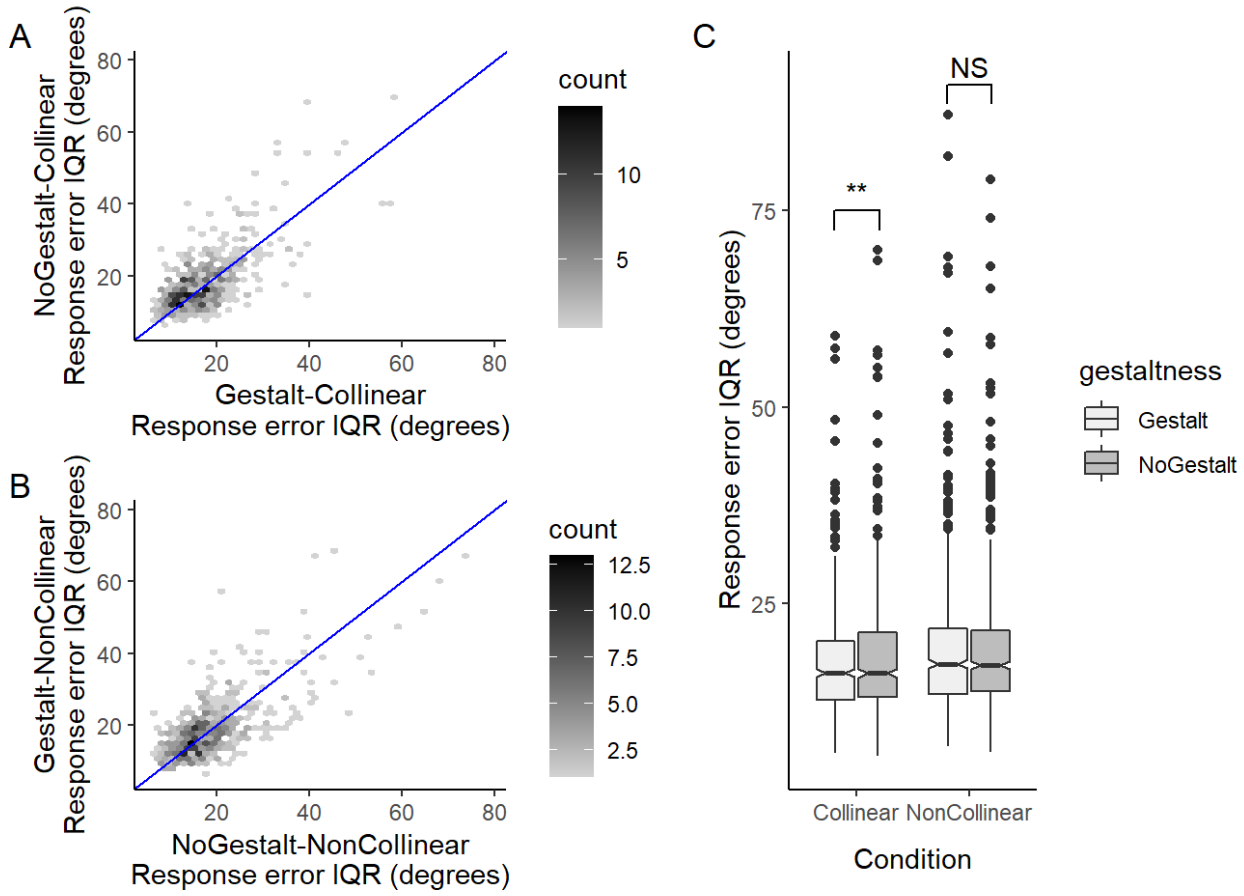

Figure 5.4: **Comparisons of perceptual sensitivity between the two Collinear conditions and between the two NonCollinear conditions.**
Same convention as for Figure 5.3 applies to this figure. More data above the blue line in **(A)** indicates most participants showed enhanced sensitivity to contributing local orientations compared to the baseline. This enhancement was significant, as illustrated by the comparison on the left in **(C)**, $^{**}p < .01$. More data above the blue line in **(B)** would suggest suppressed sensitivity to non-contributing local orientations compared to the baseline, but this comparison was non-significant, as indicated by the comparison on the right in **(C)**, ns $p > .05$.

Given that the NG-NC condition had no global percept and no local collinearity, I used this condition as an index of the observers' baseline perceptual sensitivity to local orientations. This baseline orientation sensitivity was related to the extent of differential top-down modulations between contributing and non-contributing local orientations, indexed by the difference in the response error IQR in the G-NC and the G-C conditions. As seen in Figure 5.6, observers with poorer baseline sensitivity, as indexed by larger response error IQR in the NG-NC condition, showed a slightly bigger difference between the sensitivity to contributing and non-contributing local orientations, $r(519) = 0.09$, $p = .048$. This weak but significant positive correlation indicated that individuals with

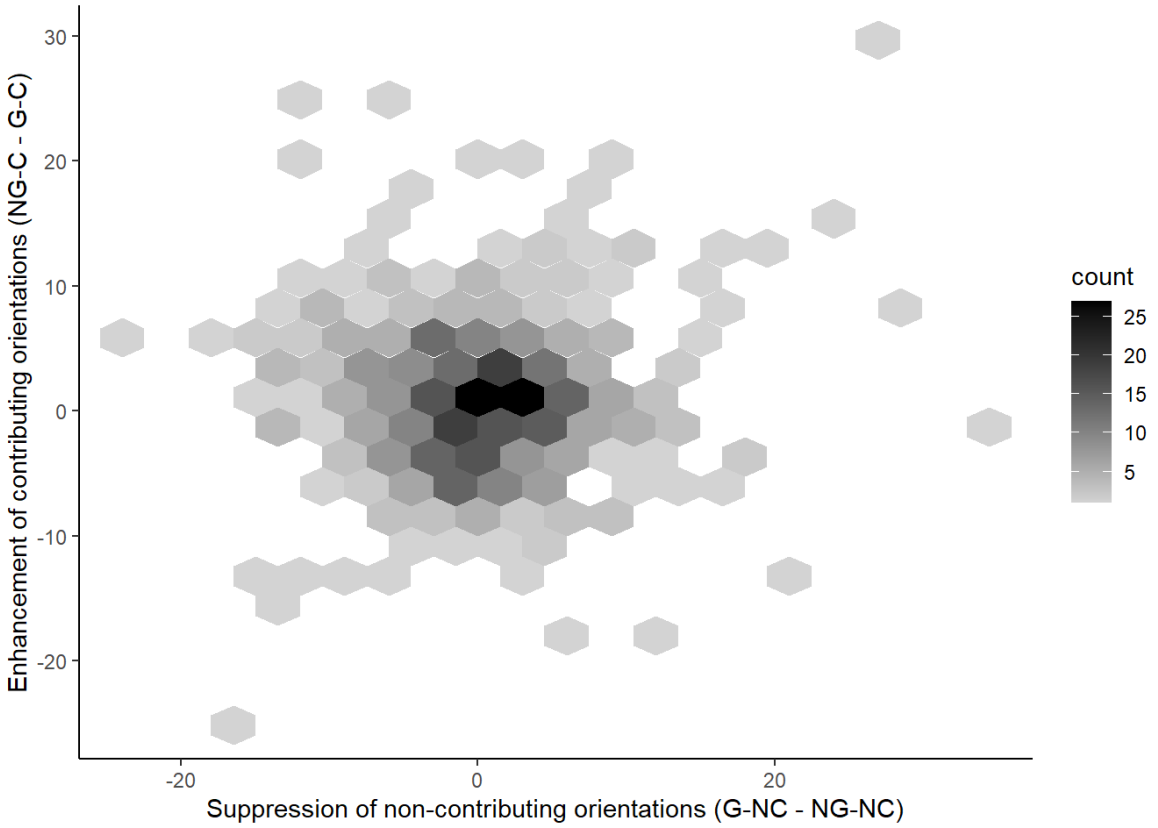

Figure 5.5: **Relationship between observers' sensitivity enhancement for contributing local orientations and sensitivity suppression for non-contributing local orientations.**
In the hexagonal heatmap illustrating the relationship, the greyscale colour indicates the density of data points in each hexagonal bin.

less reliable sensory processing had greater differential top-down modulations on early sensory processing.

To further assess the link between baseline perceptual sensitivity and top-down processing, I related the baseline performance in the NG-NC condition to the extent of sensitivity enhancement for contributing local features, quantified as the difference between the orientation sensitivity in the G-C condition and in its NoGestalt control condition (the NG-C condition). As seen in Figure 5.7, the top-down enhancement was found to be weakly but significantly correlated with the NG-NC response error IQR, $r(519) = 0.10$, $p = .023$, suggesting that individuals with poorer baseline orientation sensitivity had slightly larger top-down enhancement on the sensitivity to local orientations that contributed to the global percept.

The relationship between the baseline orientation sensitivity and the top-down suppression of non-contributing local orientations was not assessed. Because the extent of the top-down suppression was indexed by the difference between the G-NC and NG-NC

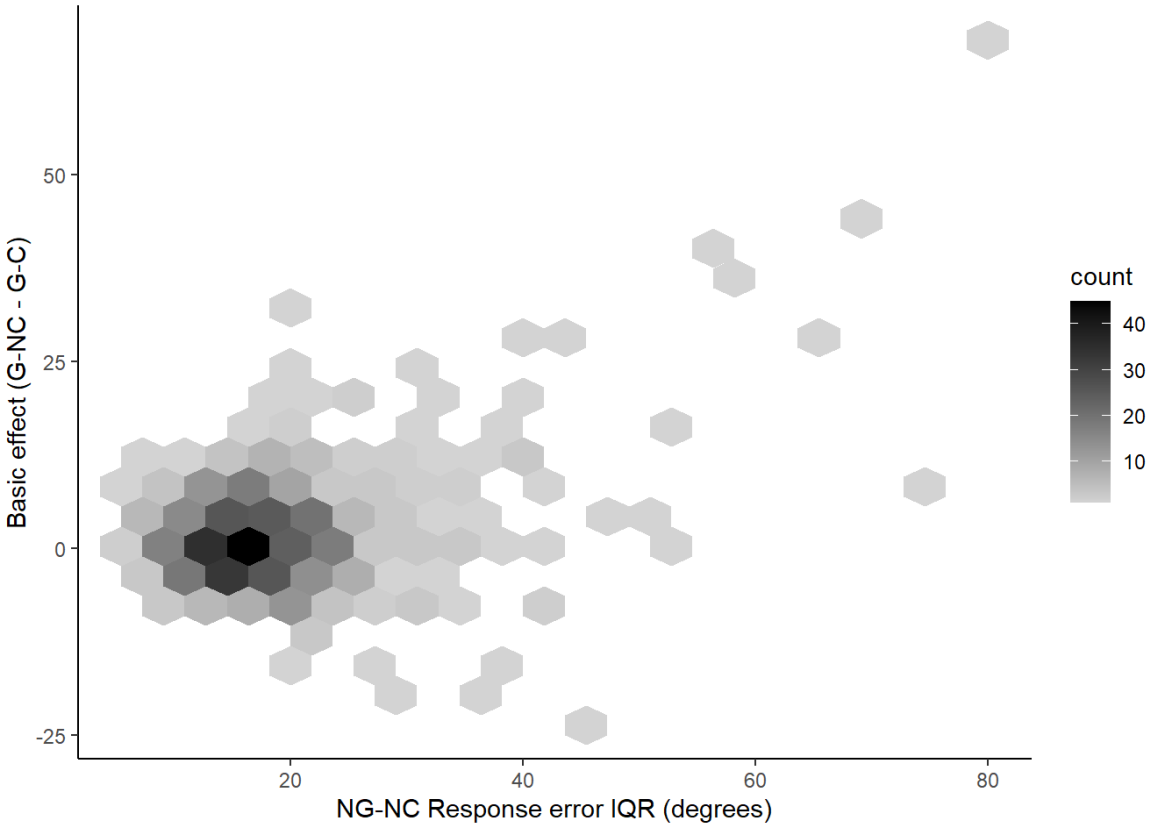

Figure 5.6: **Relationship between observers' baseline orientation sensitivity and their extent of differential modulations for contributing and non-contributing orientations.**
The baseline perceptual sensitivity is indexed by the response error IQR (degrees) in the NG-NC condition. The smaller the value, the higher the orientation sensitivity. The extent of the differential top-down modulations is quantified as the size of the basic effect, i.e., the response error IQR in the G-NC condition minus that in the G-C condition.

conditions. Correlating it with the baseline sensitivity in the NG-NC condition would yield a strong negative relationship that is not conceptually meaningful.

5.4 Discussion

The current study used point-light walker stimuli with embedded local orientations to test the hypotheses that high-level representations can modulate the perceptual sensitivity to local low-level features, and the direction of this top-down modulation is determined by whether the local features in question contribute to the high-level global percept.

Consistent with the predictions, the results showed a higher perceptual sensitivity to local orientations that contributed to the global walker percept compared to those that

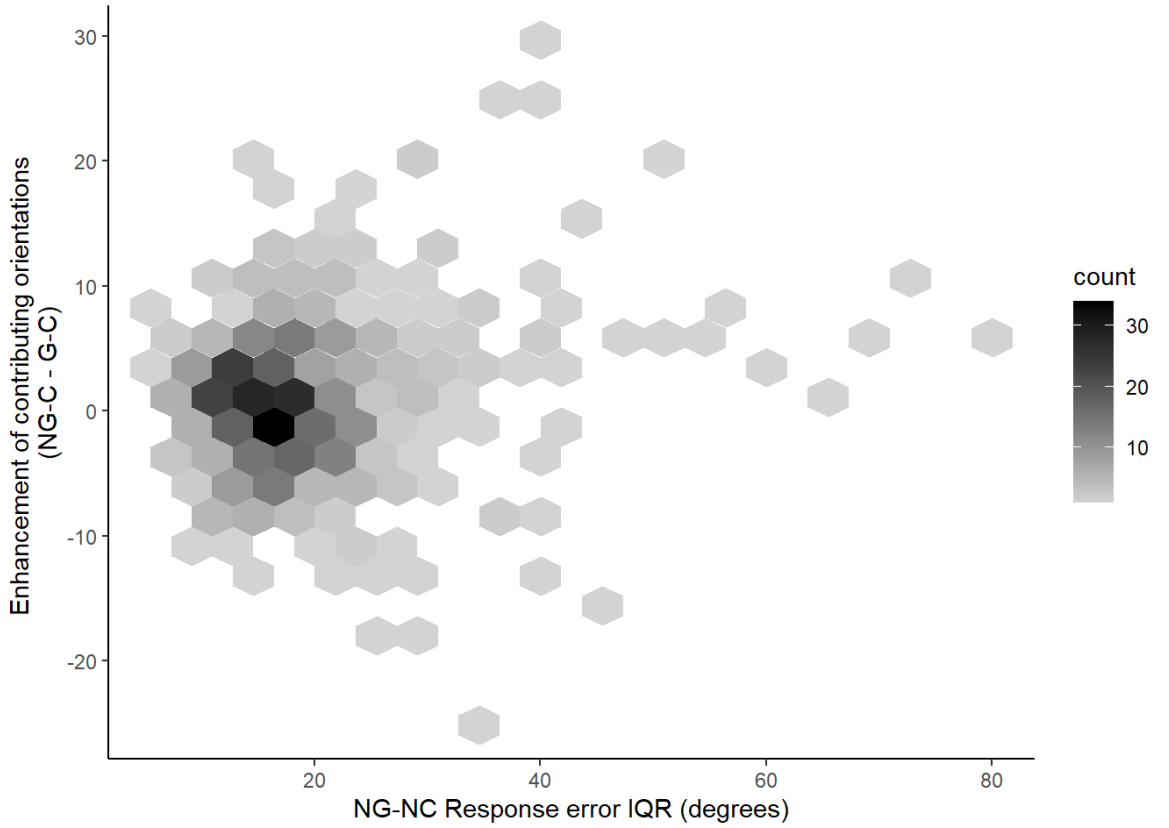

Figure 5.7: **Relationship between observers' baseline orientation sensitivity and sensitivity enhancement for contributing local orientations.**
The baseline perceptual sensitivity is indexed by the response error IQR (degrees) in the NG-NC condition. The smaller the value, the higher the orientation sensitivity. The extent of the sensitivity enhancement was quantified as the response error IQR in the NG-C condition minus that in the G-C condition.

did not contribute to the high-level representation. This difference could not be fully accounted for by the fact that local orientations contributing to the high-level walker percept were also collinear with each other, whereas local collinearity was absent in the condition where orientations were non-contributing to the global percept. Specifically, using two control conditions with the same collinearity profiles as the Gestalt stimuli but without a high-level global percept, it was found that the effect of local collinearity on its own was significantly smaller than the effect observed in the Gestalt conditions.

The two NoGestalt conditions also enabled a more detailed inspection of the underlying mechanism for the contribution-based differential modulation of local orientation sensitivity. Compared to the baseline sensitivity when local elements did not form a high-level percept, there was significant evidence showing enhanced sensitivity to local orientations when they contributed to the global walker percept, whereas the sensitivity was preserved at the baseline level without being suppressed when local orientations were non-contributing to the high-level percept. In other words, early feature detectors

for contributing features were sharpened by top-down modulation, but feature detectors for non-contributing features were not affected.

In addition to group-level analyses, individual differences analyses were also carried out. The extent of top-down enhancement and suppression was found to be unrelated, consistent with the finding of a lack of sensitivity suppression on non-contributing local orientations. Meanwhile, the extent of top-down enhancement was found to be related to the observers' baseline perceptual sensitivity. In particular, poorer baseline sensitivity was associated with a greater extent of contribution-based differential top-down modulations and a larger sensitivity enhancement for contributing local orientations. This suggests that the balance between bottom-up and top-down processing is modulated by the reliability of an individual's sensory processing.

Taken together, the current study found that high-level representations dynamically shape the tuning properties of early feature detectors, that this effect is determined by the relationship between the feature and the high-level representation, and that the extent of this top-down influence is modulated by the reliability of sensory processing. These findings provide direct behavioural evidence for predictive processing and Bayesian observer models that emphasise the interaction between high- and low-level representations in visual processing (e.g., Aitchison & Lengyel, 2017; Friston, 2010; T. S. Lee & Mumford, 2003; Rao & Ballard, 1999; Spratling, 2016; Wei & Stocker, 2015). The high-level object representation provides a template that sets up expectations for the low-level local orientations. These object-based expectations are then integrated with the sensory evidence in a flexible manner, so that the high-level representation selectively modulates the perceptual sensitivity to local features based on the relationship between the local features and the global percept. Moreover, the weighting of the selective top-down influence is also dynamic and flexible, with object-based expectations inserting more influence when the bottom-up sensory processing is less reliable, thus optimising perception.

Note that the contribution-based modulation on low-level perceptual sensitivity discovered in this study is an incidental effect. The presence of a walker percept and its relationship with local orientations were irrelevant to the task for the participants. In all conditions, the task for participants was to recreate local orientations. This only requires participants to attend to the local orientations, not to any global percept. Yet, the effect of contribution still emerged, suggesting that top-down modulation based on high-level representations is a fundamental aspect of visual processing, and it is important in optimising visual perception in an ambiguous and complex visual environment.

The browser-based online task used in the current study enabled a sample size much larger than conventional lab-based psychophysical studies but also yielded very noisy data and small effect sizes. This may be a result of the participants undertaking

the experiment without rigorously controlled lab conditions. Most of the participants completed the task in their own time and at a location of their choice; there was no way of ensuring their uninterrupted attention and full engagement. While the effects in the current study are small, the online testing enabled a sample size large enough for individual differences analyses and was an effective mitigation strategy for conducting behavioural research during the COVID-19 pandemic.

5.4.1 The direction of top-down modulation on perceptual sensitivity

The current study observed a top-down enhancement in the perceptual sensitivity to local features. This is consistent with previous findings in studies by Christensen et al. (2019), Christensen et al. (2015), Lupyan (2017), Namdar et al. (2015), Tadin et al. (2002), and Teufel et al. (2018). While past studies only demonstrated the phenomenon that high-level percepts can enhance the sensitivity to local features, the current study extends previous findings by identifying a factor that modulates this top-down influence, namely, whether the local features contribute to the high-level percept. This modulating factor can explain the sensitivity enhancement in studies mentioned above, as the local features that had an enhanced perceptual sensitivity through top-down processing were features that contributed to the global high-level representation. For example, in Christensen et al. (2015)'s and Christensen et al. (2019)'s studies, the orientation and position of local elements were what enabled the perception of high-level objects. Similarly, in Namdar et al. (2015)'s study of face perception, the distance between facial features was crucial for constructing a holistic face configuration.

While the current study established that high-level representations can enhance the perceptual sensitivity to contributing local features, it did not find evidence for top-down suppression of sensitivity to non-contributing features. This contradicted previous findings of dampened sensitivity to local features as the result of a high-level percept (Mamassian & Zannoli, 2020; Poljac et al., 2012; Wilford & Wells, 2010). However, the absence of top-down suppression in the current study is consistent with the findings of Teufel et al. (2018)'s study, which observed no dampening of sensitivity to local orientation or contrast when the edge probe carrying the low-level attribute was not aligned to the high-level percept in a two-tone image. Prior to conducting the current study, I speculated that the reason Teufel et al. (2018) did not observe a top-down sensitivity suppression was that the edge probe incongruent with the high-level percept was not a part of the two-tone image which gave rise to the high-level percept. In other words, the perception of a visual element unrelated to the high-level percept would not be modulated by its top-down influence. However, in the current study, local

orientations were implemented in visual elements integral to the high-level percept - the Gestalt walker was formed by local gratings, yet the orientation sensitivity was still not suppressed when the local orientations were not contributing to the global percept.

The conflicting findings on the presence or absence of top-down suppression of local features concur with Wagemans (2018)'s observation and categorisation of two types of Gestalts. Wagemans argues that, in the process of perceptually organising visual elements into global percepts, one type of higher-level representation suppresses the perception of the parts ("eliminative Gestalts"), whereas another type of Gestalt ("preservative Gestalts") does not suppress the encoding of parts even though the parts become less functional as the global representation arises. This distinction between eliminative and preservative Gestalts does not account for the cases of top-down enhancement on the perceptual sensitivity of local features. However, incorporating Wagemans (2018)'s categorisation with my notion of contribution-dependent modulation of top-down processing can yield a framework that explains all three observed patterns of the top-down influence on local perceptual sensitivity. Extending the notion that the relationship between local features and the global percept moderates the direction of top-down modulation, I propose that the sensitivity to a low-level local feature is enhanced if the low-level feature contributes to the perception of a high-level representation, the sensitivity of the local feature is suppressed if the perception of the low-level feature weakens the high-level percept, and the sensitivity to the local feature is preserved at the baseline level if the low-level feature is neither contributing nor detrimental to the high-level representation.

This new distinction reconciles findings from the current and previous studies. In past studies that observed top-down suppression of the perception of local features, the local features were not only non-contributing to the global percept but actually detrimental to the robustness of the high-level percept. For example, in Poljac et al. (2012)'s study where the perception of the colour of local elements making up a point-light walker was suppressed by top-down processing, the local colour was a feature that could weaken the global percept, because having distinct colours in different parts of a stimulus can lead to a perception of multiple objects rather than one coherent object. Similarly, Mamassian and Zannoli (2020) showed that grouping visual elements led to impaired depth perception of local elements. This could be explained as varied local depths within an object could make it more difficult to incorporate visual elements to form a coherent global percept. By contrast, in the G-NC condition of the current study, the local orientation sensitivity was not enhanced or suppressed, as local orientations neither contributed to the walker Gestalt nor weakened the global percept. Objects in our visual environment typically contain local edges at various orientations, they are not crucial for forming the high-level representation, but the perception of these

local orientations also does not cause the global percept to disintegrate. Overall, the extended notion of the contribution-dependent modulation of top-down processing can account for top-down enhancement, suppression and non-modulation of local perceptual sensitivity. It indicates that top-down processing sharpens, dampens or preserves low-level sensitivity in a dynamic manner in order to maximise the high-level representation and achieve efficient interpretations of the visual environment. Future studies are needed to explicitly test this notion and establish more specific properties of the model. For instance, it is necessary to clarify how to distinguish whether a local feature contributes to or hinders the global percept or does neither. An initial step of this might be to establish an independent measure to index the robustness of a high-level percept.

5.4.2 Alternative explanations

It may be argued that, instead of the modulation by high-level object representations, it was feature-based attention that selectively enhanced the sensitivity to contributing local orientations and led to the observed results. Findings of the current study cannot be meaningfully explained by attention, because the task of recreating local orientations demands the observer to attend to orientation, so it is unclear how feature-based attention can prioritise orientation even further in one condition than other conditions. Even if this could happen, the effect can only be due to the global percept. Therefore, even the feature-based attention explanation has to argue that it is the high-level representation that leads to differential top-down modulation (via attention), and the top-down processing is determined by the relationship between local features and the global percept.

To more directly rule out the alternative explanation of feature-based attention, a follow-up study could present two spatially overlapping high-level objects, for example, two point-light figures dancing with each other (like in Neri et al., 2006), and make local orientations contributing to the high-level dancer percept in one dancer and non-contributing in the other dancer. Since feature-based attention modulates the perceptual sensitivity to a feature class at the level of location-independent feature maps (Maunsell & Treue, 2006), it would enhance the orientation sensitivity in the whole visual field and not be able to explain the finding if the contribution-based differential modulation persists in spatially overlapping high-level percepts.

Another potential alternative explanation to the effects observed in the current study is that, instead of top-down processing altering the low-level perception of orientation, the effects were a result of a guessing strategy for doing the task. In specific, if participants made guesses about the local orientations based on the limb orientation

of the Gestalt walker, then their recreation of the local orientations would be more accurate in the G-C condition (where local orientations aligned with the limb orientations) than in the G-NC condition (where local and limb orientations did not align), as found in the current study. However, if participants were doing the task this way, the more one relied on this guessing strategy, the more successful they would be in the G-C condition, but the worse their performance would be in the G-NC condition. In other words, it would predict a negative correlation between participants' performance in those two conditions. Whereas, in fact, there was a positive relationship between the performance in G-C and G-NC conditions, as seen in Figure 5.3A. Therefore, it is not likely that this response strategy was used and led to the observed results. It is also not likely that participants could have selectively used this guessing strategy only in the G-C condition and not in the G-NC condition. Because trials of the four conditions were randomly interleaved, and the dynamic presentation in each trial was only one second long, leaving little time for participants to select and apply different strategies for each trial.

5.4.3 Conclusions

In conclusion, the current study demonstrated that low-level perception of local visual features was differentially modulated by high-level representations, depending on whether the local features were contributing to the high-level percept. Perceptual sensitivity to local features contributing to the global percept was enhanced, while the sensitivity to non-contributing features was preserved and not suppressed. The extent of top-down modulation was weakly related to the reliability of the individual's sensory processing. These findings extended our understanding of how high-level representations dynamically and flexibly interact with early visual processing, identifying the relationship between low-level features and the high-level percept as an important factor modulating the top-down tuning of perceptual sensitivity.

Chapter 6

General discussion

6.1 Summary of findings

Previous chapters of this thesis presented two lines of research that originated from my plan to use the frequency-tagging technique for investigating the neuronal mechanism of top-down processing in perceptual organisation. As a result of initial difficulties in eliciting harmonic and intermodulation components of VSSR, I investigated the VSSR power as a function of stimulation frequency and explored the functional implications of the individual variability in this temporal response tuning profile. Concurrently, I conducted an online psychophysical study to investigate the top-down influence of perceptual organisation in preparation for using this task in future frequency-tagging studies.

Chapter 2 demonstrated that VSSR evoked by fixed-frequency flickers could be adequately approximated by neural responses evoked by visual chirp stimuli. Using these visual chirp stimuli, a finely-sampled temporal response tuning profile was established for stimulation frequencies of 1-80 Hz. In addition to characterising the group-level tuning profile for the fundamental component and the second to seventh harmonics, substantial individual variability in the temporal response tuning profile was observed: profiles were distinct between but consistent within individuals across measures and testing sessions.

Chapter 3 then assessed whether the individual variability in the temporal response tuning profile was associated with the individual's perceptual temporal resolution (the CFF threshold) and the peak frequency of visually induced gamma oscillations. It was found that the CFF threshold was positively related to the individual's upper limit of VSSR responsiveness and the VSSR power at around 57 Hz, indicating a potential role of neural responsiveness in determining the upper bound of an individual's ability to resolve percepts in time. In contrast, no relationship was found between the temporal

response tuning profile and the peak frequency of induced visual gamma, suggesting that it remains unclear whether and how evoked and induced oscillations interact in feedforward visual processing.

Having measured the CFF threshold and induced visual gamma oscillations in a healthy cohort of individuals, the relationship between these two visual phenomena was explored in Chapter 4. The perceptual temporal resolution indexed by the CFF threshold was found to be unrelated to features of the visual gamma oscillations. By modelling the cortical microcircuitry generating visual gamma using Dynamic Causal Modelling for steady-state responses (DCM-SSR), it was found that model parameters that are thought to reflect synaptic properties of the cortical microcircuitry underlying visual gamma were also unrelated to the CFF threshold. Both the data features of visual gamma and the computational model suggested that an individual's perceptual temporal resolution was not determined by the neuronal networks generating induced gamma oscillations.

In my second line of research, Chapter 5 presented an online psychophysical study investigating how perceptually organised high-level representations exert top-down modulation on early sensory processing. While past studies in the literature disagreed on whether high-level global representations enhance or suppress the perceptual sensitivity to low-level local features, my study showed that the direction of top-down modulation was determined by whether or not the low-level local feature contributed to the high-level representation. In particular, local features that contributed to the high-level representation were perceived with enhanced sensitivity, whereas the perceptual sensitivity to non-contributing local features was preserved at the baseline level. The extent of the contribution-based differential top-down modulation and the extent of sensitivity enhancement for contributing local features were slightly larger for individuals with poorer baseline perceptual sensitivity. These findings were consistent with predictive processing and Bayesian observer models, extending our understanding of how high- and low-level perception dynamically interact in perceptual organisation.

6.2 Temporal response tuning profile

6.2.1 Methodological and conceptual significance

The MEG study presented in this thesis established a finely-sampled temporal response tuning profile for a wide range of stimulation frequencies. However, this response tuning profile is based on the particular stimulus and apparatus used in my study, and many aspects of the stimulus and apparatus have been shown to affect the VSSR tuning function, as discussed in Chapter 2. Due to this stimulus specificity, the tuning profile

presented in Chapter 2 may only be used cautiously to directly inform the choices of stimulation frequency in future studies using VSSR as a research tool or clinical intervention. Yet, the findings presented in this thesis are still of both methodological and conceptual value.

Methodologically, this thesis provides a proof of concept for efficiently establishing an individual's temporal response tuning function using visual chirp stimuli. This is one of the most important takeaways from the current thesis and should lead to changes in the standard practice of all future uses of the VSSR. Given that the VSSR profile can be stimulus-specific and largely variable between individuals, the best way to evoke maximal VSSR power in each participant is to establish an individualised temporal response tuning function using the particular apparatus and stimulus for that particular usage scenario (e.g., a frequency-tagging study, a VSSR-based clinical intervention, or a brain-computer interface [BCI] set-up). This can be done efficiently using a relatively small number of trials of visual chirp spanning the frequency range of interest, taking only a few minutes to run. The analysis of the resultant M/EEG recording is relatively simple and can be potentially conducted on the fly. Once a temporal response tuning function is derived from the chirp-evoked responses, optimal stimulation frequency can be selected for the specific participant and applied to the subsequent VSSR stimuli. Selecting stimulation frequencies that drive strong and robust neural responses is crucial for all applications of the VSSR. For instance, in frequency-tagging studies, the intermodulation (IM) responses are typically weaker than fundamentals (e.g., Alp et al., 2016; Gundlach & Müller, 2013; Vergeer et al., 2018), so using tagging frequencies that drive strong fundamentals would increase the opportunity of observing any effect in the IM components. Implementing the procedure described above as a standard practice to select optimal stimulation frequencies using visual chirps should lead to higher-quality data in frequency-tagging research, more effective VSSR-based clinical interventions and more efficient BCI systems.

Besides methodological value, the findings of my visual chirp study are also of conceptual significance. By demonstrating that the individual variability in the temporal response tuning profile is stable, distinct for the individual, and associated with the visual temporal resolution, my findings indicate that the temporal response tuning profile is an index of intrinsic properties of an individual's visual system and a functional correlate of visual processing. Just as auditory steady-state responses (ASSR) have been used to probe the functioning and capacity of the auditory neural pathway (O'Donnell et al., 2013a), the VSSR profile can reflect functional properties of one's visual system. For example, the frequency of the strongest VSSR indicates the resonance or working frequency of the relevant neural circuit (Bayram et al., 2011; Herrmann, 2001), and the VSSR power at different frequencies can reflect the ability of the relevant neu-

ronal network to generate and support oscillatory activities in various frequency bands (Griskova et al., 2007; O'Donnell et al., 2013a; Uhlhaas et al., 2010). Since the generation of VSSR may rely on the same neuronal networks involved in other visual and cognitive processes, the spectral features of the VSSR profile may indicate the neural efficiency of visual processing.

6.2.2 Future directions

To further explore the functional implications of the temporal response tuning profile, it would be interesting to assess its relation to other properties of an individual's visual system and cognitive processing. For instance, to establish the structure-function relationships underlying the individual variability in the temporal tuning profile, future studies could assess whether an individual's temporal response tuning profile is related to the microstructure of the visual cortex, as well as the structural and functional connectivity of the visual cortex. Furthermore, future research could adopt clinical and developmental perspectives to characterise the changes in the temporal response tuning profile in clinical cohorts and individuals at different developmental stages over the lifespan. Just like abnormalities in amplitude and phase coherence of gamma-band ASSR have been associated with altered neural synchronisation in conditions like schizophrenia (O'Donnell et al., 2013b; Onitsuka et al., 2022; Tada et al., 2020) and autism spectrum disorder (Rojas & Wilson, 2014; Seymour et al., 2020), features of the VSSR tuning profile might also vary between clinical and control cohorts. By combining this knowledge with our understanding of the structural and functional changes in the brain at various developmental and clinical stages, features of the temporal tuning profile may be established as biomarkers with developmental and clinical significance.

Past studies involving the VSSR have used a wide range of stimuli and apparatuses. Future research could systematically investigate how different stimulus attributes affect the VSSR and the temporal response tuning profile. It remains unclear how the amplitude, phase coherence and spatial distribution of the VSSR and spectral features of the temporal response tuning profile vary as a result of differences in stimulus wavelength, luminance, structural complexity (e.g., whether the periodically modulated stimulus is unpatterned, a simple pattern such as grating or checkerboard, or a more complex naturalistic image), and the time taken to process the stimulus (e.g., simple geometric shapes versus face identities or object categories). A comprehensive understanding of how the VSSR and the temporal response tuning profile are modulated by various factors could further our understanding of the neural pathways underlying the responses and provide inspirations for how the VSSR can be used as a research tool, clinical biomarker or treatment for diseases. For instance, the knowledge of what stimulus

attributes lead to the strongest VSSR in the gamma band could aid the development of using gamma entrainment as an intervention for Alzheimer's disease (AD) (K. Lee et al., 2021; Park et al., 2022).

6.3 Using frequency-tagging to study top-down processing in perceptual organisation

The findings of my MEG studies could facilitate future frequency-tagging investigations on the neural mechanisms of top-down processing in perceptual organisation. The two frequency-tagging studies I initially planned (as described in Section 1.3 in the General Introduction Chapter) can be conducted, using visual chirp stimuli to establish individualised temporal response tuning functions and select stimulation frequencies that evoke maximal VSSR for each participant. This would increase the chance of eliciting robust IM responses which are usually of a lower magnitude than fundamental VSSR components. Moreover, frequency-tagging can also be implemented in the point-light walker stimuli described in Chapter 5, so the frequency-tagging results can complement my psychophysical findings. For instance, flickers could be embedded in the gratings that make up the walker (or the control stimuli) with half of the gratings modulated at one frequency and the other gratings at another frequency. Given that IM components are known to index the integration of visual signals, IMs are expected to be stronger in the Gestalt conditions than in the NoGestalt control conditions, and possibly also stronger in the Gestalt-Collinear (G-C) condition than in the Gestalt-NonCollinear (G-NC) condition, indicating that local orientations aligned with the limbs of the walker result in a more robust integrated walker percept. In addition, the spatial distribution of the IMs could provide insights into where in the visual processing pathway spatial integration occurs (whether IM responses are localised in early visual areas or higher-level regions down the ventral pathway, for example). By manipulating the presence of knowledge-driven top-down modulation across conditions, comparisons between the localisation of IMs across conditions could also indicate where feedback signals conveying object-knowledge integrate with bottom-up processing. Furthermore, while IMs act as a neural signature of perceptual organisation and integration, it may be speculated that fundamental and harmonic responses reflect the processing of local elements. If that is the case, the amplitudes of fundamentals and harmonics are expected to show similar patterns as the psychophysically-measured perceptual sensitivity across the four conditions. For example, local features that contribute to the global percept in the G-C condition may show a higher amplitude of fundamentals and/or harmonics compared to its NoGestalt baseline control condition, whereas non-contributing local features in

the G-NC condition may yield the same level of fundamentals and harmonics as its baseline control.

If the fundamentals and harmonics in frequency-tagging paradigms are established as an index for bottom-up processing of local visual elements, then the separate neural signatures of local features and global percept can be assessed in relation to oscillations of different frequency bands known to be involved in visual processing. Bottom-up processing has been found to be associated with gamma-band oscillations, whereas top-down processing such as sensory predictions are related to alpha-band and beta-band oscillations (e.g., Arnal & Giraud, 2012; Engel & Fries, 2010; Mejias et al., 2016; Michalareas et al., 2016; Samaha et al., 2018; van Kerkoerle et al., 2014). These oscillations can be candidates for the neuronal mechanisms underlying the knowledge-driven top-down modulation in perceptual organisation. Therefore, in future frequency-tagging studies such as the one using point-light walker stimuli described above and the planned studies using Kanizsa figures and two-tone images described in Section 1.3, the magnitudes of VSSR components can be assessed in relation to the alpha-, beta- and gamma-band oscillations during the perceptual task. It is predicted that frequency-tagging response components are differentially related to oscillations in different frequency bands. For example, an increase in fundamental and harmonic power in the G-C condition of the point-light walker task may be related to an increase in alpha and/or beta oscillations, suggesting that the high-level walker percept enhances the processing of contributing local features via top-down modulations conveyed by alpha and/or beta oscillations. Overall, neuroimaging studies like those using the frequency-tagging technique can not only test whether conclusions drawn from psychophysical findings are consistent with neuronal findings but also shed light on possible neural implementations of the computational mechanisms inferred from behavioural testing.

Appendices

Appendix 1

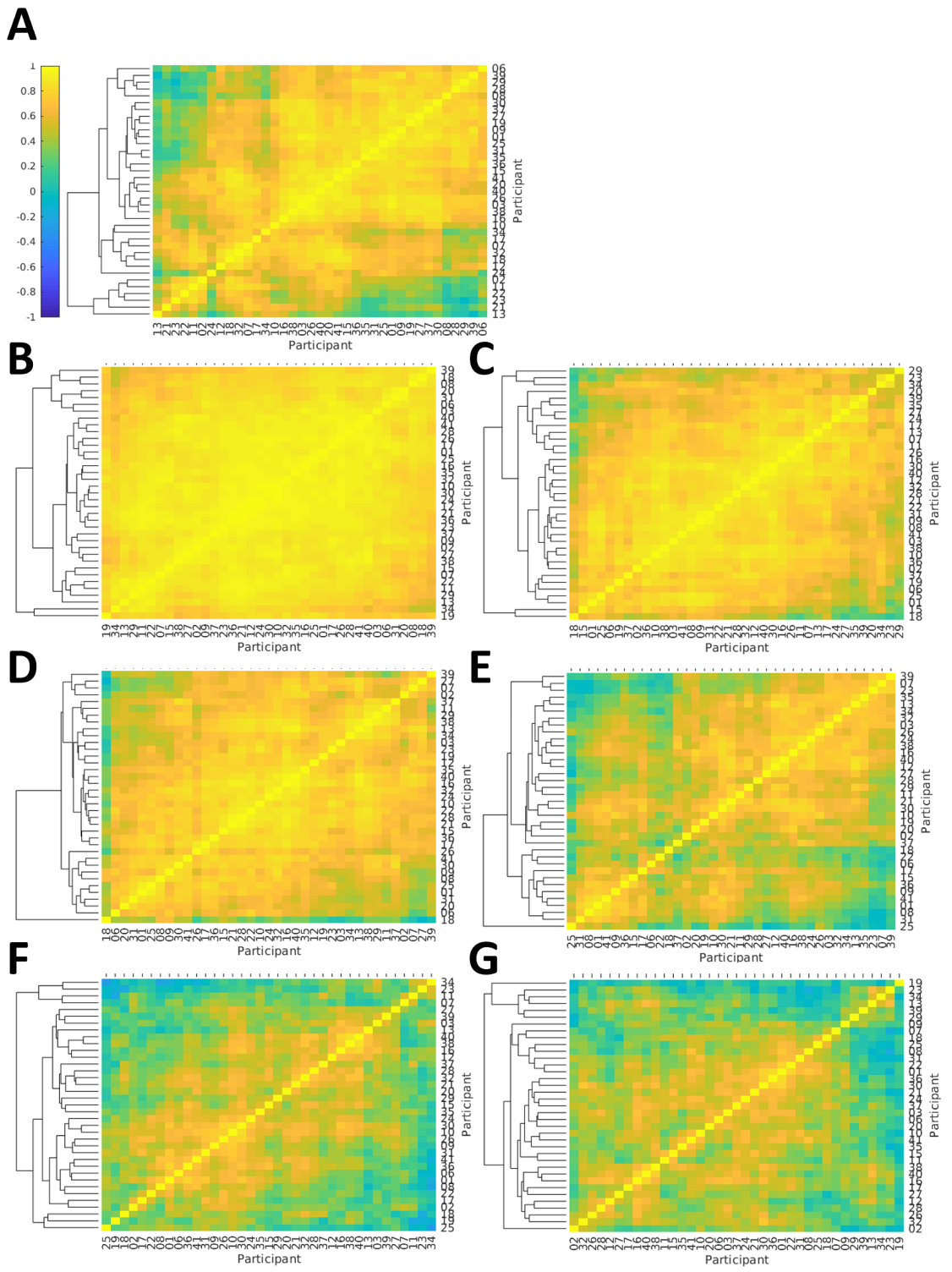

Figure 1: **Correlations across participants' visual chirp response tuning functions.**
Colours in the correlation matrices indicate Pearson's correlation coefficients between the response tuning functions of each two participants at the fundamental (A), second harmonic (B), third harmonic (C), fourth harmonic (C), fifth harmonic (C), sixth harmonic (C), and seventh harmonic (C). Hierarchical clustering analyses were conducted to group together participants with similar correlation profiles, and the resultant dendrograms are plotted next to the correlation matrices.

Appendix 2

The CFF thresholds estimated by fitting the staircase data with a psychometric function (PF) were compared to the thresholds estimated by averaging the last six reversals of the staircase. To compute the CFF threshold from staircase reversals, bad staircase runs were excluded if it met any of the following criteria: (1) the proportion of corrupted trials (where $RT < 1ms$) in the run was greater than 10%, (2) the total number of reversals in the run was fewer than eight, (3) a corrupted trial registered an incorrect response within the first five trials of the run. After applying such exclusion criteria, six participants had no good staircase runs left and thus were excluded. The remaining 31 participants had at least two good runs. The last six reversal points in each good staircase run were averaged to arrive at the CFF estimate of this run. A participant's CFF threshold was then computed as the mean of the CFF estimates of all their good staircase runs.

Figure 2 plots the CFF thresholds estimated by averaging reversals and by fitting PFs to the staircase data (as described in section 3.2.3 on page 50). Spearman's correlation analysis showed a strong positive correlation between results of the two estimation methods, $r(28) = 0.92, p = 6.21 \times 10^{-13}$. Paired-sample t-test suggested that the PF-fitting method yielded significantly higher CFF estimates (mean = 75.65, SD = 12.82) than the reversal-averaging method did (mean = 71.46, SD = 10.97), $t(29) = -4.78, p = 4.69 \times 10^{-5}$.

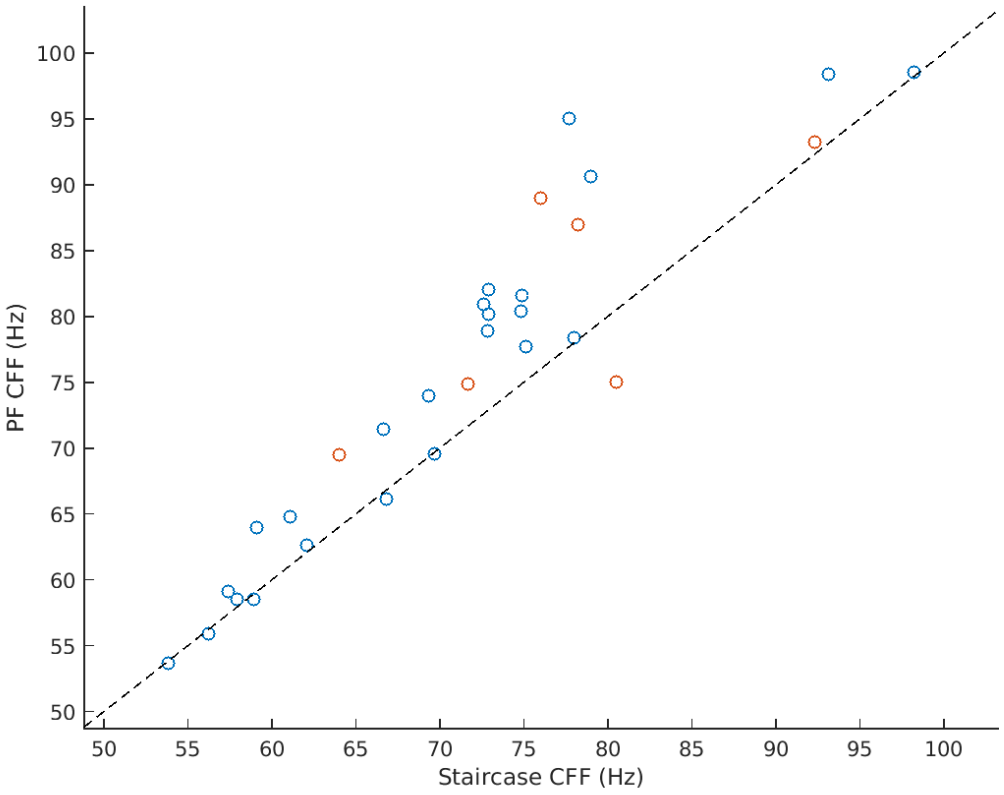

Figure 2: **Participants' CFF thresholds estimated by averaging staircase reversals and by fitting psychometric function (PF) to the staircase data.** Orange data points indicate participants whose PF fitting had a p-value smaller than 0.05 in the goodness-of-fit test, indicating poor fit. The dotted line denotes the perfect relationship between the two methods of estimating CFF.

Appendix 3

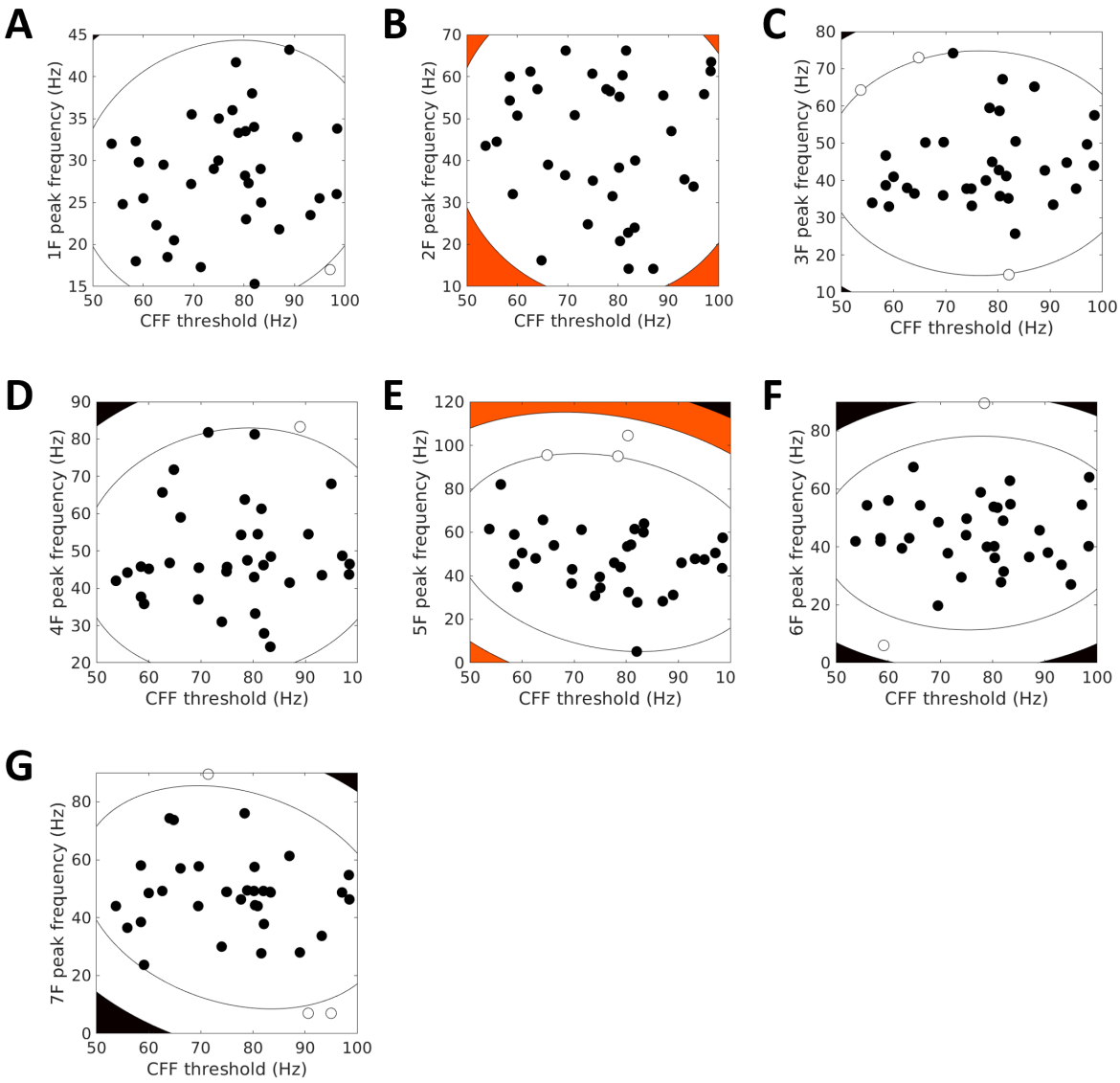

Figure 3: **Correlation between the CFF threshold and the peak frequency of chirp-evoked responses.**
Scatter plots with contour plots of the Mahalanobis lines illustrating the relationship between the CFF threshold and the peak response frequency in the visual chirp task at the fundamental (A) and the second (B), third (C), fourth (D), fifth (E), sixth (F) and seventh (G) harmonics. The contour lines and colours indicate ranges of the average bootstrapping Mahalanobis distance between each observation and the bivariate mean of all observations. Open circles indicate outlier observations excluded from the correlation analysis due to an average bootstrapping Mahalanobis distance of 6 or greater. Shepherd's pi correlations for all harmonics were non-significant, $p > .45$.

Appendix 4

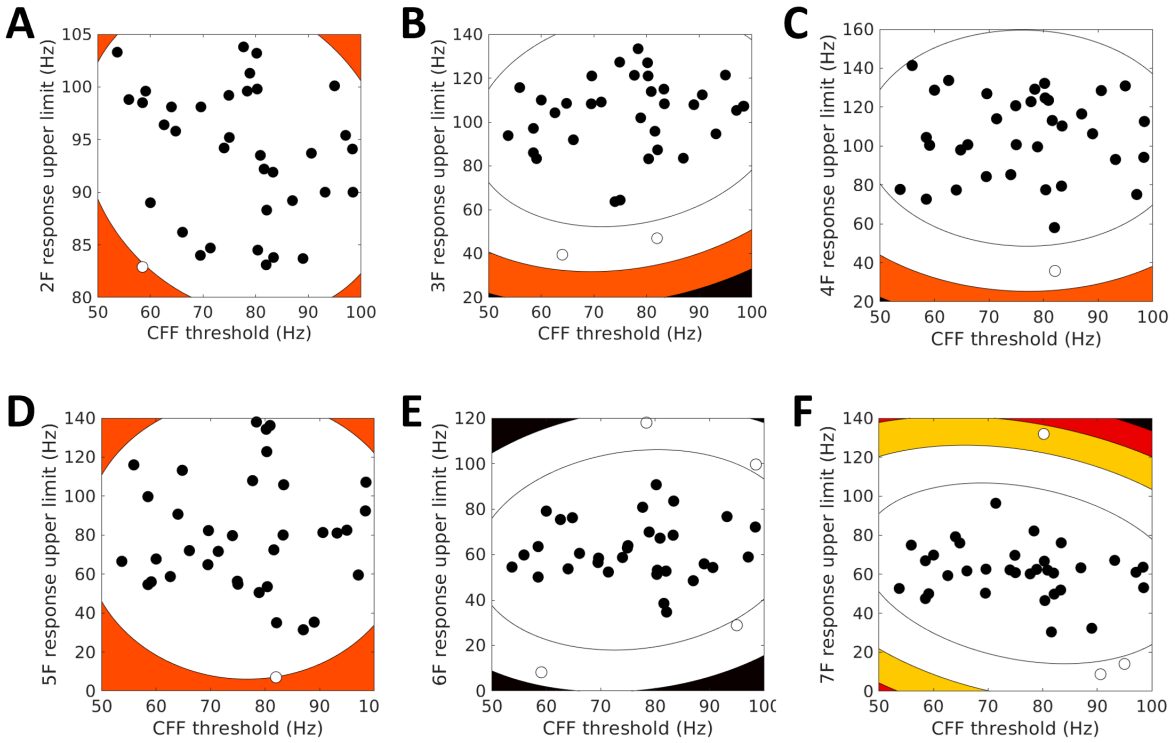

Figure 4: **Correlation between the CFF threshold and the upper limit of chirp-evoked harmonic responses.**
Scatter plots with contour plots of the Mahalanobis lines illustrating the relationship between the CFF threshold and the frequency above which the chirp-evoked response diminishes to below 15% of the peak response at the second (A), third (B), fourth (C), fifth (D), sixth (E) and seventh (F) harmonics. The contour lines and colours indicate ranges of the average bootstrapping Mahalanobis distance between each observation and the bivariate mean of all observations. Open circles indicate outlier observations excluded from the correlation analysis due to an average bootstrapping Mahalanobis distance of 6 or greater. Shepherd's pi correlations for all harmonics were non-significant, $p > .11$.

Appendix 5

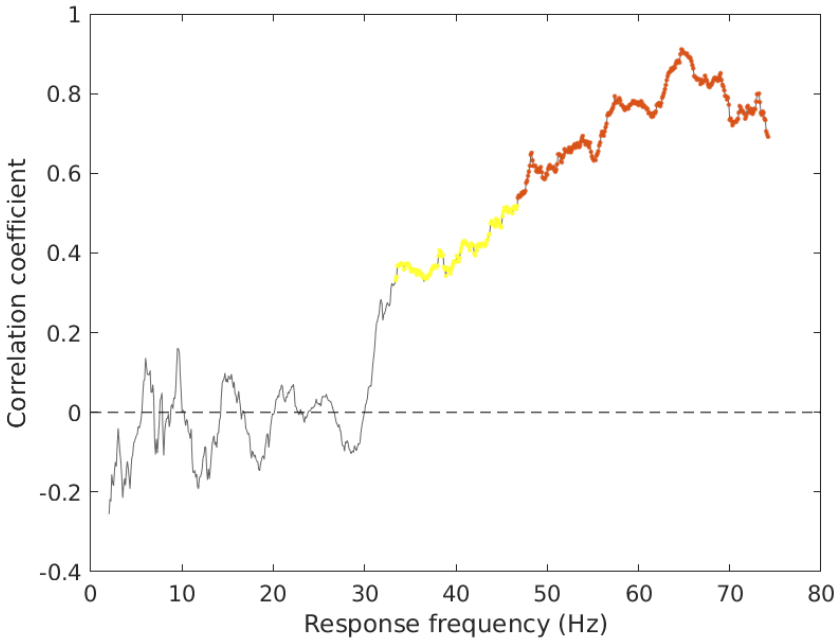

Figure 5: **Correlation between the VSSR upper limit and chirp-evoked response tuning function.**
Spearman's correlation coefficients between the upper limit of the fundamental chirp-evoked response and the temporal response tuning functions at the fundamental. Yellow dots mark correlations with $p < .05$ before correction for multiple testing. Orange dots mark significant correlations after omnibus correction.

Appendix 6

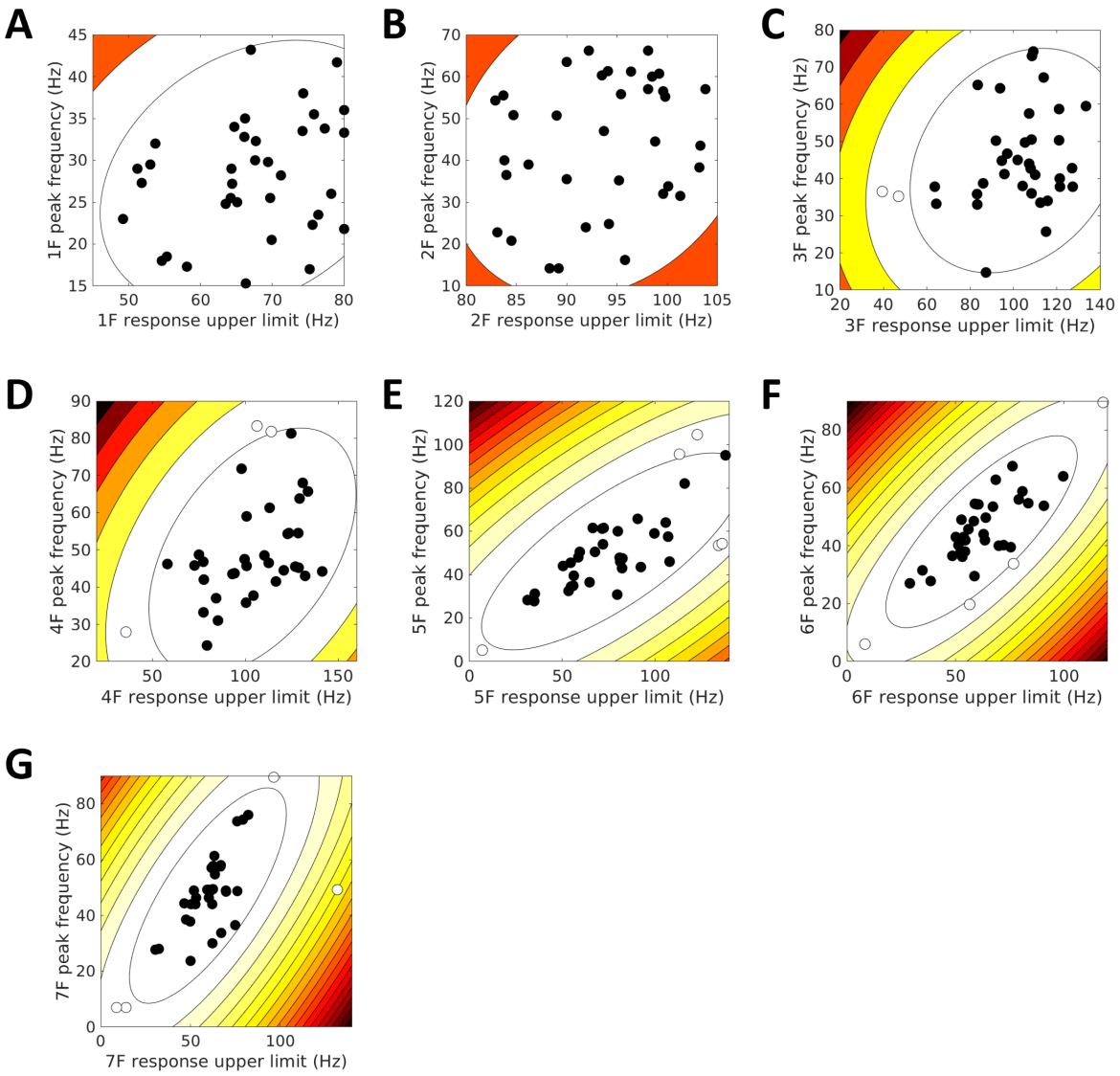

Figure 6: **Correlation between the upper limit and the peak frequency of chirp-evoked responses.**
Scatter plots with contour plots of the Mahalanobis lines illustrating the relationship between the upper limit and the peak response frequency in the visual chirp task at the fundamental (A) and the second (B), third (C), fourth (D), fifth (E), sixth (F) and seventh (G) harmonics. The contour lines and colours indicate ranges of the average bootstrapping Mahalanobis distance between each observation and the bivariate mean of all observations. Open circles indicate outlier observations excluded from the correlation analysis due to an average bootstrapping Mahalanobis distance of 6 or greater. Shepherd's pi correlations for the first four harmonics were non-significant, $p > .07$ without correction for multiple testing. There were significant positive correlations between the peak frequency and upper limit for the highest three harmonics. **(E)** $r(29) = 0.66, p = 9.53 \times 10^{-5}$, **(F)** $r(30) = 0.71, p = 1.29 \times 10^{-5}$, **(G)** $r(30) = 0.59, p = 7.30 \times 10^{-4}$ (all without correction for multiple testing).

Appendix 7

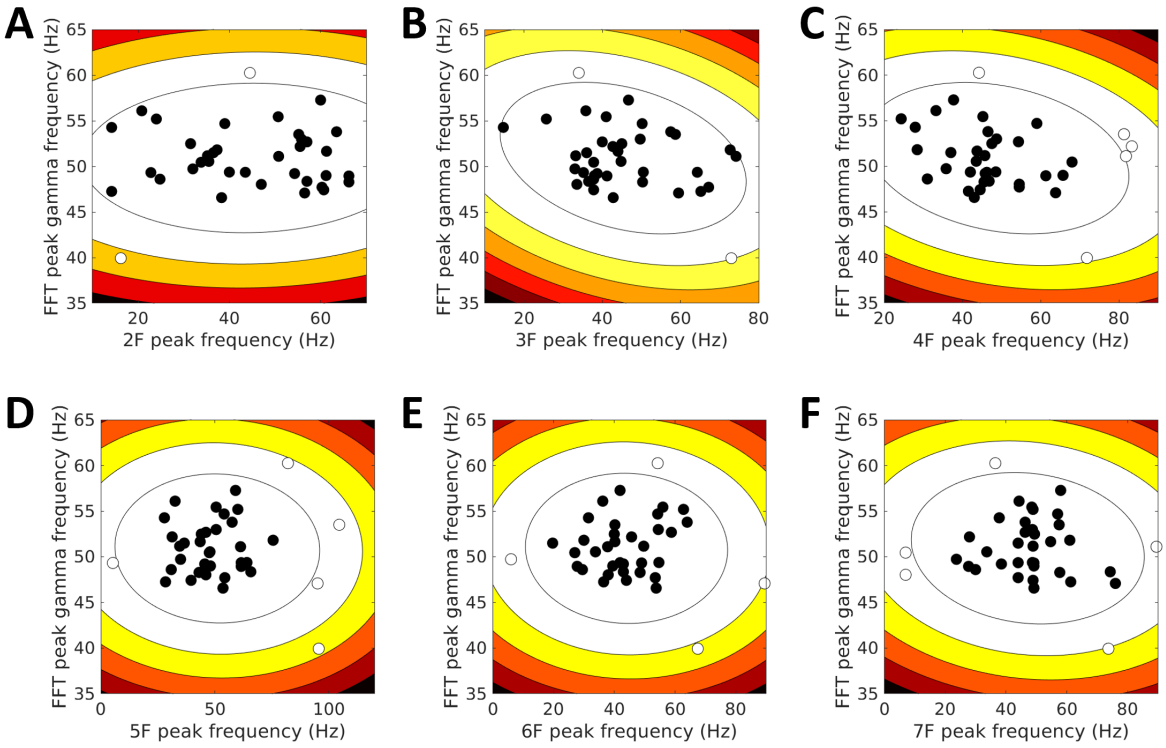

Figure 7: **Correlation between peak gamma frequency from FFT and the peak frequency of chirp-evoked harmonic responses.**
Scatter plots with contour plots of the Mahalanobis lines illustrating the relationship between the peak gamma frequency derived from the centre of mass in the FFT power spectra and the peak response frequency in the visual chirp task at the second (A), third (B), fourth (C), fifth (D), sixth (E) and seventh (F) harmonics. The contour lines and colours indicate ranges of the average bootstrapping Mahalanobis distance between each observation and the bivariate mean of all observations. Open circles indicate outlier observations excluded from the correlation analysis due to an average bootstrapping Mahalanobis distance of 6 or greater. Shepherd's pi correlations for all harmonics were non-significant, $p > .25$.

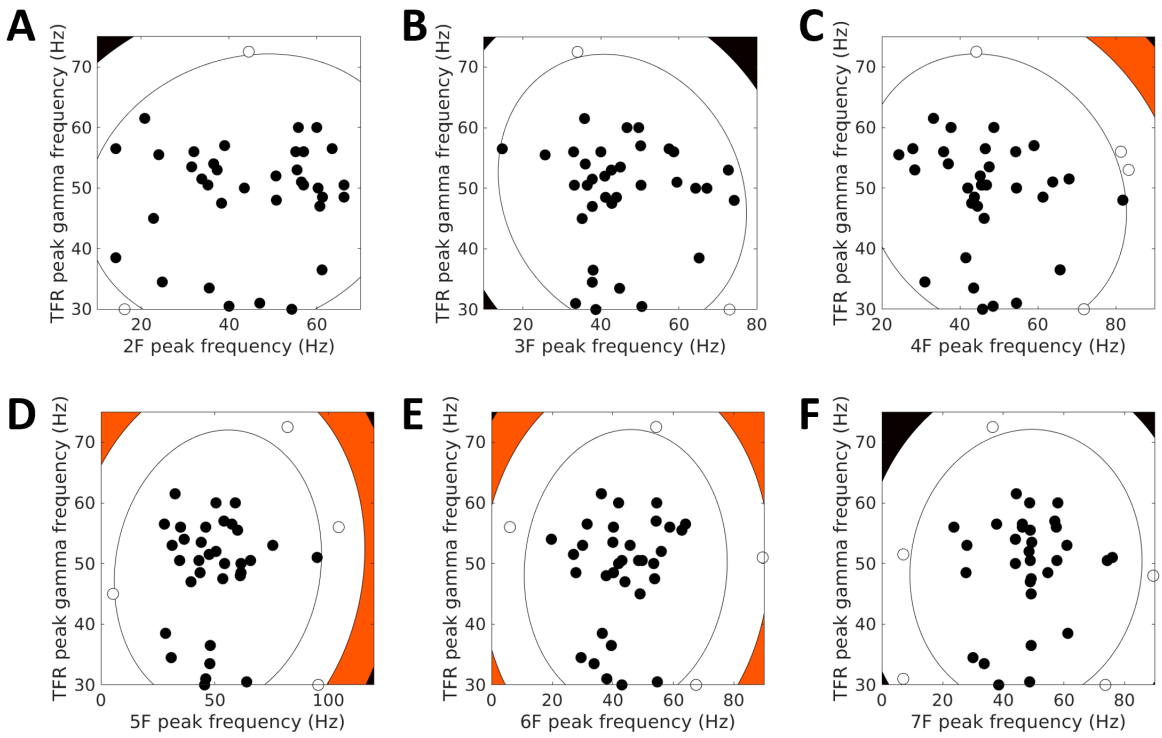

Figure 8: **Correlation between peak gamma frequency from TFR and the peak frequency of chirp-evoked harmonic responses.**
Scatter plots with contour plots of the Mahalanobis lines illustrating the relationship between the peak gamma frequency derived from time-frequency analysis TFRs and the peak response frequency in the visual chirp task at the second (A), third (B), fourth (C), fifth (D), sixth (E) and seventh (F) harmonics. The contour lines and colours indicate ranges of the average bootstrapping Mahalanobis distance between each observation and the bivariate mean of all observations. Open circles indicate outlier observations excluded from the correlation analysis due to an average bootstrapping Mahalanobis distance of 6 or greater. Shepherd's pi correlations for all harmonics were non-significant, $p > .52$.

Appendix 8

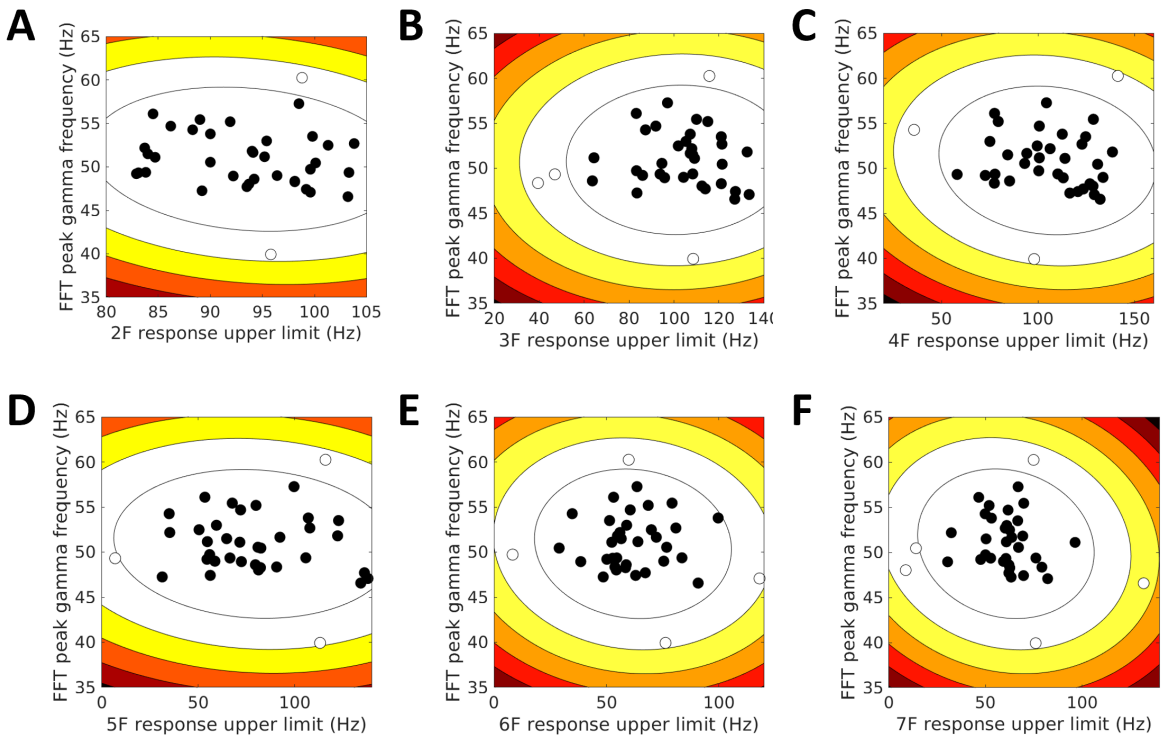

Figure 9: **Correlation between peak gamma frequency from FFT and the upper limit of chirp-evoked harmonic responses.**
Scatter plots with contour plots of the Mahalanobis lines illustrating the relationship between the peak gamma frequency derived from the centre of mass in the FFT power spectra and the frequency above which chirp-evoked responses fell below 15% of the peak response at the second (A), third (B), fourth (C), fifth (D), sixth (E) and seventh (F) harmonics. The contour lines and colours indicate ranges of the average bootstrapping Mahalanobis distance between each observation and the bivariate mean of all observations. Open circles indicate outlier observations excluded from the correlation analysis due to an average bootstrapping Mahalanobis distance of 6 or greater. Shepherd's pi correlations for all harmonics were non-significant, $p > .29$.

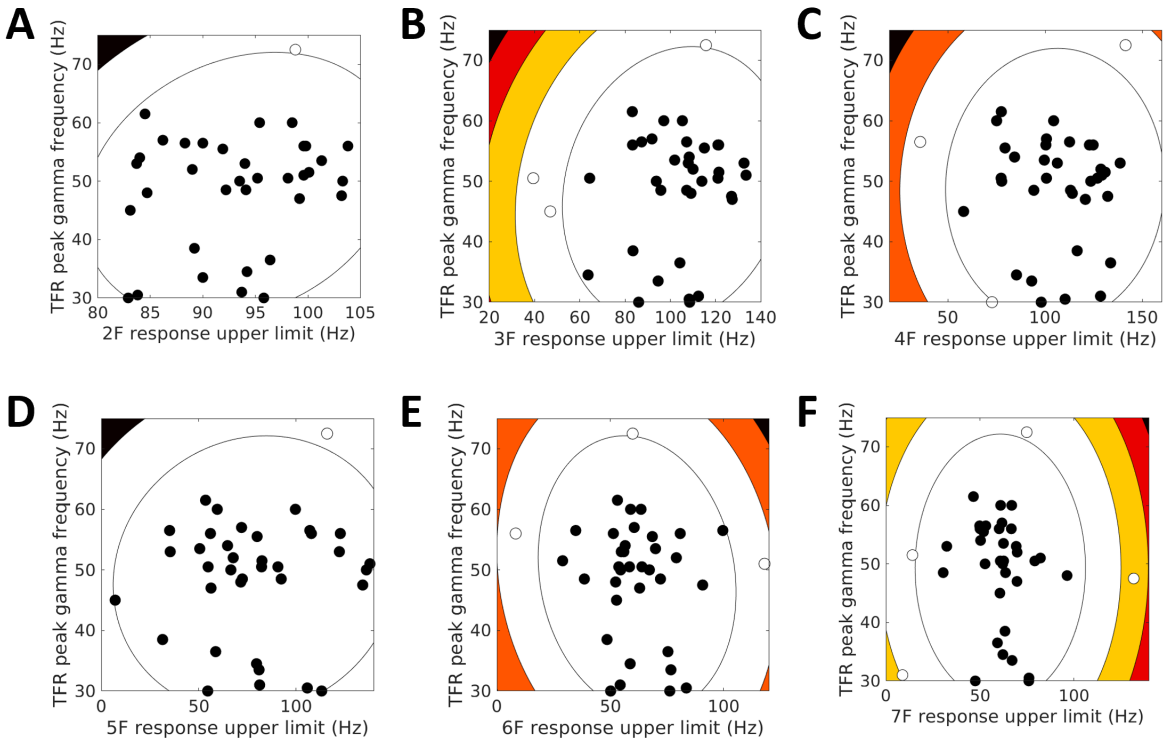

Figure 10: **Correlation between peak gamma frequency from TFR and the upper limit of chirp-evoked harmonic responses.**
Scatter plots with contour plots of the Mahalanobis lines illustrating the relationship between the peak gamma frequency derived from time-frequency analysis TFRs and the frequency above which chirp-evoked responses fell below 15% of the peak response at the second (A), third (B), fourth (C), fifth (D), sixth (E) and seventh (F) harmonics. The contour lines and colours indicate ranges of the average bootstrapping Mahalanobis distance between each observation and the bivariate mean of all observations. Open circles indicate outlier observations excluded from the correlation analysis due to an average bootstrapping Mahalanobis distance of 6 or greater. Shepherd's pi correlations for all harmonics were non-significant, $p > .17$.

Appendix 9

As illustrated in Figure 11, the response error SD was significantly smaller in the G-C condition ($Mdn = 15.04$, $M = 16.56$, $SD = 6.43$) than in the G-NC condition ($Mdn = 15.66$, $M = 18.05$, $SD = 7.78$), $Z = 47379$, $p = 2.03 \times 10^{-9}$, showing that the sensitivity for contributing local orientations was robustly better than for non-contributing local orientations. This difference could be partially explained by a collinearity effect, because the perceptual sensitivity in the NG-C control condition ($Mdn = 15.10$, $M = 17.04$, $SD = 6.88$) was better than that in the NG-NC control condition ($Mdn = 15.87$, $M = 18.00$, $SD = 7.47$), $Z = 52229$, $p = 4.55 \times 10^{-6}$. However, the difference between the two NoGestalt conditions ($Mdn = 0.78$, $M = 0.95$, $SD = 4.50$) was significantly smaller than the difference between the two Gestalt conditions ($Mdn = 0.94$, $M = 1.49$, $SD = 5.31$), $Z = 74233$, $p = .035$, showing that the sensitivity difference between contributing and non-contributing local orientations was at least partly due to differential top-down modulations from the high-level representation.

As illustrated in Figure 12, the response error SD in the G-C condition ($Mdn = 15.04$, $M = 16.56$, $SD = 6.43$) was significantly smaller than in the NG-C condition ($Mdn = 15.10$, $M = 17.04$, $SD = 6.88$), $Z = 59402$, $p = .012$, indicating enhanced orientation sensitivity when local orientations contributed to the global percept than when there was no global percept. On the other hand, the response error IQR in the G-NC condition ($Mdn = 15.66$, $M = 18.05$, $SD = 7.78$) did not differ from that in the NG-NC control condition ($Mdn = 15.87$, $M = 18.00$, $SD = 7.47$), $Z = 65697$, $p = .505$, suggesting no suppression in the sensitivity to non-contributing local orientations compared to when there was no top-down modulation from a global percept.

Individual differences analyses using Spearman's correlations found a significant correlation between individuals' baseline orientation sensitivity and the extent of differential top-down modulation between contributing and non-contributing local orientations, $r(519) = 0.16$, $p = 2.88 \times 10^{-4}$ (as illustrated in Figure 13). The baseline perceptual sensitivity was also significantly related to the extent of sensitivity enhancement for local orientations that contributed to the global percept, $r(519) = 0.13$, $p = .003$ (see Figure 14). The extents of perceptual enhancement for contributing local features and perceptual suppression for non-contributing features were not related, $p = .481$ (as seen in Figure 15).

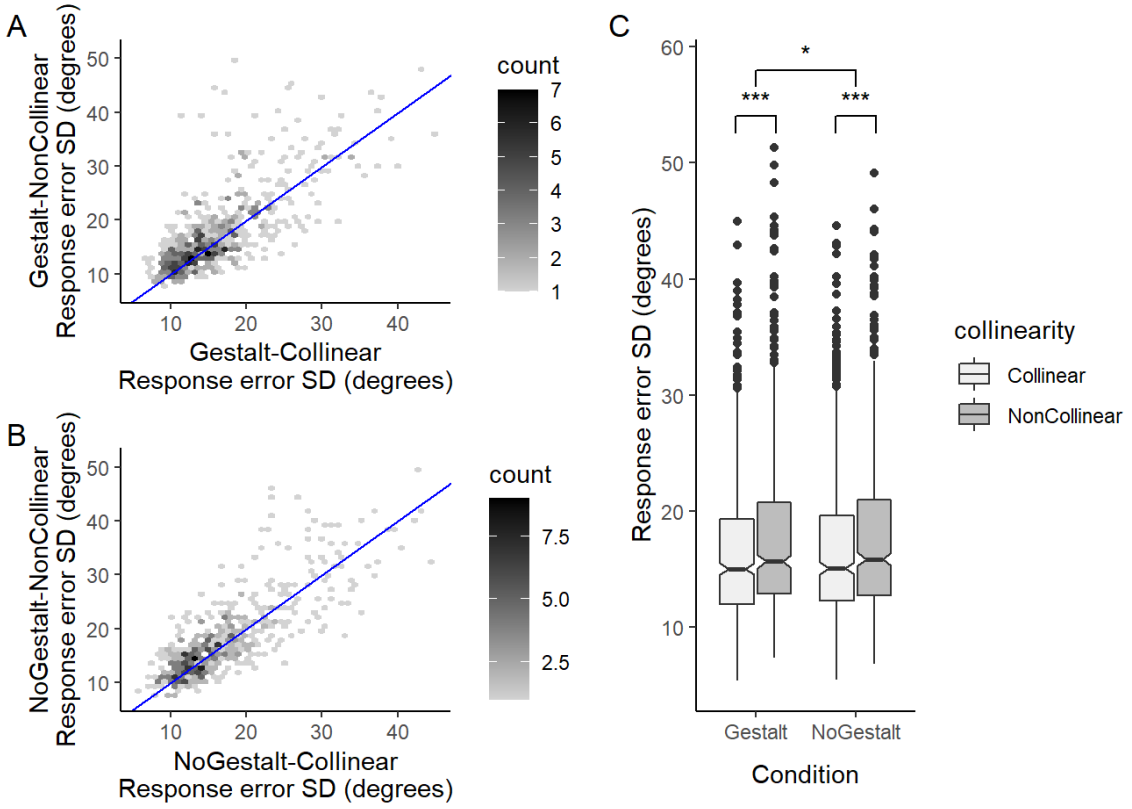

Figure 11: **Comparisons of perceptual sensitivity between the two Gestalt conditions and between the two NoGestalt conditions.**
In the hexagonal heatmaps illustrating the relationship between the two Gestalt conditions **(A)** and between the two NoGestalt conditions **(B)**, the greyscale colour indicates the density of data points in each hexagonal bin. The blue line indicates equal response error SD in the two plotted conditions. The larger the response error SD, the lower the perceptual sensitivity; thus more data above the blue line suggests that most participants' perceptual sensitivity was worse in the NonCollinear condition than in the Collinear condition. **(C)** The perceptual sensitivity was significantly better in the Collinear stimuli than in the NonCollinear stimuli for both Gestalt and NoGestalt conditions, but this difference was larger between Gestalt conditions than between NoGestalt conditions. $^{*}p < .05$, $^{***}p < .001$.

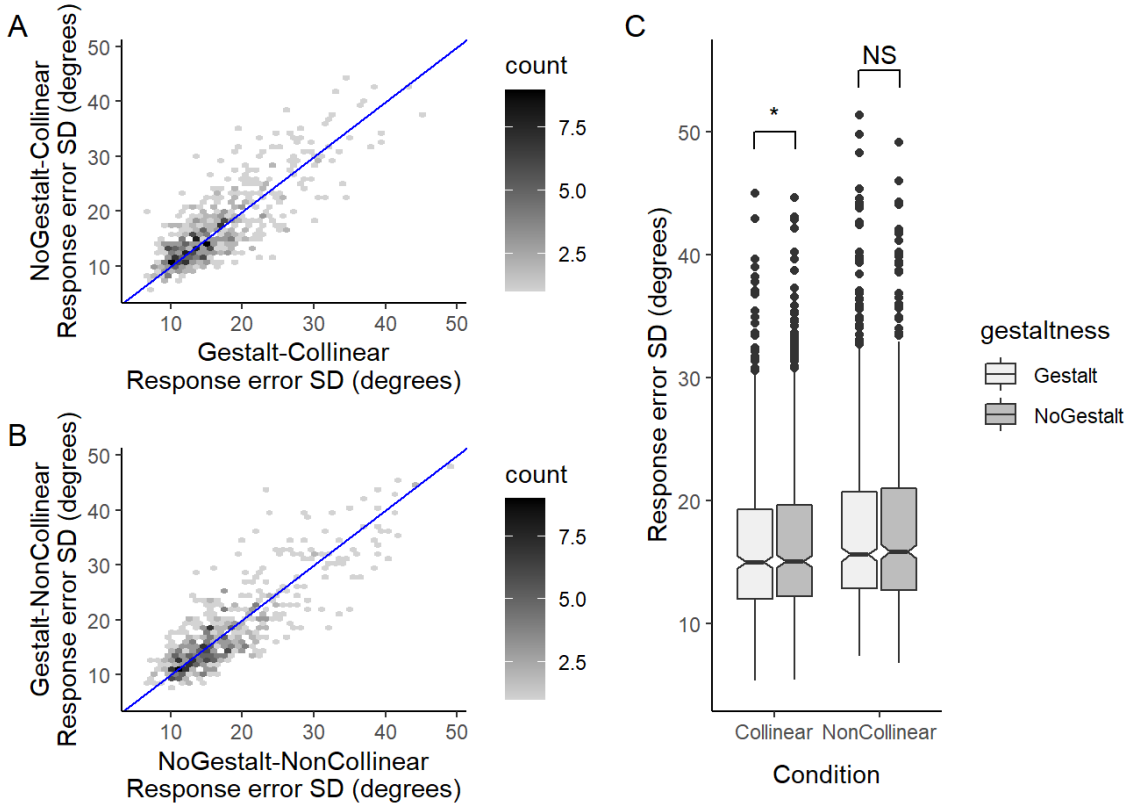

Figure 12: **Comparisons of perceptual sensitivity between the two Collinear conditions and between the two NonCollinear conditions.**
Same convention as for Figure 11 applies to this figure. More data above the blue line in **(A)** indicates most participants showed enhanced sensitivity to contributing local orientations compared to the baseline. This enhancement was significant, as illustrated by the comparison on the left in **(C)**, $^*p < .05$. More data above the blue line in **(B)** would suggest suppressed sensitivity to non-contributing local orientations compared to the baseline, but this comparison was non-significant, as indicated by the comparison on the right in **(C)**, ns $p > .05$.

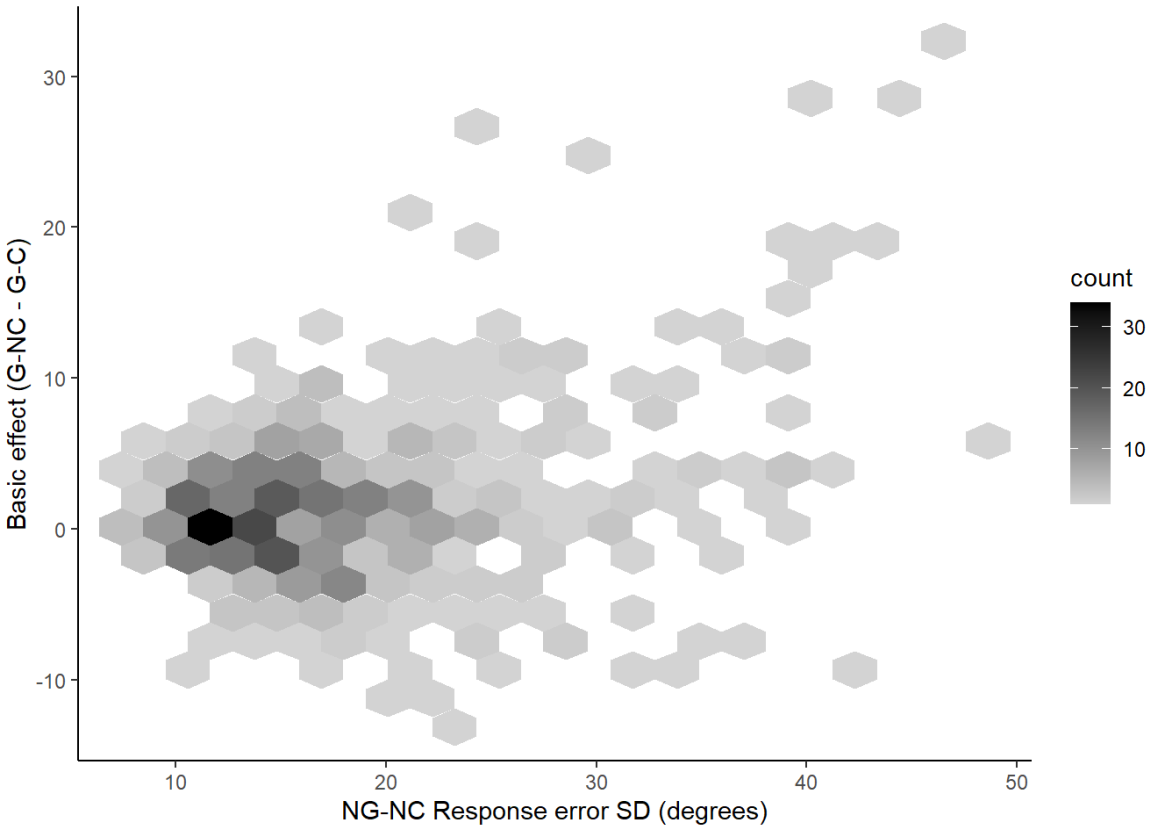

Figure 13: **Relationship between observers' baseline orientation sensitivity and their extent of differential modulations for contributing and non-contributing orientations.**
The baseline perceptual sensitivity is indexed by the response error SD (degrees) in the NG-NC condition. The smaller the value, the higher the orientation sensitivity. The extent of the differential top-down modulations is quantified as the size of the basic effect, i.e., the response error SD in the G-NC condition minus that in the G-C condition.

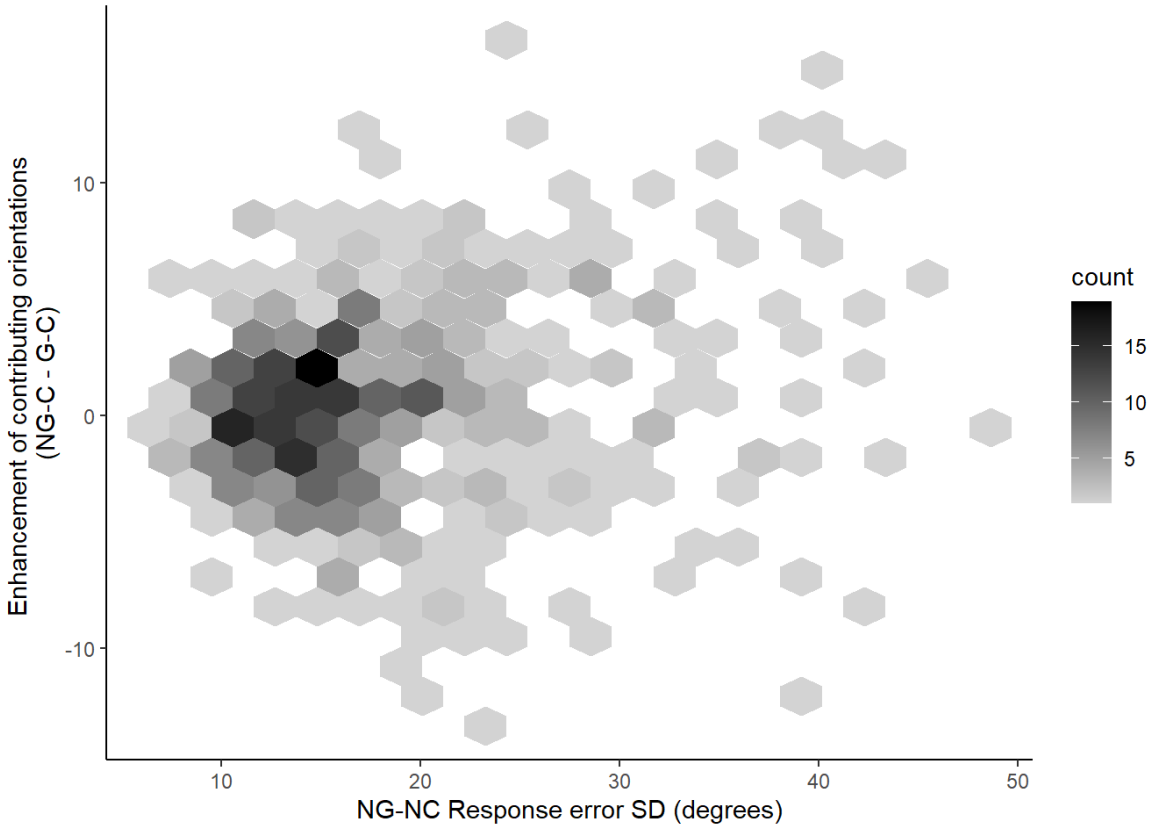

Figure 14: **Relationship between observers' baseline orientation sensitivity and sensitivity enhancement for contributing local orientations.**
The baseline perceptual sensitivity is indexed by the response error SD (degrees) in the NG-NC condition. The smaller the value, the higher the orientation sensitivity. The extent of the sensitivity enhancement was quantified as the response error SD in the NG-C condition minus that in the G-C condition.

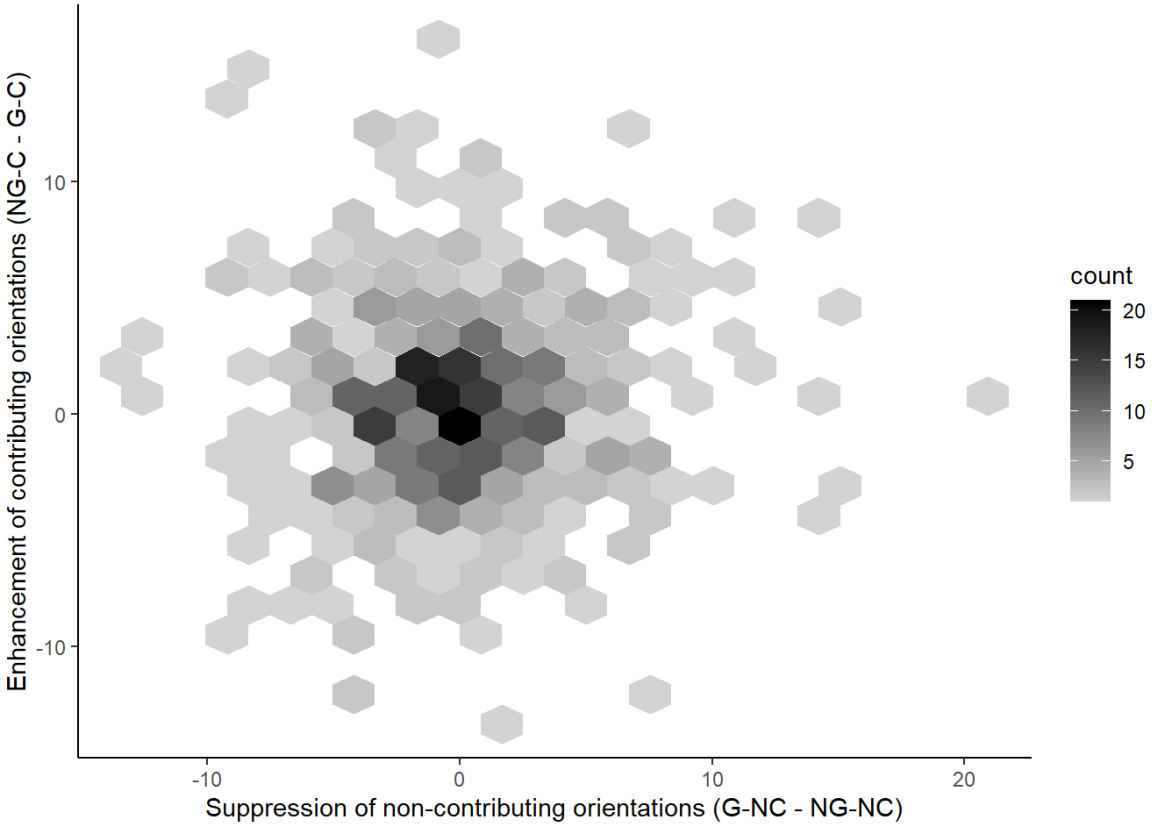

Figure 15: **Relationship between observers' sensitivity enhancement for contributing local orientations and sensitivity suppression for non-contributing local orientations.**

Bibliography

Adaikkan, C., Middleton, S. J., Marco, A., Pao, P. C., Mathys, H., Kim, D. N. W., Gao, F., Young, J. Z., Suk, H. J., Boyden, E. S., McHugh, T. J., & Tsai, L. H. (2019). Gamma Entrainment Binds Higher-Order Brain Regions and Offers Neuroprotection. *Neuron*, *102*(5), 929–943. https://doi.org/10.1016/J.NEURON.2019.04.011

Adjamian, P., Holliday, I. E., Barnes, G. R., Hillebrand, A., Hadjipapas, A., & Singh, K. D. (2004). Induced visual illusions and gamma oscillations in human primary visual cortex. *European Journal of Neuroscience*, *20*(2), 587–592. https://doi.org/10.1111/J.1460-9568.2004.03495.X

Adrian, E. D., & Matthews, B. H. (1934). The berger rhythm: Potential changes from the occipital lobes in man. *Brain*, *57*(4), 355–385. https://doi.org/10.1093/brain/57.4.355

Aissani, C., Cottereau, B., Dumas, G., Paradis, A. L., & Lorenceau, J. (2011). Magnetoencephalographic signatures of visual form and motion binding. *Brain Research*, *1408*, 27–40. https://doi.org/10.1016/j.brainres.2011.05.051

Aitchison, L., & Lengyel, M. (2017). With or without you: predictive coding and Bayesian inference in the brain. *Current Opinion in Neurobiology*, *46*, 219–227. https://doi.org/10.1016/j.conb.2017.08.010

Alais, D., Locke, S. M., Leung, J., & Van Der Burg, E. (2016). No attentional capture from invisible flicker. *Scientific Reports*, *6*(1), 29296. https://doi.org/10.1038/srep29296

Allen, C. (2019). The relationship between the temporal structure of magnetoencephalography recorded brain activity and capacity to form discrete auditory representations. *European Journal of Neuroscience*, *49*(12), 1564–1574. https://doi.org/10.1111/ejn.14289

Alp, N., Kogo, N., Van Belle, G., Wagemans, J., & Rossion, B. (2016). Frequency tagging yields an objective neural signature of Gestalt formation. *Brain and Cognition*, *104*, 15–24. https://doi.org/10.1016/j.bandc.2016.01.008

Arnal, L. H., & Giraud, A. L. (2012). Cortical oscillations and sensory predictions. https://doi.org/10.1016/j.tics.2012.05.003

Bakardjian, H., Tanaka, T., & Cichocki, A. (2010). Optimization of SSVEP brain responses with application to eight-command Brain-Computer Interface. *Neuroscience Letters*, *469*(1), 34–38. https://doi.org/10.1016/j.neulet.2009.11.039

Barlow, H. B. (1958). Temporal and spatial summation in human vision at different background intensities. *The Journal of physiology*, *141*(2), 337–350.

Bastos, A. M., Vezoli, J., Bosman, C. A., Schoffelen, J.-M., Oostenveld, R., Dowdall, J. R., De Weerd, P., Kennedy, H., & Fries, P. (2015). Visual Areas Exert Feedforward and Feedback Influences through Distinct Frequency Channels. *Neuron*, *85*(2), 390–401. https://doi.org/10.1016/J.NEURON.2014.12.018

Baumgarten, T. J., Neugebauer, J., Oeltzschner, G., Füllenbach, N. D., Kircheis, G., Häussinger, D., Lange, J., Wittsack, H. J., Butz, M., & Schnitzler, A. (2018). Connecting occipital alpha band peak frequency, visual temporal resolution, and occipital GABA levels in healthy participants and hepatic encephalopathy patients. *NeuroImage: Clinical*, *20*, 347–356. https://doi.org/10.1016/j.nicl.2018.08.013

Bayram, A., Bayraktaroglu, Z., Karahan, E., Erdogan, B., Bilgic, B., Özker, M., Kasikci, I., Duru, A. D., Ademoglu, A., Öztürk, C., Arikan, K., Tarhan, N., & Demiralp, T. (2011). Simultaneous EEG/fMRI analysis of the resonance phenomena in steady-state visual evoked responses. *Clinical EEG and Neuroscience*, *42*(2), 98–106. https://doi.org/10.1177/155005941104200210/ASSET/IMAGES/LARGE/10.1177{_}155005941104200210-FIG2.JPEG

Bieger, J., & Garcia-Molina, G. (2010). *Light Stimulation Properties to Influence Brain Activity: A Brain-Computer Interface Application* (tech. rep.). https://www.researchgate.net/publication/254761409

Börgers, C. (2017). The PING model of gamma rhythms. *An introduction to modeling neuronal dynamics* (pp. 255–267). Springer, Cham. https://doi.org/10.1007/978-3-319-51171-9{_}30

Börgers, C., & Kopell, N. (2003). Synchronization in networks of excitatory and inhibitory neurons with sparse, random connectivity. *Neural Computation*, *15*(3), 509–538. https://doi.org/10.1162/089976603321192059

Brainard, D. H. (1997). The Psychophsycis Toolbox. *Spatial Vision*, *10*(4), 433–436. https://doi.org/10.1017/CBO9781107415324.004

Brenton, R. S., Thompson, H. S., & Maxner, C. (1989). Critical flicker frequency: a new look at an old test. *New methods of sensory visual testing* (pp. 29–52). Springer.

Brown, A., Corner, M., Crewther, D. P., & Crewther, S. G. (2018). Human Flicker Fusion Correlates With Physiological Measures of Magnocellular Neural Efficiency. *Frontiers in Human Neuroscience*, *12*, 176. https://doi.org/10.3389/fnhum.2018.00176

Burns, S. A., Elsner, A. E., & Kreitz, M. R. (1992). Analysis of nonlinearities in the flicker ERG. *Optometry and vision science*, *69*(2), 95–105.

Burr, D. C. (1981). Temporal summation of moving images by the human visual system. *Proceedings of the Royal Society of London. Series B. Biological Sciences*, *211*, 321–339. https://royalsocietypublishing.org/

Butz, M., May, E. S., Häussinger, D., & Schnitzler, A. (2013). The slowed brain: Cortical oscillatory activity in hepatic encephalopathy. https://doi.org/10.1016/j.abb.2013.04.004

Cao, D., Lee, B. B., & Sun, H. (2010). Combination of rod and cone inputs in parasol ganglion cells of the magnocellular pathway. *Journal of Vision*, *10*(11). https://doi.org/10.1167/10.11.4

Capilla, A., Pazo-Alvarez, P., Darriba, A., Campo, P., & Gross, J. (2011). Steady-state visual evoked potentials can be explained by temporal superposition of transient event-related responses. *PLoS ONE*, *6*(1). https://doi.org/10.1371/journal.pone.0014543

Chai, Y., Handwerker, D. A., Marrett, S., Gonzalez-Castillo, J., Merriam, E. P., Hall, A., Molfese, P. J., & Bandettini, P. A. (2019). Visual temporal frequency preference shows a distinct cortical architecture using fMRI. *NeuroImage*, *197*, 13–23. https://doi.org/10.1016/j.neuroimage.2019.04.048

Chen, X., Wang, Y., Zhang, S., Xu, S., & Gao, X. (2019). Effects of stimulation frequency and stimulation waveform on steady-state visual evoked potentials using a computer monitor. *Journal of Neural Engineering*, *16*(6). https://doi.org/10.1088/1741-2552/ab2b7d

Christensen, J. H., Bex, P. J., & Fiser, J. (2019). Coding of low-level position and orientation information in human naturalistic vision (C. R. Fetsch, Ed.). *PLoS ONE*, *14*(2), e0212141. https://doi.org/10.1371/journal.pone.0212141

Christensen, J. H., Bex, P. J., & Fiser, J. (2015). Prior implicit knowledge shapes human threshold for orientation noise. *Journal of Vision*, *15*(9), 24–24. https://doi.org/10.1167/15.9.24

Coll, M.-p., Whelan, E., & Catmur, C. (2020). Autistic traits are associated with atypical precision-weighted integration of top-down and bottom-up neural signals. *Cognition*, *199*(February). https://doi.org/10.1016/j.cognition.2020.104236

Corbetta, M., & Shulman, G. L. (2002). Control of Goal-Directed and Stimulus-Driven Attention in the Brain. *Nature Reviews Neuroscience*, *3*(3), 215–229. https://doi.org/10.1038/nrn755

Crick, F., & Koch, C. (1995). Are we aware of neural activity in primary visual cortex? *Nature*, *375*(6527), 121–123.

da Silva Castanheira, J., Orozco Perez, H. D., Misic, B., & Baillet, S. (2021). Brief segments of neurophysiological activity enable individual differentiation. *Nature Communications*, *12*(1). https://doi.org/10.1038/s41467-021-25895-8

Davis, J., Hsieh, Y. H., & Lee, H. C. (2015). Humans perceive flicker artifacts at 500 Hz. *Scientific Reports*, *5*(1), 7861. https://doi.org/10.1038/srep07861

de Lange, F. P., Heilbron, M., & Kok, P. (2018). How Do Expectations Shape Perception? *Trends in Cognitive Sciences*, *22*(9), 764–779. https://doi.org/10.1016/j.tics.2018.06.002

de Leeuw, J. R. (2015). jsPsych: A JavaScript library for creating behavioral experiments in a Web browser. *Behavior Research Methods*, *47*(1), 1–12. https://doi.org/10.3758/s13428-014-0458-y

Donner, K. (2021). Temporal vision: Measures, mechanisms and meaning. *Journal of Experimental Biology*, *224*(15). https://doi.org/10.1242/JEB.222679/271103

Eisen-Enosh, A., Farah, N., Burgansky-Eliash, Z., Polat, U., & Mandel, Y. (2017). Evaluation of Critical Flicker-Fusion Frequency Measurement Methods for the Investigation of Visual Temporal Resolution. *Scientific Reports*, *7*(1), 15621. https://doi.org/10.1038/s41598-017-15034-z

Engel, A. K., & Fries, P. (2010). Beta-band oscillations-signalling the status quo? https://doi.org/10.1016/j.conb.2010.02.015

Fawcett, I. P., Barnes, G. R., Hillebrand, A., & Singh, K. D. (2004). The temporal frequency tuning of human visual cortex investigated using synthetic aperture magnetometry. *NeuroImage*, *21*(4), 1542–1553. https://doi.org/10.1016/j.neuroimage.2003.10.045

Fedotchev, A. I., Bondar, A. T., & Konovalov, V. F. (1990). Stability of resonance EEG reactions to flickering light in humans. *International Journal of Psychophysiology*, *9*(2), 189–193. https://doi.org/10.1016/0167-8760(90)90073-M

Fernandez-alonso, M., Kaspiris-rousellis, C., Innes, W., & Read, J. C. A. (2019). Assessment of Psychophysical Methods for Measuring the Critical Flicker Fusion Frequency in Yes/No Tasks. *European Light Field Imaging Workshop (ELFI 2019)*.

Floriano, A., Carmona, V. L., Diez, P. F., & Bastos-Filho, T. F. (2019). A study of SSVEP from below-the-hairline areas in low-, medium-, and high-frequency ranges. *Research on Biomedical Engineering*, 1–6. https://doi.org/10.1007/s42600-019-00005-2

Frisby, J. P., & Stone, J. V. (2010). *Seeing: The computational approach to biological vision* (2nd). The MIT Press.

Friston, K. (2010). The free-energy principle: A unified brain theory? *Nature Reviews Neuroscience*, *11*(2), 127–138. https://doi.org/10.1038/nrn2787

Gilbert, C. D., & Li, W. (2013). Top-down influences on visual processing. https://doi.org/10.1038/nrn3476

González-García, C., & He, B. J. (2021). A Gradient of Sharpening Effects by Perceptual Prior across the Human Cortical Hierarchy. *The Journal of Neuroscience*, *41*(1), 167–178. https://doi.org/10.1523/jneurosci.2023-20.2020

Goodale, M., & Milner, A. (1992). Separate visual pathways for perception and action. *Trends in Neurosciences*, *15*(1), 20–25. https://doi.org/10.1016/0166-2236(92)90344-8

Gordon, N., Hohwy, J., Davidson, M. J., van Boxtel, J. J., & Tsuchiya, N. (2019). From intermodulation components to visual perception and cognition-a review. https://doi.org/10.1016/j.neuroimage.2019.06.008

Gordon, N., Koenig-Robert, R., Tsuchiya, N., Van Boxtel, J. J., & Hohwy, J. (2017). Neural markers of predictive coding under perceptual uncertainty revealed with hierarchical frequency tagging. *eLife*, *6*. https://doi.org/10.7554/eLife.22749

Griskova, I., Morup, M., Parnas, J., Ruksenas, O., & Arnfred, S. M. (2007). The amplitude and phase precision of 40 Hz auditory steady-state response depend on the level of arousal. *Experimental Brain Research*, *183*(1), 133–138. https://doi.org/10.1007/S00221-007-1111-0/FIGURES/2

Gulbinaite, R., Roozendaal, D. H. M., & VanRullen, R. (2019). Attention differentially modulates the amplitude of resonance frequencies in the visual cortex. *NeuroImage*, 518779. https://doi.org/10.1101/518779

Gundlach, C., & Müller, M. M. (2013). Perception of illusory contours forms intermodulation responses of steady state visual evoked potentials as a neural signature of spatial integration. *Biological Psychology*, *94*(1), 55–60. https://doi.org/10.1016/j.biopsycho.2013.04.014

Hammond, B. R., & Wooten, B. R. (2005). CFF thresholds: relation to macular pigment optical density. *Ophthalmic and Physiological Optics*, *25*(4), 315–319.

Han, C., Shapley, R., & Xing, D. (2021). Gamma rhythms in the visual cortex: functions and mechanisms. https://doi.org/10.1007/s11571-021-09767-x

Hartmann, E., Lachenmayr, B., & Brettel, H. (1979). The peripheral critical flicker frequency. *Vision Research*, *19*(9), 1019–1023.

Häussinger, D., Dhiman, R. K., Felipo, V., Görg, B., Jalan, R., Kircheis, G., Merli, M., Montagnese, S., Romero-Gomez, M., Schnitzler, A., Taylor-Robinson, S. D., & Vilstrup, H. (2022). Hepatic encephalopathy. *Nature Reviews Disease Primers*, *8*(1), 43. https://doi.org/10.1038/s41572-022-00366-6

Hecht, S., & Verrijp, C. D. (1933). The influence of intensity, color and retinal location on the fusion frequency of intermittent illumination. *Proceedings of the National Academy of Sciences*, *19*(5), 522–535. https://www.pnas.org

Heinrich, S. P. (2010). Some thoughts on the interpretation of steady-state evoked potentials. *Documenta Ophthalmologica*, *120*(3), 205–214. https://doi.org/10.1007/S10633-010-9212-7/FIGURES/4

Heinrichs-Graham, E., & Wilson, T. W. (2012). Presence of strong harmonics during visual entrainment: A magnetoencephalography study. *Biological Psychology*, *91*(1), 59–64. https://doi.org/10.1016/j.biopsycho.2012.04.008

Herbst, S. K., Javadi, A. H., van der Meer, E., & Busch, N. A. (2013). How Long Depends on How Fast—Perceived Flicker Dilates Subjective Duration. *PLOS ONE*, *8*(10), e76074. https://doi.org/10.1371/JOURNAL.PONE.0076074

Herrmann, C. S. (2001). Human EEG responses to 1-100 Hz flicker: Resonance phenomena in visual cortex and their potential correlation to cognitive phenomena. *Experimental Brain Research*, *137*(3-4), 346–353. https://doi.org/10.1007/s002210100682

Holliday, I. E., Barnes, G. R., Hillebrand, A., & Singh, K. D. (2003). Accuracy and applications of group MEG studies using cortical source locations estimated from participants' scalp surfaces. *Human Brain Mapping*, *20*(3), 142–147. https://doi.org/10.1002/HBM.10133

Hong, J., & Qin, X. (2021). Signal processing algorithms for SSVEP-based brain computer interface: State-of-the-art and recent developments. *Journal of Intelligent & Fuzzy Systems*, *40*(6), 10559–10573. https://doi.org/10.3233/JIFS-201280

Hoogenboom, N., Schoffelen, J. M., Oostenveld, R., Parkes, L. M., & Fries, P. (2006). Localizing human visual gamma-band activity in frequency, time and space. *NeuroImage*, *29*(3), 764–773. https://doi.org/10.1016/J.NEUROIMAGE.2005.08.043

Hou, C., Pettet, M. W., Sampath, V., Candy, T. R., & Norcia, A. M. (2003). Development of the spatial organization and dynamics of lateral interactions in the human visual system. *The Journal of neuroscience : the official journal of the Society for Neuroscience*, *23*(25), 8630–8640. https://doi.org/23/25/8630[pii]ET-2003/09/26

Iaccarino, H. F., Singer, A. C., Martorell, A. J., Rudenko, A., Gao, F., Gillingham, T. Z., Mathys, H., Seo, J., Kritskiy, O., Abdurrob, F., Adaikkan, C., Canter, R. G., Rueda, R., Brown, E. N., Boyden, E. S., & Tsai, L. H. (2016). Gamma frequency entrainment attenuates amyloid load and modifies microglia. *Nature*, *540*(7632), 230–235. https://doi.org/10.1038/nature20587

Jensen, O., Bonnefond, M., Marshall, T. R., & Tiesinga, P. (2015). Oscillatory mechanisms of feedforward and feedback visual processing. *Trends in Neurosciences*, *38*(4), 192–194. https://doi.org/10.1016/j.tins.2015.02.006

Jia, D., Dai, H., Takashima, Y., Nishio, T., Hirobayashi, K., Hasegawa, M., Hirobayashi, S., & Misawa, T. (2019). EEG Processing in Internet of Medical Things Using Non-Harmonic Analysis: Application and Evolution for SSVEP Responses. *IEEE Access*, *7*, 11318–11327. https://doi.org/10.1109/ACCESS.2019.2892188

Jia, D., Takashima, Y., Hasegawa, M., Hirobayashi, S., & Misawa, T. (2017). Application to SSVEP of chirp stimulus using non-harmonic analysis. *Proceedings of 2017 International Conference on Progress in Informatics and Computing, PIC 2017*, 379–383. https://doi.org/10.1109/PIC.2017.8359576

Jia, J., Liu, L., Fang, F., & Luo, H. (2017). Sequential sampling of visual objects during sustained attention. *PLOS Biology*, *15*(6), e2001903. https://doi.org/10.1371/JOURNAL.PBIO.2001903

Jiang, L., Pei, W., & Wang, Y. (2022). A user-friendly SSVEP-based BCI using imperceptible phase-coded flickers at 60Hz. *China Communications*, *19*(2), 1–14. https://doi.org/10.23919/JCC.2022.02.001

Jiang, Y., Zhou, K., & He, S. (2007). Human visual cortex responds to invisible chromatic flicker. *Nature Neuroscience*, *10*(5), 657–662. https://doi.org/10.1038/nn1879

Kahlbrock, N., Butz, M., May, E. S., Brenner, M., Kircheis, G., Häussinger, D., & Schnitzler, A. (2012). Lowered frequency and impaired modulation of gamma band oscillations in a bimodal attention task are associated with reduced critical flicker frequency. *NeuroImage*, *61*(1), 216–227. https://doi.org/10.1016/j.neuroimage.2012.02.063

Kim, J. W., & Robinson, P. A. (2007). Compact dynamical model of brain activity. *Physical Review E - Statistical, Nonlinear, and Soft Matter Physics*, *75*(3). https://doi.org/10.1103/PhysRevE.75.031907

Kim, Y. J., Grabowecky, M., Paller, K. A., & Suzuki, S. (2011). Differential roles of frequency-following and frequency-doubling visual responses revealed by evoked neural harmonics. *Journal of Cognitive Neuroscience*, *23*(8), 1875–1886. https://doi.org/10.1162/jocn.2010.21536

Kingdom, F. A. A., & Prins, N. (2016). *Psychophysics: a practical introduction* (2nd ed.). Academic Press.

Kircheis, G., Wettstein, M., Timmermann, L., Schnitzler, A., & Häussinger, D. (2002). Critical flicker frequency for quantification of low-grade hepatic encephalopathy. *Hepatology*, *35*(2), 357–366. https://doi.org/10.1053/jhep.2002.30957

Kleiner, M., Brainard, D., & Pelli, D. (2007). What's new in Psychtoolbox-3?

Koch, S. P., Steinbrink, J., Villringer, A., & Obrig, H. (2006). Synchronization between Background Activity and Visually Evoked Potential Is Not Mirrored by Focal Hyperoxygenation: Implications for the Interpretation of Vascular Brain Imag-

ing. *Journal of Neuroscience*, *26*(18), 4940–4948. https://doi.org/10.1523/JNEUROSCI.3989-05.2006

Kogo, N., & Wagemans, J. (2013). The emergent property of border-ownership and the perception of illusory surfaces in a dynamic hierarchical system. *Cognitive Neuroscience*, *4*(1), 54–61. https://doi.org/10.1080/17588928.2012.754750

Kok, P., Bains, L. J., Van Mourik, T., Norris, D. G., & De Lange, F. P. (2016). Selective activation of the deep layers of the human primary visual cortex by top-down feedback. *Current Biology*, *26*(3), 371–376. https://doi.org/10.1016/j.cub.2015.12.038

Kuś, R., Duszyk, A., Milanowski, P., Łabecki, M., Bierzyńska, M., Radzikowska, Z., Michalska, M., Zygierewicz, J., Suffczyński, P., & Durka, P. J. (2013). On the Quantification of SSVEP Frequency Responses in Human EEG in Realistic BCI Conditions (G. R. Barnes, Ed.). *PLoS ONE*, *8*(10), e77536. https://doi.org/10.1371/journal.pone.0077536

Labecki, M., Kus, R., Brzozowska, A., Stacewicz, T., Bhattacharya, B. S., & Suffczynski, P. (2016). Nonlinear Origin of SSVEP Spectra—A Combined Experimental and Modeling Study. *Frontiers in Computational Neuroscience*, *10*, 129. https://doi.org/10.3389/fncom.2016.00129

Lamme, V. A. (2001). Blindsight: The role of feedforward and feedback corticocortical connections. *Acta Psychologica*, *107*(1-3), 209–228. https://doi.org/10.1016/S0001-6918(01)00020-8

Lazarev, V. V., Simpson, D. M., Schubsky, B. M., & DeAzevedo, L. C. (2001). Photic driving in the electro-encephalogram of children and adolescents: Harmonic structure and relation to the resting state. *Brazilian Journal of Medical and Biological Research*, *34*(12), 1573–1584. https://doi.org/10.1590/S0100-879X2001001200010

Lea-Carnall, C. A., Montemurro, M. A., Trujillo-Barreto, N. J., Parkes, L. M., & El-Deredy, W. (2016). Cortical Resonance Frequencies Emerge from Network Size and Connectivity (C. C. Hilgetag, Ed.). *PLOS Computational Biology*, *12*(2), e1004740. https://doi.org/10.1371/journal.pcbi.1004740

Lee, K., Park, Y., Suh, S. W., Kim, S. S., Kim, D. W., Lee, J., Park, J., Yoo, S., & Kim, K. W. (2021). Optimal flickering light stimulation for entraining gamma waves in the human brain. *Scientific Reports*, *11*(1), 1–10. https://doi.org/10.1038/s41598-021-95550-1

Lee, T. S., & Mumford, D. (2003). Hierarchical Bayesian inference in the visual cortex. *Journal of the Optical Society of America A*, *20*(7), 1434. https://doi.org/10.1364/josaa.20.001434

Lewis, C. M., Ni, J., Wunderle, T., Jendritza, P., Lazar, A., Diester, I., & Fries, P. (2021). Cortical gamma-band resonance preferentially transmits coherent input. *Cell Reports*, *35*(5), 109083. https://doi.org/10.1016/J.CELREP.2021.109083

Li, F., Tian, Y., Zhang, Y., Qiu, K., Tian, C., Jing, W., Liu, T., Xia, Y., Guo, D., Yao, D., & Xu, P. (2015). The enhanced information flow from visual cortex to frontal area facilitates SSVEP response: Evidence from model-driven and data-driven causality analysis. *Scientific Reports*, *5*. https://doi.org/10.1038/srep14765

Lin, F. C., Zao, J. K., Tu, K. C., Wang, Y., Huang, Y. P., Chuang, C. W., Kuo, H. Y., Chien, Y. Y., Chou, C. C., & Jung, T. P. (2012). SNR analysis of high-frequency steady-state visual evoked potentials from the foveal and extrafoveal regions of Human Retina. *Proceedings of the Annual International Conference of the IEEE Engineering in Medicine and Biology Society, EMBS*, 1810–1814. https://doi.org/10.1109/EMBC.2012.6346302

Lithari, C., Sánchez-Garciá, C., Ruhnau, P., & Weisz, N. (2016). Large-scale network-level processes during entrainment. *Brain Research*, *1635*, 143–152. https://doi.org/10.1016/j.brainres.2016.01.043

Liu, M. x., Yan, Y., Xue, Q., & Gong, L. (2015). The Research and Analysis of Factors Affecting Critical Flicker Frequency. *Procedia Manufacturing*, *3*, 4279–4286. https://doi.org/10.1016/j.promfg.2015.07.417

Liu-Shuang, J., Norcia, A. M., & Rossion, B. (2014). An objective index of individual face discrimination in the right occipito-temporal cortex by means of fast periodic oddball stimulation. *Neuropsychologia*, *52*(1), 57–72. https://doi.org/10.1016/j.neuropsychologia.2013.10.022

Lupyan, G. (2017). Objective Effects of Knowledge on Visual Perception. *Journal of Experimental Psychology: Human Perception and Performance*, *43*(4), 794–806. https://doi.org/10.1037/xhp0000343.supp

Malpeli, J. G., PETER H. Schiller, & CAROL L. Colby. (1981). Response properties of single cells in monkey striate cortex during reversible inactivation of individual lateral geniculate laminae. *Journal of neurophysiology*, *46*(5), 1102–1119.

Mamassian, P., & Zannoli, M. (2020). Sensory loss due to object formation. *Vision Research*, *174*, 22–40. https://doi.org/10.1016/j.visres.2020.05.005

Mankowska, N. D., Marcinkowska, A. B., Waskow, M., Sharma, R. I., Kot, J., & Winklewski, P. J. (2021). Critical Flicker Fusion Frequency: A Narrative Review. *Medicina 2021, Vol. 57, Page 1096*, *57*(10), 1096. https://doi.org/10.3390/MEDICINA57101096

Manning, C., Jones, P. R., Dekker, T. M., & Pellicano, E. (2018). Psychophysics with children: Investigating the effects of attentional lapses on threshold estimates.

Attention, Perception, and Psychophysics, *80*(5), 1311–1324. https://doi.org/10.3758/s13414-018-1510-2

Manning, J. R., Jacobs, J., Fried, I., & Kahana, M. J. (2009). Broadband shifts in local field potential power spectra are correlated with single-neuron spiking in humans. *Journal of Neuroscience*, *29*(43), 13613–13620. https://doi.org/10.1523/JNEUROSCI.2041-09.2009

Marr, D. (2010). *Vision: A computational investigation into the human representation and processing of visual information*. MIT press.

Martorell, A. J., Paulson, A. L., Suk, H. J., Abdurrob, F., Drummond, G. T., Guan, W., Young, J. Z., Kim, D. N. W., Kritskiy, O., Barker, S. J., Mangena, V., Prince, S. M., Brown, E. N., Chung, K., Boyden, E. S., Singer, A. C., & Tsai, L. H. (2019). Multi-sensory Gamma Stimulation Ameliorates Alzheimer's-Associated Pathology and Improves Cognition. *Cell*, *177*(2), 256–271. https://doi.org/10.1016/j.cell.2019.02.014

Maunsell, J. H., & Treue, S. (2006). Feature-based attention in visual cortex. *Trends in Neurosciences*, *29*(6), 317–322. https://doi.org/10.1016/j.tins.2006.04.001

Mejias, J. F., Murray, J. D., Kennedy, H., & Wang, X.-J. (2016). Feedforward and feedback frequency-dependent interactions in a large-scale laminar network of the primate cortex. *Science Advances*, *2*(11), e1601335. https://doi.org/10.1126/sciadv.1601335

Merkulyeva, N. S. (2022). Conducting Channels in the Visual System. The Third Channel. *Neuroscience and Behavioral Physiology*, *52*(6), 886–898. https://doi.org/10.1007/s11055-022-01313-4

Michalareas, G., Vezoli, J., van Pelt, S., Schoffelen, J. M., Kennedy, H., & Fries, P. (2016). Alpha-Beta and Gamma Rhythms Subserve Feedback and Feedforward Influences among Human Visual Cortical Areas. *Neuron*, *89*(2), 384–397. https://doi.org/10.1016/j.neuron.2015.12.018

Misiak, H. (1951). The decrease of critical flicker frequency with age. *Science*, *113*(2941), 551–552. https://doi.org/10.1126/science.113.2941.551

Moca, V. V., Nikolić, D., Singer, W., & Mureşan, R. C. (2014). Membrane Resonance Enables Stable and Robust Gamma Oscillations. *Cerebral Cortex*, *24*(1), 119–142. https://doi.org/10.1093/CERCOR/BHS293

Moore, C., & Cavanagh, P. (1998). Recovery of 3D volume from 2-tone images of novel objects. *Cognition*, *67*(1-2), 45–71. https://doi.org/10.1016/S0010-0277(98)00014-6

Moran, R. J., Stephan, K. E., Seidenbecher, T., Pape, H. C., Dolan, R. J., & Friston, K. J. (2009). Dynamic causal models of steady-state responses. *NeuroImage*, *44*(3), 796–811. https://doi.org/10.1016/j.neuroimage.2008.09.048

Morrone, M. C., Fiorentini, A., & Burr, D. C. (1996). Development of the Temporal Properties of Visual Evoked Potentials to Luminance and Colour Contrast in Infants. *Vision Research*, *36*(19), 3141–3155. https://doi.org/10.1016/0042-6989(96)00050-8

Murray, M. M., & Herrmann, C. S. (2013). Illusory contours: a window onto the neurophysiology of constructing perception. *Trends in Cognitive Sciences*, *17*(9), 471–481. https://doi.org/10.1016/J.TICS.2013.07.004

Muthukumaraswamy, S. D., & Singh, K. D. (2013). Visual gamma oscillations: The effects of stimulus type, visual field coverage and stimulus motion on MEG and EEG recordings. *NeuroImage*, *69*, 223–230. https://doi.org/10.1016/j.neuroimage.2012.12.038

Muthukumaraswamy, S. D., Singh, K. D., Swettenham, J. B., & Jones, D. K. (2010). Visual gamma oscillations and evoked responses: Variability, repeatability and structural MRI correlates. *NeuroImage*, *49*(4), 3349–3357. https://doi.org/10.1016/j.neuroimage.2009.11.045

Namdar, G., Avidan, G., & Ganel, T. (2015). Effects of configural processing on the perceptual spatial resolution for face features. *Cortex*, *72*, 115–123. https://doi.org/10.1016/j.cortex.2015.04.007

Namerow, N. S. (1971). Temperature Effect on Critical Flicker Fusion in Multiple Sclerosis. *Archives of Neurology*, *25*(3), 269–275.

Neri, P. (2014). Semantic control of feature extraction from natural scenes. *Journal of Neuroscience*, *34*(6), 2374–2388. https://doi.org/10.1523/JNEUROSCI.1755-13.2014

Neri, P., Luu, J. Y., & Levi, D. M. (2006). Meaningful interactions can enhance visual discrimination of human agents. *Nature Neuroscience*, *9*(9), 1186–1192. https://doi.org/10.1038/nn1759

Norcia, A. M., Appelbaum, L. G., Ales, J. M., Cottereau, B. R., & Rossion, B. (2015). The steady-state visual evoked potential in vision research: A review. *Journal of Vision*, *15*(6), 4. https://doi.org/10.1167/15.6.4

O'Donnell, B. F., Vohs, J. L., Krishnan, G. P., Rass, O., Hetrick, W. P., & Morzorati, S. L. (2013a). Application of Brain Oscillations in Neuropsychiatric Diseases. In E. Başar, C. Başar-Eroğlu, A. Özerdem, P. M. Rossini, & G. G. Yener (Eds.), *Application of brain oscillations in neuropsychiatric diseases (supplements to clinical neurophysiology)* (pp. 101–112).

O'Donnell, B. F., Vohs, J. L., Krishnan, G. P., Rass, O., Hetrick, W. P., & Morzorati, S. L. (2013b). The auditory steady-state response (ASSR): a translational biomarker for schizophrenia. *Supplements to Clinical Neurophysiology*, *62*, 101–112. https://doi.org/10.1016/B978-0-7020-5307-8.00006-5

Onitsuka, T., Tsuchimoto, R., Oribe, N., Spencer, K. M., & Hirano, Y. (2022). Neuronal imbalance of excitation and inhibition in schizophrenia: a scoping review of gamma-band ASSR findings. *Psychiatry and Clinical Neurosciences*. https://doi.org/10.1111/PCN.13472

Oostenveld, R., Fries, P., Maris, E., & Schoffelen, J.-M. (2011). FieldTrip: Open Source Software for Advanced Analysis of MEG, EEG, and Invasive Electrophysiological Data. *Computational Intelligence and Neuroscience*, *2011*, 1–9. https://doi.org/10.1155/2011/156869

Park, Y., Lee, K., Park, J., Bae, J. B., Kim, S.-S., Kim, D.-W., Woo, S. J., Yoo, S., & Kim, K. W. (2022). Optimal flickering light stimulation for entraining gamma rhythms in older adults. *Scientific Reports 2022 12:1*, *12*(1), 1–12. https://doi.org/10.1038/s41598-022-19464-2

Parkkonen, L., Andersson, J., Hamalainen, M., & Hari, R. (2008). Early visual brain areas reflect the percept of an ambiguous scene. *Proceedings of the National Academy of Sciences*, *105*(51), 20500–20504. https://doi.org/10.1073/pnas.0810966105

Parrott, A. C. (1982). Critical Flicker Fusion Thresholds and Their Relationship to Other Measures of Alertness. *Pharmacopsychiatry*, *15*(S 1), 39–43. https://doi.org/10.1055/S-2007-1019548

Pastor, M. A., Valencia, M., Artieda, J., Alegre, M., & Masdeu, J. C. (2007). Topography of Cortical Activation Differs for Fundamental and Harmonic Frequencies of the Steady-State Visual-Evoked Responses . An EEG and PET H 15 2 O Study. *Cerebral Cortex*, *17*(August), 1899–1905. https://doi.org/10.1093/cercor/bhl098

Pastor, M. A., Artieda, J., Arbizu, J., Valencia, M., & Masdeu, J. C. (2003). Human Cerebral Activation during Steady-State Visual-Evoked Responses. *The Journal of Neuroscience*, *23*(37), 11621–11627. https://doi.org/10.1523/JNEUROSCI.23-37-11621.2003

Pedziwiatr, M. A., Von Dem Hagen, E., & Teufel, C. (2021). Knowledge-driven perceptual organization reshapes information sampling via eye movements. *bioRxiv*. https://doi.org/10.1101/2021.09.24.461220

Pelli, D. G. (1997). The VideoToolbox software for visual psychophysics: Transforming numbers into movies. *Spatial Vision*, *10*(4), 437–442.

Perenboom, M. J., van de Ruit, M., Zielman, R., van den Maagdenberg, A. M., Ferrari, M. D., Carpay, J. A., & Tolner, E. A. (2020). Enhanced pre-ictal cortical responsivity in migraine patients assessed by visual chirp stimulation. *Cephalalgia*, *40*(9), 913–923. https://doi.org/10.1177/0333102420912725

Peters, J. L., Bavin, E. L., Brown, A., Crewther, D. P., & Crewther, S. G. (2020). Flicker fusion thresholds as a clinical identifier of a magnocellular-deficit dyslexic

subgroup. *Scientific Reports*, *10*(1), 1–10. https://doi.org/10.1038/s41598-020-78552-3

Pfurtscheller, G., Neuper, C., & Mohl, W. (1994). Event-related desynchronization (ERD) during visual processing. *International journal of psychophysiology*, *16*, 147–153.

Picton, T. W., John, M. S., Dimitrijevic, A., & Purcell, D. (2003). Human auditory steady-state responses: Respuestas auditivas de estado estable en humanos. *http://dx.doi.org/10.3109/14992020309101316*, *42*(4), 177–219. https://doi.org/10.3109/14992020309101316

Poljac, E., De-Wit, L., & Wagemans, J. (2012). Perceptual wholes can reduce the conscious accessibility of their parts. *Cognition*, *123*(2), 308–312. https://doi.org/10.1016/j.cognition.2012.01.001

Poljac, E., Verfaillie, K., & Wagemans, J. (2011). Integrating biological motion: The role of grouping in the perception of Point-Light actions (S. He, Ed.). *PLoS ONE*, *6*(10), e25867. https://doi.org/10.1371/journal.pone.0025867

Pomerantz, J. R., & Portillo, M. C. (2011). Grouping and Emergent Features in Vision: Toward a Theory of Basic Gestalts. *Journal of Experimental Psychology: Human Perception and Performance*, *37*(5), 1331–1349. https://doi.org/10.1037/a0024330

Prins, N., & Kingdom, F. A. (2018). Applying the model-comparison approach to test specific research hypotheses in psychophysical research using the Palamedes toolbox. *Frontiers in Psychology*, *9*(JUL), 1250. https://doi.org/10.3389/fpsyg.2018.01250

Ramos-Junior, S. G., Celino, D. R., Rodor, F. F., Ribeiro, M. R., Müller, S. M., Filho, T. F. B., & Filho, M. S. (2011). Experimental evidences for visual evoked potentials with stimuli beyond the conscious perception threshold. *2011 ISSNIP Biosignals and Biorobotics Conference: Biosignals and Robotics for Better and Safer Living, BRC 2011*, 86–90. https://doi.org/10.1109/BRC.2011.5740685

Rao, R. P. N., & Ballard, D. H. (1999). Predictive coding in the visual cortex: a functional interpretation of some extra-classical receptive-field effects. *Nature Neuroscience*, *2*(1), 79–87. https://doi.org/10.1038/4580

Read, J. C. (2015). The place of human psychophysics in modern neuroscience. *Neuroscience*, *296*, 116–129. https://doi.org/10.1016/J.NEUROSCIENCE.2014.05.036

Regan, M. P., & Regan, D. (1989). Objective Investigation of Visual Function Using a Nondestructive Zoom-FFT Technique for Evoked Potential Analysis. *Canadian Journal of Neurological Sciences / Journal Canadien des Sciences Neurologiques*, *16*(2), 168–179. https://doi.org/10.1017/S0317167100028845

Roberts, J. A., & Robinson, P. A. (2012). Quantitative theory of driven nonlinear brain dynamics. *NeuroImage*, *62*(3), 1947–1955. https://doi.org/10.1016/j.neuroimage.2012.05.054

Rojas, D. C., & Wilson, L. B. (2014). γ-band abnormalities as markers of autism spectrum disorders. *Biomarkers in Medicine*, *8*(3), 353–368. https://doi.org/10.2217/BMM.14.15

Rubin, M. (2021). When to adjust alpha during multiple testing: a consideration of disjunction, conjunction, and individual testing. *Synthese*, *199*(3-4), 10969–11000. https://doi.org/10.1007/S11229-021-03276-4/TABLES/1

Salchow, C., Strohmeier, D., Klee, S., Jannek, D., Schiecke, K., Witte, H., Nehorai, A., & Haueisen, J. (2016). Rod driven frequency entrainment and resonance phenomena. *Frontiers in Human Neuroscience*, *10*, 12. https://doi.org/10.3389/FNHUM.2016.00413/BIBTEX

Samaha, J., Boutonnet, B., Postle, B. R., & Lupyan, G. (2018). Effects of meaningfulness on perception: Alpha-band oscillations carry perceptual expectations and influence early visual responses. *Scientific Reports*, *8*(1), 6606. https://doi.org/10.1038/s41598-018-25093-5

Schiller, P. H. (2010). Parallel information processing channels created in the retina. *Proceedings of the National Academy of Sciences of the United States of America*, *107*(40), 17087–17094. https://doi.org/10.1073/pnas.1011782107

Schiller, P. H., & Tehovnik, E. J. (2015a). The Midget and Parasol Systems. *Vision and the visual system* (pp. 135–158). Oxford University Press. https://doi.org/10.1093/ACPROF:OSO/9780199936533.003.0008

Schiller, P. H., & Tehovnik, E. J. (2015b). The Retina. *Vision and the visual system* (pp. 35–58). Oxford University Press. https://doi.org/10.1093/ACPROF:OSO/9780199936533.003.0003

Schwarzkopf, D. S., De Haas, B., & Rees, G. (2012). Better Ways to Improve Standards in Brain-Behavior Correlation Analysis. *Frontiers in Human Neuroscience*, *6*(JUNE 2012), 200. https://doi.org/10.3389/fnhum.2012.00200

Seymour, R. A., Rippon, G., Gooding-Williams, G., Sowman, P. F., & Kessler, K. (2020). Reduced auditory steady state responses in autism spectrum disorder. *Molecular Autism*, *11*(1), 1–13. https://doi.org/10.1186/S13229-020-00357-Y/FIGURES/7

Sharma, P., Sharma, B. C., Puri, V., & Sarin, S. K. (2007). Critical flicker frequency: Diagnostic tool for minimal hepatic encephalopathy¿. *Journal of Hepatology*, *47*(1), 67–73. https://doi.org/10.1016/j.jhep.2007.02.022

Shaw, A. D., Moran, R. J., Muthukumaraswamy, S. D., Brealy, J., Linden, D. E., Friston, K. J., & Singh, K. D. (2017). Neurophysiologically-informed markers

of individual variability and pharmacological manipulation of human cortical gamma. *NeuroImage*, *161*, 19–31. https://doi.org/10.1016/j.neuroimage.2017.08.034

Shaw, A. D., Muthukumaraswamy, S. D., Saxena, N., Sumner, R. L., Adams, N. E., Moran, R. J., & Singh, K. D. (2020). Generative modelling of the thalamo-cortical circuit mechanisms underlying the neurophysiological effects of ketamine. *NeuroImage*, *221*, 117189. https://doi.org/10.1016/j.neuroimage.2020.117189

Solf, B., Schramm, S., Blum, M. C., & Klee, S. (2020). The Influence of the Stimulus Design on the Harmonic Components of the Steady-State Visual Evoked Potential. *Frontiers in Human Neuroscience*, *14*(September), 1–11. https://doi.org/10.3389/fnhum.2020.00343

Spaak, E., Bonnefond, M., Maier, A., Leopold, D. A., & Jensen, O. (2012). Layer-specific entrainment of gamma-band neural activity by the alpha rhythm in monkey visual cortex. *Current Biology*, *22*(24), 2313–2318. https://doi.org/10.1016/j.cub.2012.10.020

Spratling, M. W. (2016). A neural implementation of Bayesian inference based on predictive coding. *Connection Science*, *28*(4), 346–383. https://doi.org/10.1080/09540091.2016.1243655

Srinivasan, R., Bibi, F. A., & Nunez, P. L. (2006). Steady-state visual evoked potentials: Distributed local sources and wave-like dynamics are sensitive to flicker frequency. *Brain Topography*, *18*(3), 167–187. https://doi.org/10.1007/s10548-006-0267-4

Summerfield, C., & Egner, T. (2009). Expectation (and attention) in visual cognition. *Trends in Cognitive Sciences*, *13*(9), 403–409. https://doi.org/10.1016/j.tics.2009.06.003

Swettenham, J. B., Muthukumaraswamy, S. D., & Singh, K. D. (2009). Spectral properties of induced and evoked gamma oscillations in human early visual cortex to moving and stationary stimuli. *Journal of Neurophysiology*, *102*(2), 1241–1253. https://doi.org/10.1152/JN.91044.2008/ASSET/IMAGES/LARGE/Z9K0080996200006.JPEG

Tada, M., Kirihara, K., Koshiyama, D., Fujioka, M., Usui, K., Uka, T., Komatsu, M., Kunii, N., Araki, T., & Kasai, K. (2020). Gamma-Band Auditory Steady-State Response as a Neurophysiological Marker for Excitation and Inhibition Balance: A Review for Understanding Schizophrenia and Other Neuropsychiatric Disorders. *Clinical EEG and Neuroscience*, *51*(4), 234–243. https://doi.org/10.1177/1550059419868872/ASSET/IMAGES/LARGE/10.1177{_}1550059419868872-FIG2.JPEG

Tadin, D., Lappin, J. S., Blake, R., & Grossman, E. D. (2002). What constitutes an efficient reference frame for vision? *Nature Neuroscience*, *5*(10), 1010–1015. https://doi.org/10.1038/nn914

Tallon-Baudry, C., & Bertrand, O. (1999). Oscillatory gamma activity in humans and its role in object representation. *Trends in cognitive sciences*, *3*(4), 151–162.

Taylor, G., Hipp, D., Moser, A., Dickerson, K., & Gerhardstein, P. (2014). The development of contour processing: Evidence from physiology and psychophysics. https://doi.org/10.3389/fpsyg.2014.00719

Teufel, C., Dakin, S. C., & Fletcher, P. C. (2018). Prior object-knowledge sharpens properties of early visual feature-detectors. *Scientific Reports*, *8*(1), 10853. https://doi.org/10.1038/s41598-018-28845-5

Teufel, C., & Fletcher, P. C. (2020). Forms of prediction in the nervous system. *Nature Reviews Neuroscience*, *21*(4), 231–242. https://doi.org/10.1038/s41583-020-0275-5

Teufel, C., & Nanay, B. (2017). How to (and how not to) think about top-down influences on visual perception. *Consciousness and Cognition*, *47*, 17–25. https://doi.org/10.1016/j.concog.2016.05.008

Thut, G., Schyns, P. G., & Gross, J. (2011). Entrainment of perceptually relevant brain oscillations by non-invasive rhythmic stimulation of the human brain. *Frontiers in Psychology*, *2*(JUL), 170. https://doi.org/10.3389/fpsyg.2011.00170

Tononi, G., Srinivasan, R., Russell, D. P., & Edelman, G. M. (1998). Investigating neural correlates of conscious perception by frequency-tagged neuromagnetic responses. *Proceedings of the National Academy of Sciences*, *95*(6), 3198–3203. https://doi.org/10.1073/pnas.95.6.3198

Tu, T., Xin, Y., Gao, X., & Gao, S. (2012). Chirp-modulated visual evoked potential as a generalization of steady state visual evoked potential. *Journal of Neural Engineering*, *9*(1), 016008. https://doi.org/10.1088/1741-2560/9/1/016008

Uhlhaas, P. J., Roux, F., Rodriguez, E., Rotarska-Jagiela, A., & Singer, W. (2010). Neural synchrony and the development of cortical networks. *Trends in Cognitive Sciences*, *14*(2), 72–80. https://doi.org/10.1016/J.TICS.2009.12.002

van Kerkoerle, T., Self, M. W., Dagnino, B., Gariel-Mathis, M.-A., Poort, J., van der Togt, C., & Roelfsema, P. R. (2014). Alpha and gamma oscillations characterize feedback and feedforward processing in monkey visual cortex. *Proceedings of the National Academy of Sciences of the United States of America*, *111*(40), 14332–41. https://doi.org/10.1073/pnas.1402773111

van Pelt, S., Boomsma, D. I., & Fries, P. (2012). Magnetoencephalography in twins reveals a strong genetic determination of the peak frequency of visually in-

duced gamma-band synchronization. *Journal of Neuroscience*, *32*(10), 3388–3392. https://doi.org/10.1523/JNEUROSCI.5592-11.2012

Vanrie, J., & Verfaillie, K. (2004). Perception of biological motion: A stimulus set of human point-light actions. *Behavior Research Methods, Instruments, and Computers*, *36*(4), 625–629. https://doi.org/10.3758/BF03206542

VanRullen, R. (2016). Perceptual Cycles. *Trends in Cognitive Sciences*, *20*(10), 723–735. https://doi.org/10.1016/j.tics.2016.07.006

VanRullen, R., & Macdonald, J. S. (2012). Perceptual echoes at 10 Hz in the human brain. *Current Biology*, *22*(11), 995–999. https://doi.org/10.1016/j.cub.2012.03.050

Vergeer, M., Kogo, N., Nikolaev, A. R., Alp, N., Loozen, V., Schraepen, B., & Wagemans, J. (2018). EEG frequency tagging reveals higher order intermodulation components as neural markers of learned holistic shape representations. *Vision Research*, *152*, 91–100. https://doi.org/10.1016/j.visres.2018.01.007

Vialatte, F. B., Maurice, M., Dauwels, J., & Cichocki, A. (2010). Steady-state visually evoked potentials: Focus on essential paradigms and future perspectives. https://doi.org/10.1016/j.pneurobio.2009.11.005

Victor, J. D., & Conte, M. M. (2000). Two-frequency analysis of interactions elicited by Vernier stimuli. *Visual Neuroscience*, *17*(6), 959–973. https://doi.org/10.1017/S0952523800176151

Vidal, J. R., Chaumon, M., Kevin O'regan, J., & Tallon-Baudry, C. (2006). Visual grouping and the focusing of attention induce gamma-band oscillations at different frequencies in human magnetoencephalogram signals. *Journal of cognitive neuroscience*, *18*(11), 1850–1862. http://direct.mit.edu/jocn/article-pdf/18/11/1850/1935685/jocn.2006.18.11.1850.pdf?casa_token=n_8GczCiqR8AAAAA:FlVPsmziXBcwxbtTmHRwqeGGKvIQFTcznNJpxFMVpBiIL9j0usfTLjfQBx-pkPV7WrIq

Wagemans, J. (2018). Perceptual Organization. In J. T. Wixted & J. Serences (Eds.), *The stevens' handbook of experimental psychology and cognitive neuroscience: Vol. 2. sensation, perception & attention* (pp. 803–872). John Wiley & Sons, Inc. http://www.gestaltrevision.be/pdfs/bookchapters/Perceptual_Organization.pdf

Wagemans, J., Elder, J. H., Kubovy, M., Palmer, S. E., Peterson, M. a., Singh, M., & von der Heydt, R. (2012). A century of Gestalt psychology in visual perception: I. Perceptual grouping and figure–ground organization. *Psychological Bulletin*, *138*(6), 1172–1217. https://doi.org/10.1037/a0029333

Wandell, B. A. (1995). *Foundations of vision*. Sinauer Associates. https://psycnet.apa.org/record/1995-98050-000

Waytowich, N. R., & Krusienski, D. J. (2016). Multiclass Steady-State Visual Evoked Potential Frequency Evaluation Using Chirp-Modulated Stimuli. *IEEE Transactions on Human-Machine Systems*, *46*(4), 593–600. https://doi.org/10.1109/THMS.2015.2513014

Wei, X. X., & Stocker, A. A. (2015). A Bayesian observer model constrained by efficient coding can explain 'anti-Bayesian' percepts. *Nature Neuroscience*, *18*(10), 1509–1517. https://doi.org/10.1038/nn.4105

Wieser, M. J., Miskovic, V., & Keil, A. (2016). Steady-state visual evoked potentials as a research tool in social affective neuroscience. *Psychophysiology*, *53*(12), 1763–1775. https://doi.org/10.1111/PSYP.12768

Wilford, M. M., & Wells, G. L. (2010). Does facial processing prioritize change detection? Change blindness illustrates costs and benefits of holistic processing. *Psychological Science*, *21*(11), 1611–1615. https://doi.org/10.1177/0956797610385952/ASSET/IMAGES/LARGE/10.1177{_}0956797610385952-FIG2.JPEG

Wyart, V., & Tallon-Baudry, C. (2008). Neural dissociation between visual awareness and spatial attention. *Journal of Neuroscience*, *28*(10), 2667–2679. https://doi.org/10.1523/JNEUROSCI.4748-07.2008

Xing, D., Yeh, C. I., Burns, S., & Shapley, R. M. (2012). Laminar analysis of visually evoked activity in the primary visual cortex. *Proceedings of the National Academy of Sciences of the United States of America*, *109*(34), 13871–13876. https://doi.org/10.1073/pnas.1201478109

Zhang, G., Cui, Y., Zhang, Y., Cao, H., Zhou, G., Shu, H., Yao, D., Xia, Y., Chen, K., & Guo, D. (2021). Computational exploration of dynamic mechanisms of steady state visual evoked potentials at the whole brain level. *NeuroImage*, *237*, 118166. https://doi.org/10.1016/J.NEUROIMAGE.2021.118166

Zhigalov, A., Herring, J. D., Herpers, J., Bergmann, T. O., & Jensen, O. (2019). Probing cortical excitability using rapid frequency tagging. *NeuroImage*, *195*, 59–66. https://doi.org/10.1016/j.neuroimage.2019.03.056

Zhigalov, A., Duecker, K., & Jensen, O. (2021). The visual cortex produces gamma band echo in response to broadband visual flicker. *PLoS Computational Biology*, *17*(6). https://doi.org/10.1371/journal.pcbi.1009046

Zhu, D., Bieger, J., Garcia Molina, G., & Aarts, R. M. (2010). A Survey of Stimulation Methods Used in SSVEP-Based BCIs. *Computational Intelligence and Neuroscience*, *2010*, 1–12. https://doi.org/10.1155/2010/702357